

I. REPORT DOCUMENTATION PAGE

Form Approved
OMB No. 0704-0788

Public reporting burden for the collection of information is estimated to average 1 hour per response, including the time for reviewing instructions, searching existing data sources, gathering and maintaining the data needed, and completing and reviewing the collection of information. Send comments regarding the burden estimate or any other aspect of the collection of information, including suggestions for reducing the burden, to Washington Headquarters Services, Directorate for Information Operations and Analysis, 1215 Jefferson Davis Highway, Suite 1204, Arlington, VA 22202-4162, and to the Office of Management and Budget, Paperwork Reduction Project (0704-0188), Washington, DC 20585.

1. AGENCY USE ONLY (Leave blank)	2. REPORT DATE	3. REPORT TYPE AND DATES COVERED
	Jan. 13, 1997	FINAL REPORT
4. TITLE AND SUBTITLE Development of a Technique to Determine (U) the Morphology and Dynamics of Agglomerates in Chemically Reacting Flows		5. FUNDING NUMBERS
		PE - 6110ZF PR - 2308 SA - BS G - F49620-92-J-0447
6. AUTHOR(S) Tryfon Charalampopoulos		
7. PERFORMING ORGANIZATION NAME(S) AND ADDRESS(ES) Louisiana State University Mechanical Engineering Department Baton Rouge, LA 70803		AFOSR-TR- 90 97 0144
8. SPONSORING/MONITORING AGENCY NAME(S) AND ADDRESS(ES) AFOSR/NA 110 Duncan Avenue, Suite B115 Bolling AFB DC 20332-0001		9. SPONSORING/MONITORING AGENCY REPORT NUMBER NA 92-J-0447
10. DISTRIBUTION/AVAILABILITY STATEMENT Approved for public release; distribution is unlimited		
11. DISTRIBUTION CODE		
12. ABSTRACT (Maximum 200 words) An exact formulation was developed for the prediction of the internal electric field of an assembly of Rayleigh particles exposed to an incident radiation field which: (i) satisfies the energy conservation (ii) accounts for self contribution and multiple scattering effects (iii) is invariant to coordinate transformation and (iv) is particularly useful for soot diagnostics. Based on this formulation a computer code (AGGL) was written for the computation of extinction, total scattering efficiency factors, and differential scattering intensities for agglomerates. The computations were free of error and resulted in tenfold reduction in computational time. Agglomerates with straight chain configuration were generated in a diffusion carbon/monoxide/air flame seeded with iron pentacarbonyl vapor. Both the primary particle size and the aspect ratio were found to be strong functions of the vapor concentration and aggregate residence time. X-ray diffraction measurements revealed that the particles consisted predominantly of iron oxide(Fe2O3). In-situ measurements of the particle dynamics using polarized and depolarized light scattering showed that the signal to noise ratio was significantly improved when measurements were carried out in the cross correlation mode. It was also found that monitoring of the particle dynamics was possible with sampling times as low as 25 nanoseconds.		
14. SUBJECT TERMS Soot, Agglomerates, Optical diagnostics, Depolarized and Polarized Dynamic Light Scattering, Light Scattering Theory for Agglomerates, Chain-like Iron Oxide Aggregates		15. NUMBER OF PAGES 139
16. PRICE CODE		
17. SECURITY CLASSIFICATION OF REPORT Unclassified	18. SECURITY CLASSIFICATION OF THIS PAGE Unclassified	19. SECURITY CLASSIFICATION OF ABSTRACT Unclassified
		20. LIMITATION OF ABSTRACT UL

TABLE OF CONTENTS

	Page
I. Summary of Work Carried out During the Grant Period.....	1
II. Publications Related to Contract/Grant.....	4
III. Personnel Involved in the Research Program.....	5
IV. Development of a System for Controlled Combustion Synthesis of Chain - like Aggregates.....	6
1. Introduction	6
2. Development of the System.....	8
3. Tests and Results.....	12
4. Summary.....	14
5. References.....	15
V. Use of Polarized and Depolarized Dynamic Light Scattering to Determine the Morphology and Dynamics of Flame Borne Particulates.....	29
1. Introduction.....	29
2. Apparatus.....	31
3. System Tests and Results.....	33
4. Summary and Conclusions.....	36
5. References.....	37
VI. Sensitivity Considerations for Use of Dynamic Light Scattering to Infer Velocities and Brownian Diffusion Coefficients of Agglomerates in High Temperature Enviroment.....	47
1. Introduction and Motivation.....	47
2. Experimental Considerations.....	48
3. Conditions for Particle Velocity and Size Inference from from the Heterodyne Correlation Function.....	51
4. Applications to Non- Spherical Particles.....	59
5. Discussion.....	64
6. Summary of Results.....	66
7. References.....	67
VII. Computer Code (AGGL) for the Prediction of Light Scattering Properties of Agglomerated Particulates Composed of Rayleigh Sized Primary Particles.....	77
VIII. User's Guide for AGGL with Source Code.....	128
1. User Interface: AGGL _ Shell.....	128
2. Output List.....	129
3. Sample Master Program and Results.....	130

19970314 077

I. Summary of the Work Carried out During the Grant Period

The work carried out during the grant period may be summarized as follows:

a) An exact formulation has been developed for the prediction of the internal electric field of an assembly of particles exposed to an incident radiation field which: (i) satisfies the energy conservation requirement (ii) accounts for self contribution and multiple scattering field effects (iii) is invariant to coordinate transformation and (iv) is particularly useful for soot and other particulate diagnostics at the ultraviolet (UV) part of the spectrum. This part of the work has been published in the Journal of Physics D: Applied Physics, Vol. 27, 2258-2270 (1994) under the title "On the electromagnetic scattering and absorption of agglomerated small spherical particles".

b) Based on the developed exact formulation of light scattering by agglomerated small particles, partial derivatives of scattering quantities were derived with respect to refractive index and size parameter. Computations of the derivatives could be conveniently incorporated into scattering computer code. This provided for an efficient computation of the various derivatives needed for data inversion purposes as opposed to the usual finite difference approximation which requires judicious choice of step sizes and additional computational time and, as a result, is subject to inaccuracy as well as inefficiency.

Specific considerations regarding data inversion were provided. Because experimental errors are inevitable, it is suggested that an error response or inversion uncertainty analysis could be included as an inherent part of the data inversion task. A complete data inversion procedure should consist of an evaluation of derivatives, inversion of measured data and estimation of uncertainty resulting from measurement of errors.

The pairing problem in the sense of deciding which quantities to measure in order to obtain the most accurate and reliable results was also posed and was found to be a critical and important step.

With respect to the inversion scheme, it was found that the same conclusions/restrictions apply to agglomerate geometries other than the straight chain one, such as clusters(closely packed structure) and randomly branched chain.

A simple inversion algorithm for the complex refractive index was developed which exhibits excellent numerical behavior and provides a prototype for developing more sophisticated inversion algorithms. Because all further data inversion of light scattering data inevitably involves inversion for the complex refractive index, the approach developed during the course of this study constitutes the building blocks for future studies aiming at complete characterization of agglomerated particle systems. The results of this part of the work have been published in the Journal of Physics D: Applied Physics Vol. 28 , pp 2585- 2594(1995) under the title “On the inverse acattering problem for characterization of agglomerated particulates” partial derivative formulation”.

c) Based on the the exact light scattering formulation developed and summarized under (a) above as new computer code under the acronym (AGGL) was written for the computations of extinction, absorption, total scattering efficiency factors, and differential scattering intensities for agglomerates of arbitrary configurations. Derivatives with respect to the refractive index and size parameter were also internally generated. The computations showed that the code was free of error and resulted in tenfold reduction in computational time. Details about the developed code and a listing of the code itself is presented in Section VII of this Report.

d) Since one of the objectives of the study was to develop a technique for the determination of the dynamics of particulates in reacting flows a system was developed by which agglomerated particulates of specific configurations, namely chain like aggregates could be produced. The system can accommodate both mechanical and thermophoretic particle sampling and optical measurements to be performed as functions of axial and radial position within a diffusion flame system. The reactor consists of a diffusion type burner constructed of stainless steel. The fuel used was carbon monoxide seeded with iron pentacarbonyl vapor (Fe(CO)₅) and the oxidizer was ambient air. The details of the experimental system are discussed in the Section IV of this Report.

e) Using the experimental system developed (see (d) above) nanosized chain-like aggregates were synthesized in an iron pentacarbonyl—carbon monoxide—air diffusion flame system. The size and shape of the chainlike aggregates and primary particles were characterized in terms of measurable morphological parameters such as diameter of primary particles and aspect ratio. The influence of operating conditions on the parameters have been investigated systematically by employing thermophoretic and transmission electromicroscopy (TEM). The morphological parameters were found to be strong functions of operating conditions, residence time, and locations within the flame and could be controlled by adjusting the concentrations of Fe(CO)₅ seeded in the flame through the variation of the carrier gas flowrate and temperature of metal additive.

X-ray diffraction measurements coupled with thermodynamic equilibrium composition predictions were used to identify the chemical state of the particulate components. The results indicated that the aggregates formed in this flame consisted predominantly of primary particles of Fe₂O₃. In addition the physical and chemical mechanisms of formation of chain-like aggregates

were reviewed. Our observations pointed to the possibility that while magnetic forces are necessary for providing a self - alignment mechanism, the flame temperature may also be critical for the formation of chain like aggregates. The results of this part of the work were presented in Twenty Sixth Symposium (International) on Combustion and Published in the Proceedings of the Combustion Institute under the title "Controlled Combustion Synthesis of Nanosized Iron Oxide Aggregates " and co-authored by Z. Zhang and T.T. Charalampopoulos.

f) As planned in the original proposal an optical system had to be developed that would allow monitoring of the depolarized correlation function corresponding to the chain-like aggregates formed under flame conditions. The optical system was also to provide for monitoring of the polarized correlation function from the same set of aggregates. This particular system has been developed and has been tested. The results obtained so far have shown that data can be collected at sampling rates as low as 25 nanoseconds. Furthermore it has been shown that significant reduction in noise levels can be accomplished when the measurements are carried out in the cross correlation mode. This is because noisy effects such as those resulting from afterpulsing of the photomultiplier tubes become virtually uncorrelated under cross correlation conditions. The results of this part of the work are presented in Section V of this Report.

g) In the course of the development of the method for obtaining the dynamics/morphology of the aggregates using depolarized light scattering the use of heterodyne dynamic light scattering to infer velocities and Brownian diffusion coefficients of agglomerates in reacting flows was assessed analytically. The analysis related the variance of the inferred velocity and diffusion parameters to the variance of the normalized correlation function of three detected light's intensity (or photon count) fluctuations. An experimental criterion was established for insuring the accuracy of the inferred results. This criterion defined the range of angles for which the statistical uncertainties of the inferred results, when normalized with respect to the inferred parameters, magnitudes are less than or equal to the statistical uncertainty of the experimentally determined correlation function. Under suitable assumptions, this analysis is extended to non-spherical, cylindrically-symmetric particles (or agglomerates)

II. Publications Related to the Aforementioned Contract/Grant

1. T. T. Charalampopoulos and P. K. Panigrahi , "Depolarization Characteristics of Agglomerated Particulates - Reciprocity Relations" *J. Physics D: Applied Physics*. Vol. 26 pp 2075-2081(1993).
2. B. J. Stagg and T. T. Charalampopoulos, "Refractive Indices of Pyrolytic Graphite, Amorphous Carbon and Flame Soot in the Temperature Range 25 to 600 degrees Celsius" *Combustion and Flame* , Vol. 94 pp 381-396 (1993) .
3. D. W. Hahn and T. T. Charalampopoulos "The role of Iron Additives in Sooting Premixed Flames" *Twenty- Fourth Symposium (International) on Combustion/ The Combustion Institute*, pp 1007-1014(1992) .
4. D. W. Hahn and T. T. Charalampopoulos, "On the Optical Properties of Submicrometer Inhomogeneous Flame Particulates " *J. Physics D: Applied Physics*, Vol. 26, pp 1851-1858 (1993).
5. W. Lou and T. T. Charalampopoulos, " On the Electromagnetic Scattering and Absorption of Agglomerated Small Particles", *J. Physics D: Applied Physics*, Vol. 27, pp 2258-2270 (1994)..
6. W. Lou and T. T. Charalampopoulos, " On the Inverse Scattering Problem for Characterization of Agglomerated Particulates: Partial Derivative Formulation", *J. Physics D; Applied Physics*, Vol. 28, pp 2585- 2594 (1995).
7. Z. Zhang and T. T. Charalampopoulos, "Controlled Combustion Synthesis of Iron Oxide Aggregates" *Twrnty-Sixth Symposium (International) on Combustion /The Combustion Institute* Papaer No 842 (1996).
8. D. Venizelos, W. Lou and T. T. Charalampopoulos, "Development of an Algorithm for the Calculation of the Scattering Properties of Agglomerates" *Applied Optics* , Paper No 10190.

III. Personnel involved in the reserach program.

1. T. T. Chalamopoulos, Principal Investigator
2. Dr. D. W. Hahn, as part time Resaerch Associate
3. Dr. D. Venizelos, as graduate student and as part time Research Associate
4. Z. Zhang, as MS student
5. Anna Olmetchenko, as PhD student
6. Glenn Waguespack , as PhD student
7. W. Lou , as MS student
8. Ruben Munoz, MS student
9. Angel Borrel, as student assistant
10. Marry Tilley, as student assistant

IV. Development of a system for controlled combustion synthesis of chain-like aggregates

1. Introduction

. Knowledge of the shape and size of particles and their aggregates formed in the combustion system is significant in many areas of research and practical applications. Information about the size

and shape of anisotropic particulates is important for (i) predicting growth and oxidation of particulates in combustion systems, (ii) studying the agglomeration mechanism of particulates, (iii) the efficient control of fibrous aerosols in the industrial hygiene, (iv) the study of real time quality control of materials synthesized in flame reactors, and (v) air pollution control studies[1]

The techniques used for determining the size and shape of particulates in flame system can be divided into two categories: ex-situ and in-situ. Both techniques possess advantages and disadvantages and are complementary. The present study constitutes the first step towards the development of an in-situ optical method by which the optical and morphological properties of agglomerated structures, as well as their dynamics in reacting systems, may be determined. The potential of such an approach and its implications has been recently discussed in Charalampopoulos [1]. Thus the objectives of this part of the study were to develop a suitable experimental system for the synthesis of anisotropic aggregates and to determine the most appropriate type of extractive sampling technique without compromising the integrity of the samples. Since straight chains constitute the simplest structure and most well defined form of aggregates, they have been chosen for the purpose of this study.

Numerous experimental studies have been performed to synthesize submicron size particulates and to determine the shape and/or the morphological features of aggregates formed in combustion processes [2-9], employing both ex-situ and in-situ methods. The studies show that the structure of aggregates in flame strongly depends on the technology of synthesis, the type of combustion system, fuel, fuel equivalence ratio, and operating conditions. Some of the studies specifically investigated the synthesis of chain-like aggregates. Two techniques were used in the synthesis of the chain-like aggregates. With the exploding wire method [2,3] predominantly chains were produced, consisting up to thousands of primary particles, while the disadvantages of the method are that the process is not continuous and is difficult to control in order to produce uniformly dispersed chains. The combustion synthesis via the gaseous phase was used for the production of chain-like aggregates as well. The metal additives, such iron pentacarbonyl, are introduced into flames where decomposition and chemical reaction take place to form metal oxide vapors. Because of the nature of the chemical structures, the molecules of some metal oxides, such as Fe_2O_3 [5], tend to form chain structures.

Then the coagulation of primary particles from subsequent nucleation and condensation leads to chain-like aggregates.

A number of experiments [5,7] have been conducted to synthesize the chain-like aggregates based on the above combustion technology. The chain -like aggregates of iron oxide particulates were generated by seeding a CO/O₂/N₂ flame with iron pentacarbonyl (Fe(CO)₅) vapor. The Fe(CO)₅ vapor decomposed at above 300 C to form iron oxide in the presence of oxygen. Under appropriate flame conditions, the iron oxide particles formed chain-like aggregates. The investigators also characterized the morphology of chain-like aggregates employing ex-situ technique. The characteristics of the chain aggregates were determined for the samples taken in the post flame region for different concentrations of the seeding vapor and varying O₂:CO mixing ratio. The studies found that both diameter of primary particles and length of chain-like aggregates were controllable and dependent of additive concentration [6,7].

2. Development of the system

In order to fulfill the objectives of the study, the experimental system should exhibit the following properties: control, reproducibility, and stability. In accordance with these design criteria, the experimental system, developed for the controlled combustion synthesis of chain-like aggregates and for the performance of the ex-situ characterization, consists of a supply and feeding system, which supplies the combustion gases and seeding vapor to the burner and regulates the flowrates of all gases in the combustion process; a burner, which produces the flame; sampling system, which extracts the particulates from the flame to facilitate the TEM analysis; and driving mechanism systems, which controls the location of the burner with respect to the sampling probe and optical apparatus. A schematic of the experimental set-up is shown in Figure 1.

A supply-feeding system, as shown in Figure 2, was designed to deliver, control and monitor the gases to the burner. The amount of each component fed into the burner was accurately controlled and monitored by this system. The capabilities of the system include the ability to provide independent variations of the feeding flow-rate of gases through a network of compressed gas cylinders, flowmeters, valves and tubing. The flowrates of critical reactants, CO and O₂ were monitored by means of the thermal-type digital mass flow-meters [Hastings, Model HFM 200] with fluctuation less than 1 percent of the full scale flow rate of 5 l/min. Because of the high corrosion effect of iron pentacarbonyl vapor, a purging system is incorporated with the gas supply system that the whole gas supply system, including the burner and digital flow meters, is purged with nitrogen after every run of the flame. The purging nitrogen acts to remove some of the deposits within the reactant supply line and burner, which maintains the cleanliness of the supply and feeding system for continuous accuracy and provides the necessary condition of reproducibility and control of the flame experiments.

Figure 3 illustrates the additive feeding system. The iron pentacarbonyl vapor is introduced into the CO-air flame by diverting a small fraction of bulk fuel flow through a column of liquid Fe(CO)₅ stored in a heated metallic stainless steel cylinder. By monitoring the temperature of the cylinder and carrier gas flowrate, partially saturated Fe(CO)₅ vapor is transported by the carrier gas and injected into the flame through the inner tube. A thermal-type digital mass flow-meter [Hastings, Model HFM 200L] is used to monitor the flow rate of carriage gas with fluctuation within 1 percent of the full scale flow rate of 300 cc/min. The concentration of iron pentacarbonyl vapor introduced into the flame was regulated by controlling the temperature of the heated evaporate cylinder and the carrier gas flowrate. The actual mass flowrate of iron pentacarbonyl supplied for a given carrier flowrate and cylinder temperature is calibrated by measuring the condensed mass of iron pentacarbonyl vapor during a measured time interval into a condensation coil maintained at -15 C as the evaporator outlet gas passes through the coil. Thus the concentration of iron pentacarbonyl

vapor delivered to the bulk fuel flow for varying carrier flow rate at a given cylinder temperature is known prior to entering into the flame. The calibrated mass flowrate curve along with calculated saturation mass flowrate is presented in Figure 4.

In order to minimize the condensation and deposition of the iron pentacarbonyl vapor on the wall along the inlet line during the flame operation, the fuel line from outlet of the evaporate cylinder to the inlet of the burner is heated to an average temperature 92 C and thermally insulated from the surroundings. Four thermal couples were mounted to monitor the wall temperature at various locations along the line fuel supply line.

The burner (Figure 5) used in this study is a concentric stainless steel (316) tube burner with a diameter of the inner tube 1/4 inch and the annular interval between the tubes 1/16 inch. The fuel, directed to the surface of the burner through the central tube, mixes with through diffusion with oxidized, which is either obtained from ambient room air or directed through an annular region surrounding the fuel tube to produce a nearly conical diffusion flame. A ceramic honeycomb with fixed height above the burner surface was utilized to straighten the gas flow streamline and to stabilize the flame.

Two different sampling systems for the collection of particles were tested in the course of this study. One is a mechanical suction type sampling system, the other one is a thermophoretic sampling system. The mechanical extractive type sampling system is depicted in Figure 6.

Prior to burner ignition and during the period required for the achievement of thermal equilibrium between the burner system and its surroundings, a small amount of nitrogen is allowed to go through the probe through the 'purging' line, which enables the sampling system to be kept clean and prevents the inlet of the probe from being clogged by solid particulates. The particle sampling is accomplished by establishing a vacuum downstream of the probe and consequently drawing the flame gases with particles into the probe. The by-pass line is designed for the selection of sampling rate such that the minimum disturbance of the flame near the probe inlet is observed, which ensures the establishment of the isokinetic sampling condition [8]. When the desired sampling condition is attained, sampling can be initiated by switching the two three-way valves to the 'sampling' mode. Upon leaving the probe, samples pass into the sampling line and deposit on the carbon-coated copper grid seated on a Swagelok in-line filter element.

The mechanical suction probes designed in the test are: a water-cooled probe, and a uncooled probe (as shown in Figure 7). The original overall considerations of the design for the water cooled sampling probe were to quench further agglomeration and chemical reactions within the probe [9]. It consists of three concentric stainless steel tubes (I.D. of 0.125 inch, O.D. of 0.25 inch, interval between the tubes of 0.125 inch). Cooling water runs between the two annular regions. Samples are withdrawn through the center tube. A thinner probe (I.D. of 0.0785 inch, O.D. of 0.125 inch)

without cooling water was designed to minimize disturbance to the flame while chemical reactions within the probe were of less concern.

Since continuous agglomeration within the probe was of concern in this study, a thermophoretic sampling system was also designed and constructed. It is believed [10] that the thermophoretic sampling technique is well suited for the collection of particles for the morphology studies. The principle is that the probe provides an instant cold surface in the hot flame to establish a temperature gradient which drives the flame-born particles toward the cold surface to deposit on it. The cold surface also quenches the chemical reaction and coagulations of particles that are already captured. Therefore, the thermophoretic sampling technique eliminates the potential agglomeration of particles[10,11]. The conventional carbon coated copper grid [Electron Microscopy Science, Model CF200-Cu, 200mesh] is used as a cold surface to catch the particulates. The carbon coating film not only is stable under the electron beam, comparing with other coatings, also be able to withstand relatively high temperature as well. It is very easily oxidized in the flame environment, however, it can be exposed in the flame for very short time intervals. A slotted plate is placed between the probe and flame to deflect the air current induced by the motion of the probe and to block the heat transfer from the flame to the probe[8].

The thermophoretic sampling system consists of a double-acting pneumatic cylinder [BIMBA, Model MRS-04-DXP] of 3/4 inch diameter and 3 inch stroke that is driven by high air pressure 40 psi, a solenoid controlled directional 4-way valve, and a computer controlled variable time-delay relay circuit which accurately controls the position and motion of the thermophoretic probe assembly. The thermophoretic probe is mounted to the piston shaft. A nitrid-based permanent magnet is mounted on the piston to operate a hall effect switch (BIMBA HSCX-04) as shown in Figure 8. The BHE switch is connected in series with a D.C power supply (9v) and a oscilloscope. During the operation, a constant current is passed through the hall sensor. When the magnet is not directly below the sensor, the current distribution will be uniform and no potential difference exists across the output. When the magnet is directly below the sensor, it disturbs the current distribution, producing a potential difference across the output. The circuitry amplifies this voltage to signal the oscilloscope. By recording the time variations of the oscilloscope signal and the position of the piston, the position and movement of the probe can be precisely determined. A piston speed of 0.86 m/s, and a transition time 4+1ms for the entry of the probe from the edge to the center of the flame are achieved with the present system. The computer controlled variable time-delay relay circuit also controls the sampling time which varies from 75 to 200 ms, depending on the additive concentration and the sampling position.

The precise positioning of the probe with respect to the burner surface is very critical in order to obtain the reproducible measurements of size distribution varying with the height above the burner surface. The mechanical components of the thermophoretic probe control system and mechanical suction probe system are mounted on a rigid rotational optical table. To provide good spatial

resolution within the flame, the vertical position of the probe is fixed, whereas the burner moves up and down through a burner translation mechanism. A pulse generator attached to the gear of the burner translation mechanism monitors the displacement of the burner such that the height of the probe with respect to the burner surface can be accurately controlled. The calibration of the translation mechanism determined that the precision for measuring the actuate burner height is within 1/10 of a millimeter. The burner translation mechanism, as shown in Figure 1, is similar to the one used by Charalampopoulos [12]. The precise positioning of the thermophotetic probe within the flame is achieved by the alignment of optical arm with respect to the laser beam. The optical arm, on which the probe is mounted, is fixed at 90 $^{\circ}$ with respect to the incident laser beam so that the probe is perpendicular to the laser beam which is directed and focussed at the central axis of the burner. The carbon grid is attached on the tip of the probe and its position is zeroed with reference to the laser beam. The precision of the horizontal positioning of the probe/grid assembly is within 0.2 mm.

3. Test and results

The diffusion type carbon monoxide-air flame supported on the system was tested. The tests showed that the stable seeded CO-air diffusion flame was obtainable for CO flowrate ranging from 200 to 450 cc/min. Flow rates lower than 200 cc/min can not sustain a flame and flow rates higher than 450 cc/min induce flickering in the flame. At a total fuel flowrate of 450 cc/min the flame seeded with iron pentacarbonyl presented a most stable and suitable sampling condition for the investigation of variations of the particulate morphology with the operating conditions, with the ceramic honeycomb fixed at 40 mm height above the burner surface. The picture of this flame under unseeded and seeded conditions is shown in Figure 9. The flame was characterized with temperature measurement. A platinum vs. platinum-10% rhodium thermocouple with a bead diameter of 0.3 mm was used in the temperature measurements. The position and alignment of the thermocouple is the same as that of the thermophoretic probe. Figure 10 shows the radiation corrected radial temperature profiles for unseeded CO/air diffusion flame at various heights above the burner surface. The maximum fluctuation for the temperature measurements occurred at 35 mm height and was found to be 2.7% different about the mean temperature value of three measurements.

Experiments for synthesis of chain-like aggregates and sampling particles were performed. Chain-like aggregates were produced in the CO-air diffusion flame seeded with $\text{Fe}(\text{CO})_5$ vapor. A typical TEM micrograph is shown in the Figure 11 for samples taken by mechanical suction probes and thermophoretic probe. The image of the iron oxide particles appears to be hexagonal or polyhedral whereas the image of the aggregates resembles straight chain-like structure. as may be seen from the figure, the difference of the results was significant in comparing the samples collected by both mechanical probes with thermophoretic probe. It appeared that there was no significant difference in the primary particle diameter, whereas the aggregate morphologies determined by these two ex-situ techniques were highly different. The size and shape were identical for the samples collected from the water cooled and the non-cooled probes. Majority of the aggregates are branched chains and consisted of hundred of primary particles per aggregate, yet the size of the aggregates could not be reduced by decreasing the concentration of $\text{Fe}(\text{CO})_5$ vapor and did not vary significantly with location. It was suspected that since the sizes of both probes are comparable with that of the flame, the flame might have been severely distorted by the probe. In addition, no mechanism exists to prevent additional agglomeration, the further agglomeration might have occurred within the probe. The samples collected by these two probes probably do not accurately represent the true morphology of the particulates as they occur within the flame. However, the thermophoretic sampling technique, in which the particulates deposit on a cold surface which then quenches further agglomeration, should be better able to preserve the morphology of the particulates as they occur within the flame. For this reason, the thermophoretic sampling system was utilized for the determination of size and

morphology of the particles and their aggregates produced in the experiments. The size and shape of the chain-like aggregates and the primary particles were characterized in terms of diameter of primary particles, number of the primary particles per aggregate, and aspect ratio of aggregates of chain-like aggregates based on the TEM micrographs. A quantitative data on the primary particle size distribution and aggregate size distribution as a function of location in the flame were obtained. The variations of the morphological parameters with location was assessed by collecting samples within the flame along the centerline at the heights of 4, 15, 25, 35 mm above the burner surface. Figures 12 to 14 represent the frequency distributions of the diameters of primary particles, the number of primary particles per aggregate, and the aspect ratio of the straight chains as determined by sampling and TEM photographs at the operating condition of total fuel flowrate 450 cc/min and carrier flowrate 20 cc/min. At short residence times (4mm above the burner surface) the straight chains were observed with ill defined shapes that quantitative analysis was not able to provided. As the height increased, the particles grow and the time available for aggregation was increased, resulting in longer and more well defined chain-like aggregates.

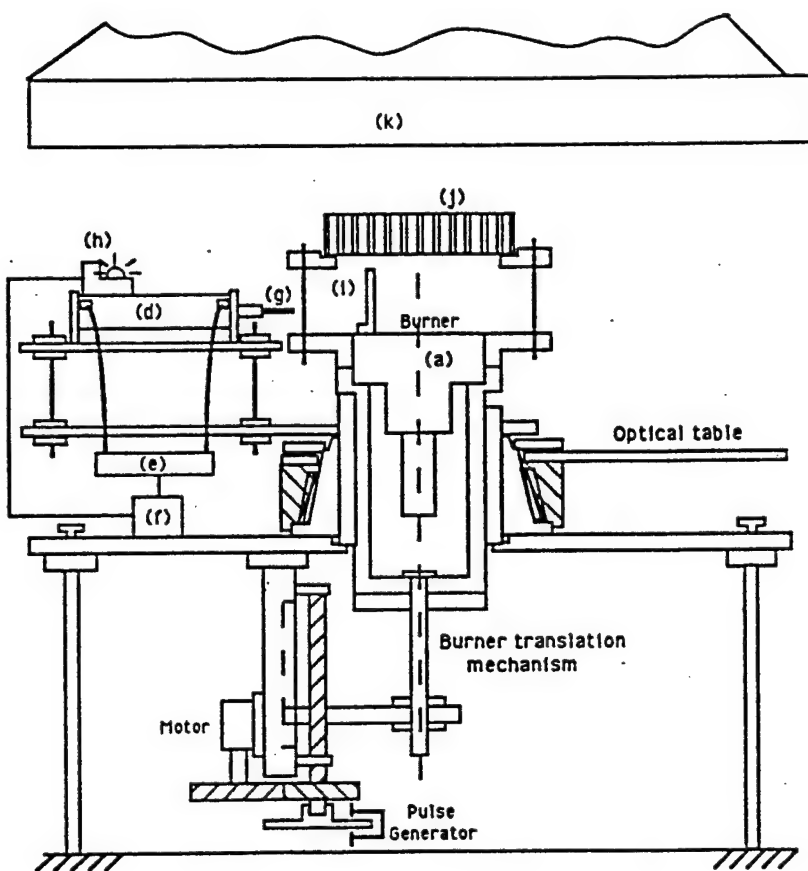
4. Summary

The accomplishment of this part of the study is summarized as follows:

1. An experimental system for controlled combustion synthesis of particulates has been developed and tested that the system can be used for the performance of both the ex-situ morphology measurements and the in-situ optical measurements of the determination of the morphology of the anisotropic particulates.
2. Predominantly chain-like aggregates were synthesized in an iron pentacarbonyl vapor seeded CO/air diffusion flame supported on a concentric stainless steel tube burner.
3. The tests showed that for particle morphology studies, thermophoretic probe system may be suitable for the sampling without compromising the integrity of the samples.
4. The analysis of TEM photographs of the samples collected by thermophoretic sampling technique provided a qualitative description of the morphology of the particulates formed in the flame. The average diameter of the primary particles and the aspect ratio of chain-like aggregates increased with increase of the residence time.

5. References

- [1]. T. T. Charalampopoulos, Prog. Energy Combust. Science, 18:13-45, 1992.
- [2]. E. G. Chase and H. R. Moore, Exploding Wires, 4:1958-1968, 1971.
- [3]. R. A. Vomela and K. T. Whitby, J. Colloidal Interface Sci., 25:568, 1967.
- [4]. H. L. Green and W. R. Lane, Particulate Clouds: Dusts, Smokes and Mists, page 33, 1964.
- [5]. Kasper, S-N Shon, and D. T. Shaw, Journal of Am. Ind. Hyg. Assoc., 41:288-296, 1980.
- [6]. M.T. Cheng, G. W. Xie, and D. T. Shaw, Aerosol Science and Technology, 14:74-81, 1991.
- [7]. R. E. Weiss, V. N. Kaputsin and P.V. Hobbs, J. Geophysical Research, 97:14527-14531, 1992.
- [8]. W. J. Dodds, M.B. Dolket, and A. M. Mellow, Technical Report, Part I, MAST—RGR:1-78, 1976.
- [9]. D. W. Hahn, PhD Dissertation, Louisiana State University , B.R. La , 1992.
- [10]. R. A. Dobbins and C. M. Megaridis, Langmuir, 3:254--266,1987.
- [11]. D. E. Rosner and D. W. Mackowski, Combustion Science and Technology, 80:87-101.1991.
- [12]. T. T. Charalampopoulos, Review of Scientific Instruments, 58: 1638-1646, 1987.



- (a): Concentric tube diffusion burner
- (b): Additive-seeding system
- (c): Evaporate cylinder
- (d): Double-acting pneumatic cylinder
- (e): 4-way solenoid valve
- (f): Controllable time-delay relay circuit
- (g): Thermophoretic probe
- (h): Hall effect switch
- (i): Slotted plate (deflector)
- (j): Ceramic honeycomb
- (k): Exhaust fume hood

Figure 1: Experimental setup

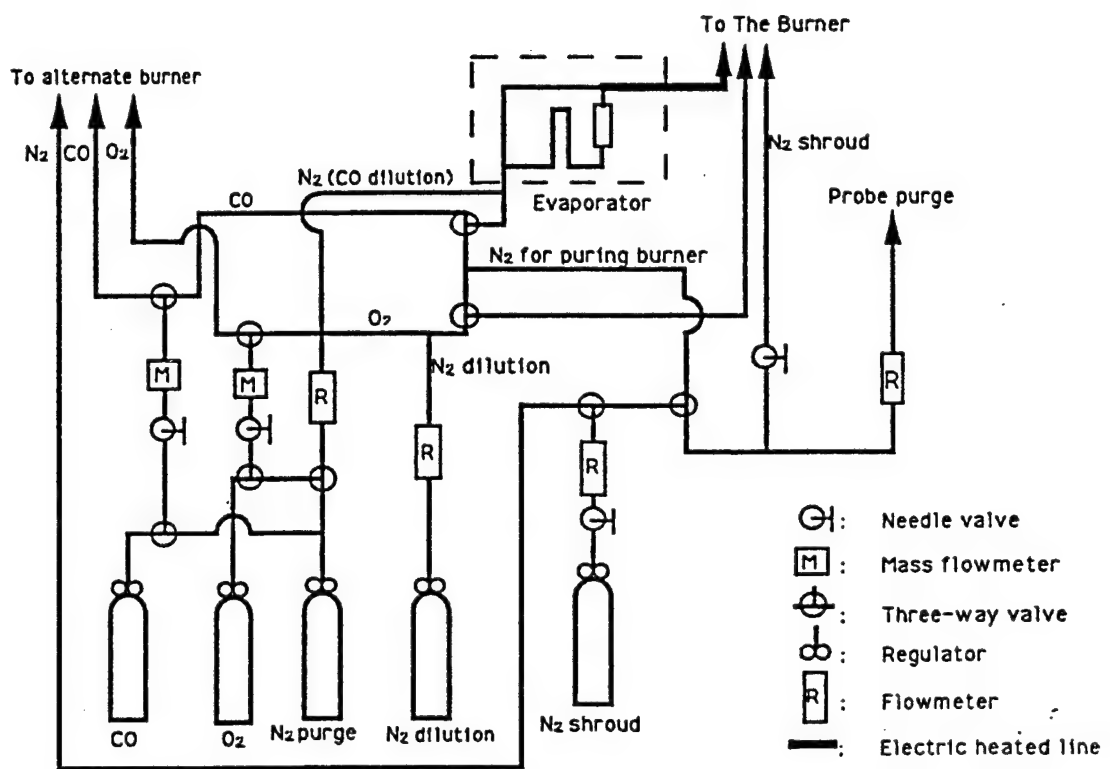


Figure 2: Gas supply system

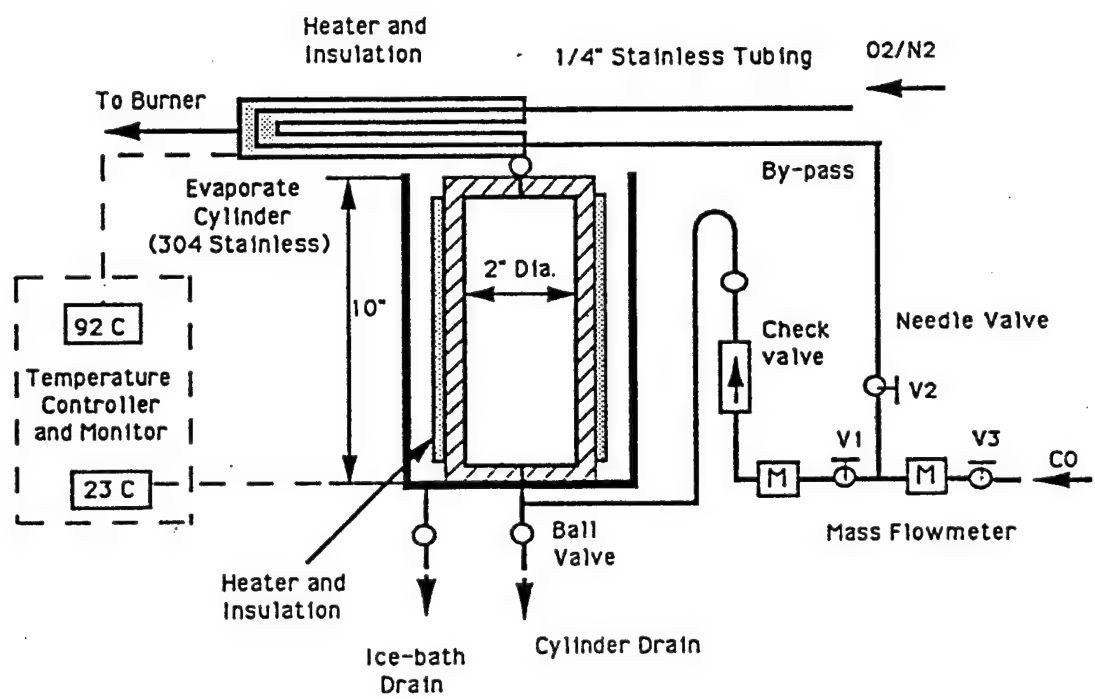


Figure 3: Additive-feeding system

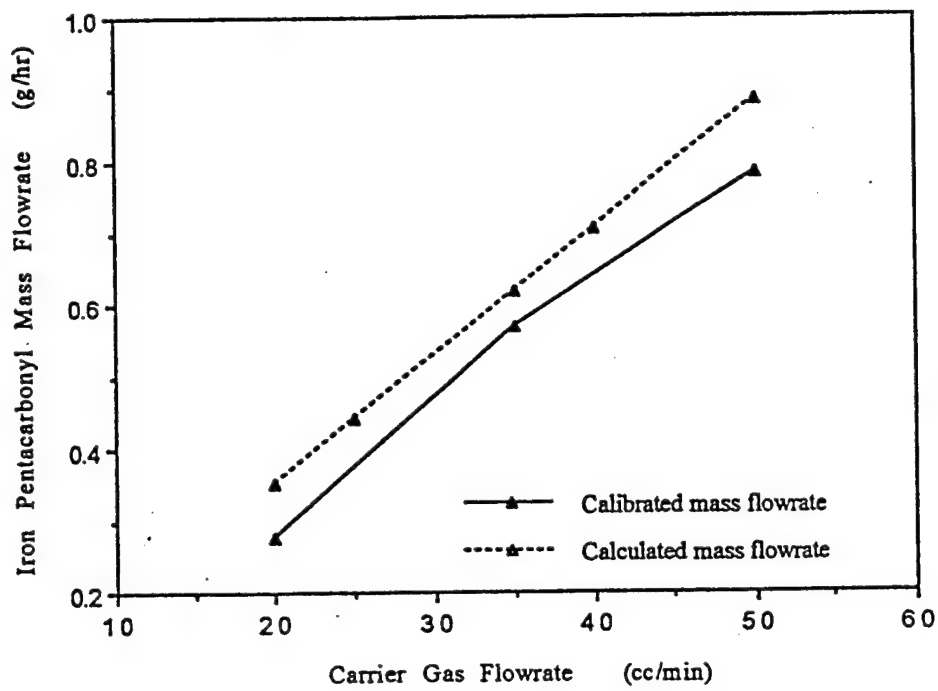


Figure 4: The calibrated and calculated mass flowrate of iron pentacarbonyl with varying carrier flowrate at heated cylinder temperature 23°C

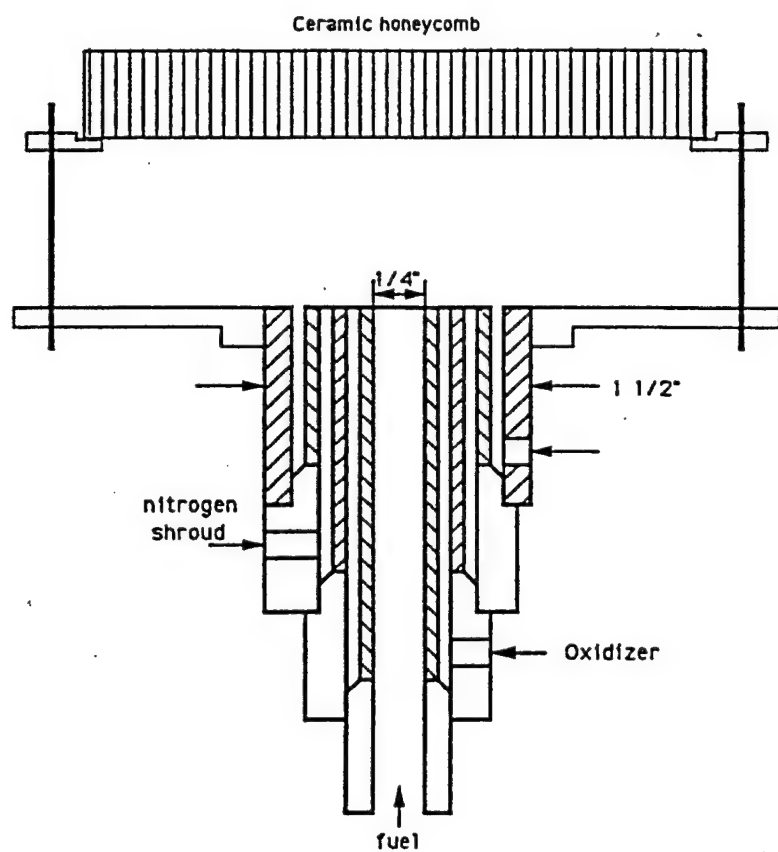


Figure 5: Concentric tube diffusion burner

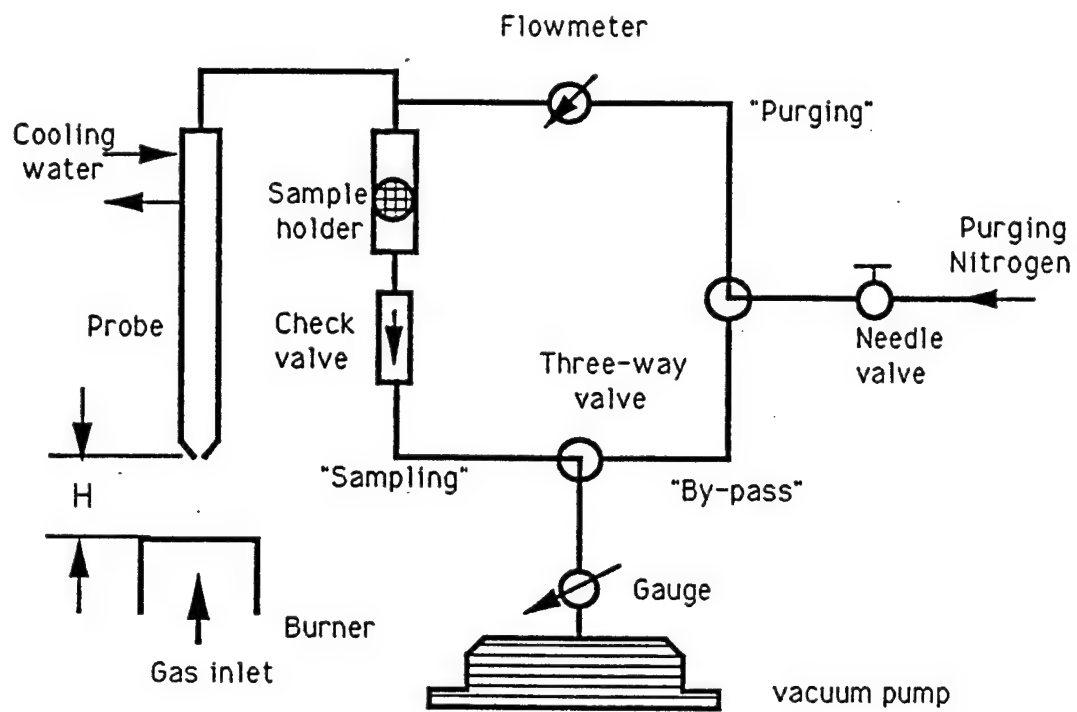


Figure 6: Mechanical suction sampling system

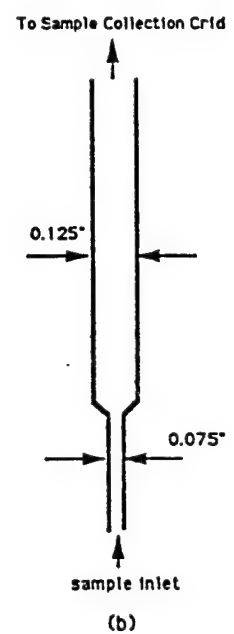
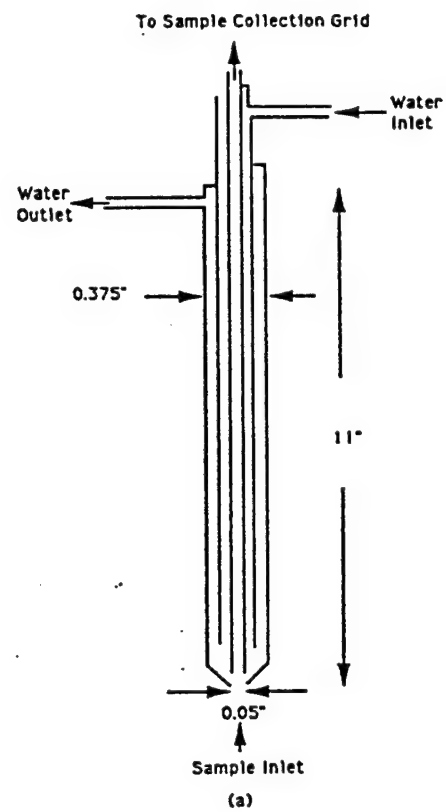


Figure 7: Probes: (a) water-cooled probe (b) uncooled probe

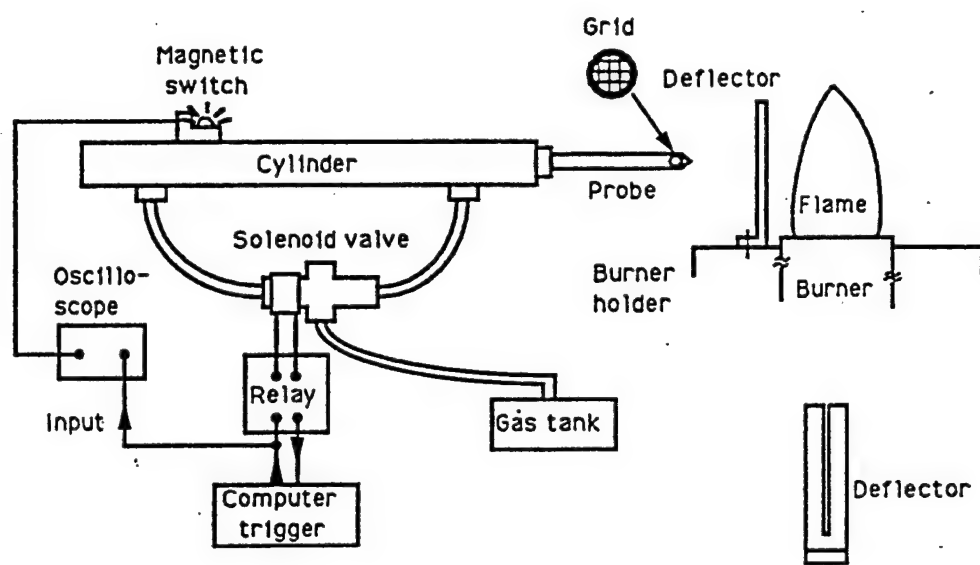
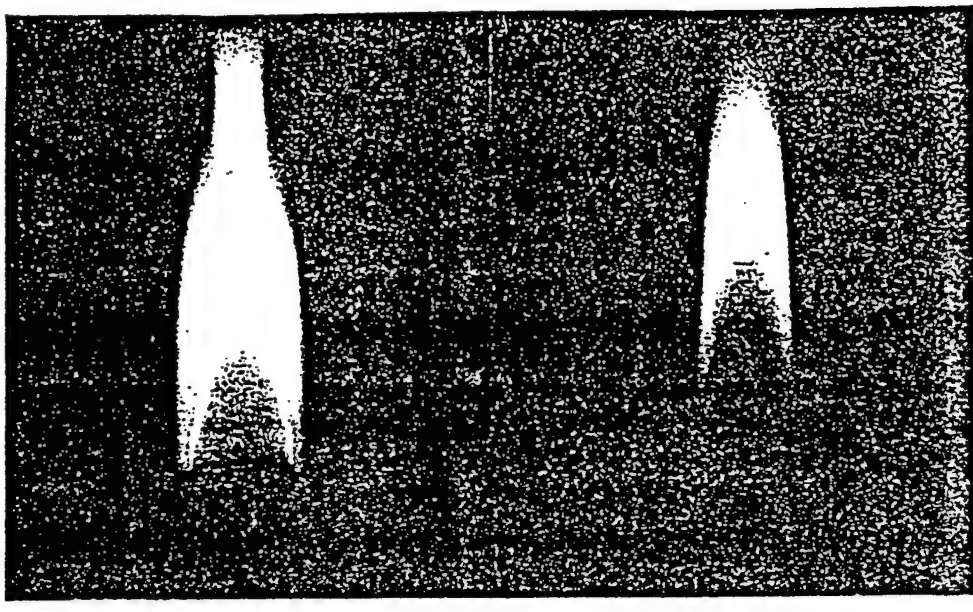


Figure 8: Pneumatic actuator and thermophoretic sampling system



(a)

(b)

Figure 9: CO-air diffusion flame (a)unseeded flame (b)seeded with $Fe(CO)_5$ vapor

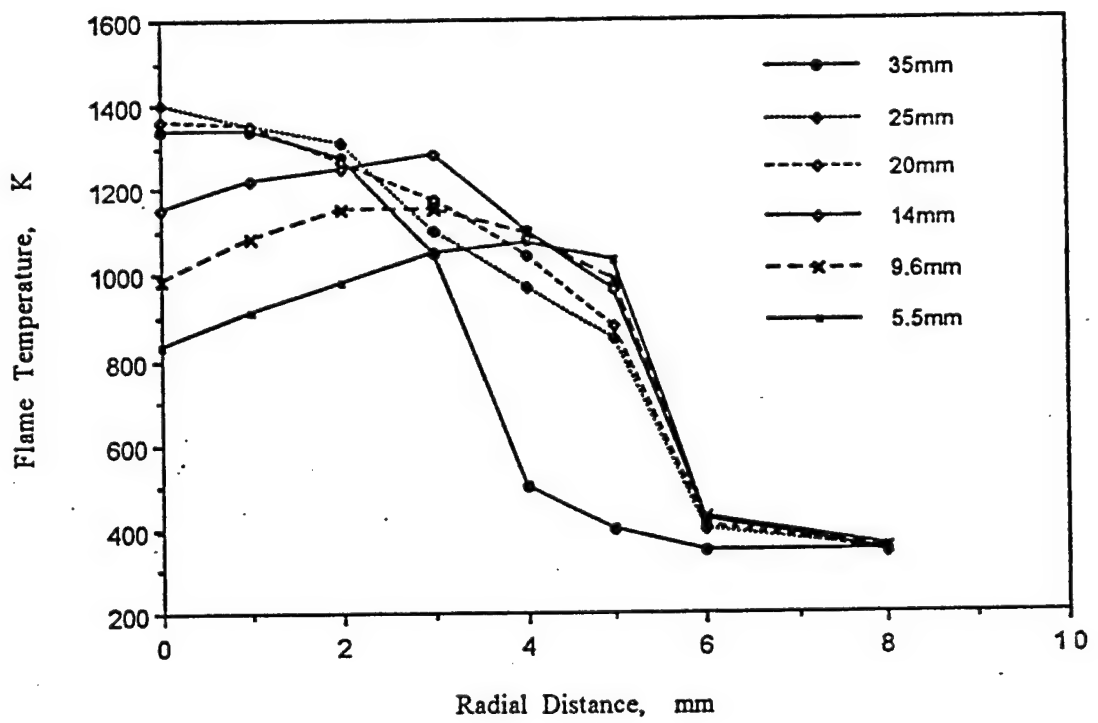


Figure 10: Radiation corrected radial temperatures for CO/air diffusion flame with varying height above the burner surface

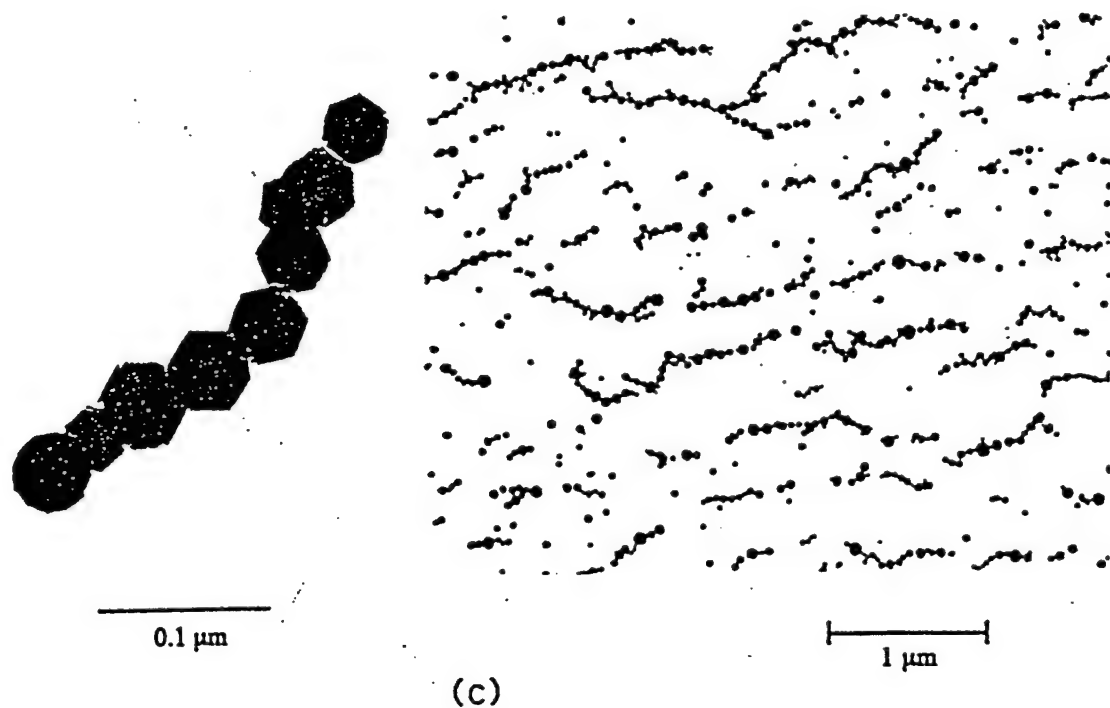
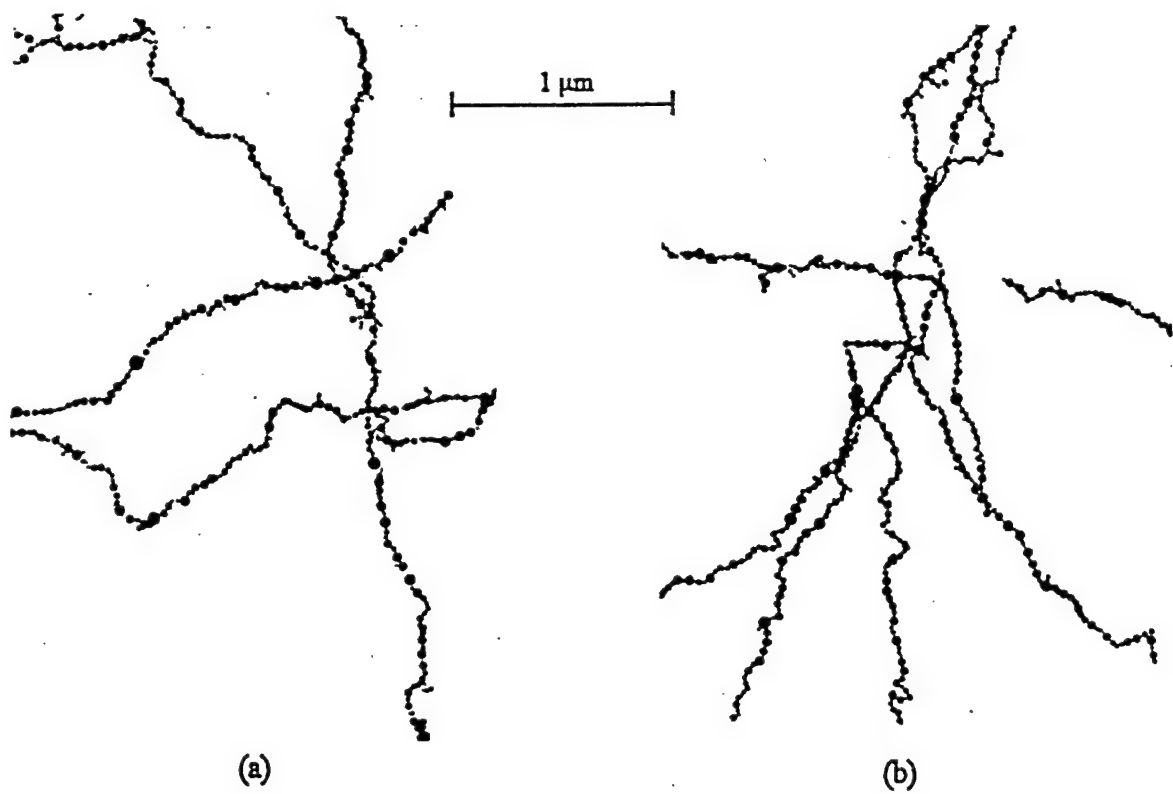


Figure 11: The TEM micrographs: (a) sample taken by water-cooled probe (b) sample taken by uncooled probe (c) sample taken by thermophoretic probe

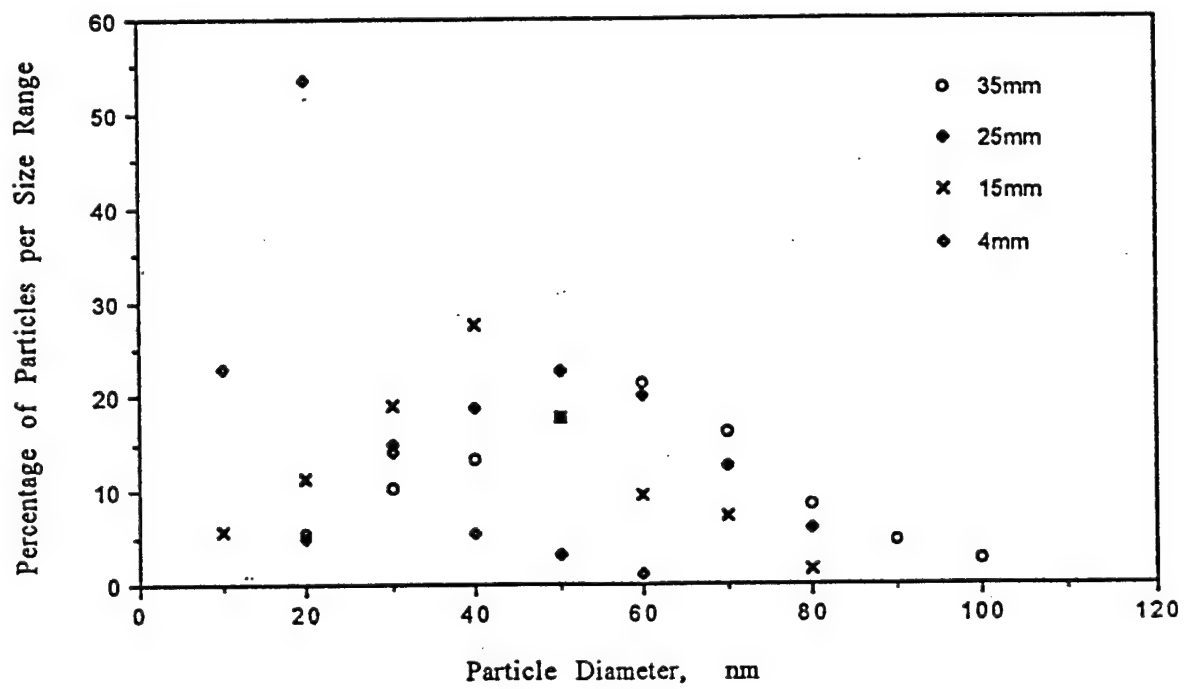


Figure 12: The distributions of diameter of primary particles of chain-like aggregates with varying height above the burner surface

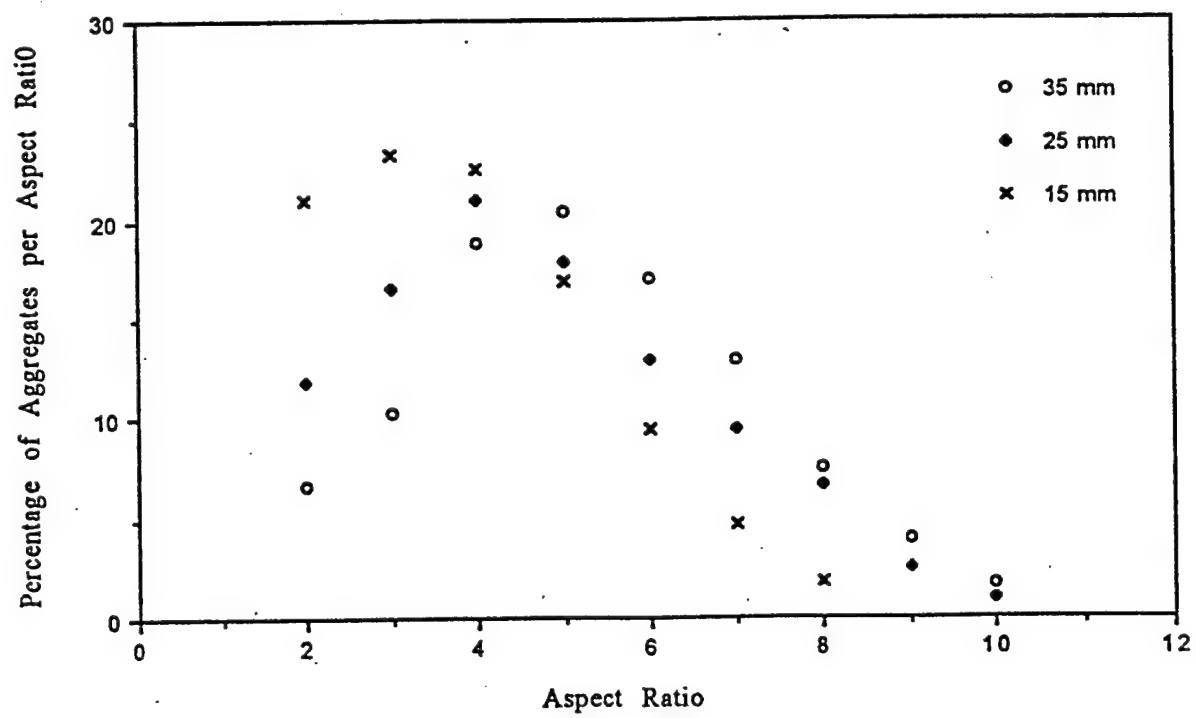


Figure 13: The distribution of aspect ratio of chain-like aggregates with varying height above the burner surface

V. Use of Polarized and Depolarized Dynamic Light Scattering to Determine the Morphology and Dynamics of Flame-Borne Agglomerates

1. Introduction

The objective of the current study is to adapt and utilize light scattering techniques to measure both the morphological (primary particle diameter, aspect ratio, etc.) and dynamic (Brownian translational and rotational diffusion coefficients) properties of agglomerated structures occurring within flames. Such information is useful for process monitoring of materials synthesis using flame technology, pollution control studies, flame emission calculations, and soot formation studies. The predominant advantage of *in situ* measurements, such as light scattering, over the alternative *ex situ* measurements, such as the extraction of particulate samples from the flame for subsequent examination using electron microscopy, is that the *in situ* measurements are less likely to disturb the specimens being studied. Additionally, *in situ* measurement techniques are generally more easily automated.

The current study involves performing low scattering angle ($\theta < 7^\circ$) polarized (VV) and depolarized (VH) dynamic light scattering (DLS) measurements and classical depolarization ratio measurements of the straight chain agglomerates of iron oxide particles occurring along the central axis of a conical iron-pentacarbonyl-seeded CO-O₂ diffusion flame. These optical measurements are supplemented by flame temperature measurements using a type S (Pt/Pt-10% Rh) thermocouple and an *ex situ* determination of the agglomerates' morphology distribution obtained through the analysis of transmission electron micrographs of thermophoretically-obtained samples.

Utilizing appropriate theoretical considerations and approximations ([1], [2], [3]), depolarized dynamic light scattering data can be combined with the depolarization ratio and either polarized DLS data from the same scattering angle or depolarized DLS data from a different scattering angle to infer the distributions of the agglomerates' Brownian translational and rotational diffusion coefficients. This information may conceivably be combined with the measured flame temperature and appropriate relationships between the Brownian diffusion coefficients and the agglomerate primary particle diameter and aspect ratio to infer the mean primary particle diameter and distribution of aspect ratios of the agglomerates at the measurement location within the flame. Such relationships between the Brownian diffusion coefficients and the agglomerate morphological parameters have been previously theoretically obtained for particles whose characteristic size is much larger than the mean free path of the surrounding gas (the *continuum regime*) ([1], [2], [4]). These relations, however, are not valid when the particle size is of the same order (or smaller) as the gas mean free path [5], a condition common within flames. Because the non-continuum effects on these diffusion coefficient relationships are not accurately known at the present time, the diffusion coefficient information obtained from the optical measurements are to be compared with the *ex situ* morphology information to obtain experimental data relating the Brownian diffusion coefficients to the agglomerate morphology. Such information would contribute to the development of a non-continuum model or empirical correlation relating the diffusion coefficients to the morphological parameters so that the morphological information can be directly inferred from future DLS experiments without the need for *ex situ* sampling and analysis.

The primary motivation for the use of dynamic light scattering is that these non-intrusive measurements exhibit little or no dependence upon the typically unknown refractive index of the particles being measured ([6], [7]). Previous DLS flame studies (see eg. [6], [8], [9], [10], [11], [12]) have relied exclusively on polarized (VV) measurements, in which the incident and detected light are both vertically polarized with respect to the (horizontal) *scattering plane*, which is defined by the propagation directions of the incident and detected light. These polarized DLS studies, however, typically assume that the scattering particles are spherical because the overwhelming dependence of polarized DLS data on the isotropic part of the scatterers' polarizability tensor permits the accurate determination of the translational diffusion coefficient only. This permits the extraction of an equivalent-sphere radius.

This investigation extends the previous DLS flame studies by incorporating the anisotropic effects obtained from depolarized(VH) dynamic light scattering measurements. Such measurements are made possible only by the recent improvements in the minimum sample time of the digital correlators (down to 10 - 25 ns) used to record and process DLS data. The rotational decay times of flame-borne agglomerates, which can range from 10 to 100 ns or less, are typically too fast to provide a meaningful signal when the scattered light is processed by older correlators, whose minimum sample times were often 100 ns or longer. With the additional depolarized information, the nonspherical nature of straight chain agglomerates can be represented through the determination of a distribution of agglomerate aspect ratios in addition to the mean primary particle diameter based upon the determination of both the Brownian translational and rotational diffusion coefficients from the DLS data. Since straight-chain agglomerates are the simplest form of anisotropic agglomerate structure, the development and adaptation of light scattering methods for measuring the morphological parameters of this agglomerate type offers a step towards the broader objective of developing optical techniques to measure the properties of arbitrary structures.

2. Apparatus

The apparatus utilized in this study consists of a concentric-tube diffusion burner, which generates the seeded flame described above, a thermophoretic sampling system for extracting *ex situ* samples from the flame, and a customized light scattering spectrometer for performing the optical measurements.

The concentric-tube diffusion burner, which is illustrated in figure 1, is constructed of three concentric stainless steel tubes. The fuel (CO) flows through the central 1/2" i.d. tube, emerging to combust with either room air or an annulus of O₂ emerging from the cylindrical gap surrounding the central tube. The outer tube provides an outlet for an inert shroud gas, such as N₂, which can be used prevent entrainment of the surrounding air into the flame. The CO fuel is seeded with iron pentacarbonyl (Fe(CO)₅) upstream of the burner by diverting a portion of the CO flow through a temperature-regulated cylinder containing 200 ml of liquid Fe(CO)₅ and subsequently combining the diverted stream with the main CO stream. Bubbling the diverted CO flow through the iron pentacarbonyl bath causes partial saturation of the diverted flow with the volatile Fe(CO)₅. The tubing between the Fe(CO)₅ bath and the burner is electrically heated to an average temperature of 102°C to minimize condensation of the iron pentacarbonyl on the tube walls. The resulting flame is stabilized and anchored by a ceramic honeycomb (196 cells per square inch) mounted above the burner.

A thermophoretic probe ([13], [14]) is used to collect samples from the flame for an *ex situ* determination of the distribution of agglomerate morphological parameters. The probe actuator inserts a room temperature 20 x 4 x 0.4 mm stainless steel strip into the flame for a time period ranging from 75 ms to 200 ms. The temperature gradient induced in the flame gases between the room temperature probe and the hot flame gases propels the flame-borne particles towards the probe due to the momentum imbalance of the molecules impacting the particles from the hot and cold sides. This phenomenon, called *thermophoresis* ([15], [16]), causes the agglomerates to deposit on a carbon coated copper grid, which is attached to the probe strip. The particles collected on this grid are subsequently examined using a transmission electron microscope (TEM). Disturbances to the flame are minimized by orienting the probe parallel to the flame's streamlines and by shielding the flame from air currents induced by the rapidly moving mechanism by placing a slotted plate between the actuator mechanism and the flame. Theoretically, this sampling technique does not bias the distribution of morphological parameters [17] and it also minimizes the possibility of post-sampling agglomeration and reaction. It is thus an extremely effective available *ex situ* sampling technique for morphological studies [14].

The optical system, which is pictured in Figure 2, is a light scattering spectrometer of fairly standard design [18]. An argon ion laser beam (from a Spectra Physics 2085A-20 laser) is directed through a focusing lens L1, an aperture D1, and a polarizer P into the particle-laden flame to provide a focused, vertically-polarized, coherent light source for scattering by the agglomerates. The light scattered at a scattering angle θ from the direction of the incident beam is again polarized by the analyzer A (either in the vertical plane for VV detection or the horizontal plane for VH detection) before being focused by the collector lens L2 onto the plane of aperture D3. A photomultiplier tube PMT

(Thorn EMI 9863B/350), whose photocathode is immediately behind aperture D3, converts the photons into current pulses, which are subsequently discriminated from low level noise by a preamplifier/discriminator PAD (Brookhaven BIC 10056). The PAD's output pulses are then sent to a Brookhaven BI-9000AT digital correlator CORR, which generates the following correlation function [19]:

$$G(\tau_j) = \frac{1}{N} \sum_{i=1}^N n_i n'_{i-j} \quad (j = 1, 2, 3, \dots, M), \quad (1)$$

where n_i and n'_{i-j} are the respective numbers of photon pulses received at correlator inputs A and B during sample times Δt centered at times t_i and $t_i - \tau_j$ (with τ_j being the j th delay time), N is the number of products in the summation, and M is the total number of correlator channels. The detection system apertures D2 and D3 respectively serve to define the effective detector area and the width of the *scattering volume* of illuminated particles seen by the detector. A laser line filter is also incorporated within the detection optics to eliminate the detection of light outside the wavelength band of 488 ± 1 nm. The high voltage power supply HVPS shown in figure 2 is needed by the PMT so that the photocurrent pulses can be amplified to detectable levels between its series of dynodes.

In addition to the single-detector autocorrelation scheme shown in figure 2, a two detector cross-correlation technique is also considered. As shown in figure 3, this alternative detection system uses a nonpolarizing dielectric cube beam splitter (Newport 05BC16NP.2) to direct the scattered light into two separate photomultiplier tubes. The resulting discriminated signals are fed into the A and B inputs of the correlator, which cross-correlates them. This detection scheme, as described by Phillies [20], minimizes the effects of afterpulsing and deadtime on the correlation function because for any given scattered light intensity, the specific arrival times of photons detected any PMT is independent of the photon arrival times at the other PMT. Because both afterpulsing and dead time effects are triggered by the arrival of individual photons at a detector surface, this lack of correlation between the photon arrival times at the different detectors greatly reduces the afterpulsing and dead time effects on the cross-correlation function. Some higher-order afterpulsing and deadtime effects may still be present, however, because the probability of detecting a photon, which is proportional to the detected intensity, is correlated between the two detectors. The main disadvantage of this detection method is that the scattered light intensity detected by each detector is less than half of the intensity detected by a single detector in the autocorrelation mode. Thus, the experimental duration time required to obtain the same signal-to-noise ratio in cross-correlation experiments as obtained in autocorrelation experiments must be increased by at least a factor of four, according to the theoretical uncertainty results of Jakeman, *et al.* [21].

3. System Tests and Preliminary Results

The initial tests of the optical system involved performing measurements on a portion of the incident laser light scattered off a stationary surface into the detector under various conditions. These static light experiments were used to select an appropriate supply voltage for the photomultiplier tubes, check the linearity of the detection system, and detect afterpulsing and deadtime errors in the measured correlation function.

The most appropriate supply voltage for the PMT's was determined by measuring the detected count rate as a function of supply voltage at a constant laser intensity. When plotted on a semi-log graph, as in figure 4, the count rate versus supply voltage curve resembles a plateau, with the count rate increasing rapidly with increasing voltage at lower voltages and leveling to a nearly constant value at higher voltages. The optimum supply voltage is chosen as the voltage at which the log count rate versus voltage curve flattens [22]. This insures that the amplitudes of most of the photon-induced current pulses from the photomultiplier are of sufficient amplitude to be recognized as photoelectric pulses by the preamplifier/discriminator and that errors and fluctuations in the supply voltage have a minimal effect on the detected photon count rate. For both PMT's the operating voltage was determined to be approximately 1865 V. Measuring the count rate at various laser powers subsequently confirmed an approximate linear relationship between these two quantities, in accordance with theoretical expectations [22].

In order to check optical system errors in generating a simple correlation function, the digital correlator was used to establish the time-based correlation function of the detected static laser light. The theoretical correlation function of a constant intensity source, such as the static laser light, should exhibit no variation with delay time (ie. it should be a flat line). Figure 5 depicts the normalized autocorrelation function of static light photon counts detected by a single detector with the optical configuration of figure 2. This correlation function exhibits systematic noise present from 0.025 μ s to approximately 2 μ s. Initial polarized single-detector DLS measurements from an iron-pentacarbonyl-seeded CO/air diffusion flame demonstrate similar noise in the initial channels of the resulting correlation function, as shown in figure 6. A comparison of figure 5 with figure 6 reveals that the noise trends are nearly identical, indicating a systematic error resulting either from afterpulsing and deadtime in the detection system or high-frequency correlated intensity fluctuations in the laser.

In order to determine the source of this systematic noise, the system was modified to incorporate the two-detector arrangement of figure 3. The resulting normalized static light cross-correlation function is shown in figure 7. This correlation function was measured under the same conditions as the autocorrelation function of figure 5 and is plotted on the same scale for ease of comparison. Figure 7 demonstrates a dramatic reduction in the systematic noise present in the 0.025 μ s to 2 μ s range in the static light correlation function. The noise is also noticeably absent from the polarized (VV) cross-correlation function depicted in figure 8, which was generated from the light scattered from a seeded flame. This result implies that the noise in the single-detector autocorrelation function was created by detection system effects, such as afterpulsing and deadtime, not the laser. Because the 0.025 μ s to 2 μ s delay time range is crucial for accurate determination of the depolarized DLS correlation function from the flame-borne agglomerates (due to its expected rapid decay time), the reduction of systematic noise within this range outweighs the

disadvantages incurred by the reduction of signal resulting from splitting the scattered beam into two beams prior to detection.

Since the intensity of the scattered light's depolarized component is typically much less than its polarized component (by a factor of 10^{-2} or less for agglomerates occurring in the presently-studied flame), the conditions necessary for obtaining a depolarized correlation function with an acceptable signal-to-noise ratio are much more extreme than those required for polarized DLS. Based upon preliminary measurements in conjunction with the theoretical uncertainty results of Jakeman, *et al.* [21], accurate depolarized DLS measurements require an incident laser power on the order of several watts with experiment duration times of several hours (or more). Because particle deposition upon the burner surface and stabilizing honeycomb is observed to become problematic after a $\text{Fe}(\text{CO})_5$ -seeded $\text{CO}-\text{O}_2$ flame is permitted to burn for longer than approximately 5 minutes, an accurate depolarized correlation function cannot be obtained by collecting the data continuously. Therefore, the correlator has been programmed to accumulate correlation function and count rate data over consecutive 30 second intervals, storing the data accumulated within each interval as separate data files. This permits the cessation of data acquisition every 5 minutes to permit cleaning of the burner surface and stabilizing honeycomb. The resulting multiple correlation functions are then combined into a single correlation function whose effective duration time is the sum of the duration times of the individual correlation functions. This technique permits the effective accumulation of DLS data for arbitrarily long duration times while preventing the alteration of the flame conditions due to excessive particle deposition. This technique also facilitates the experimental estimation of the standard deviation of each point on the combined correlation function, which can be used to determine an effective weighting function for the application of a distribution analysis routine, such as Provencher's CONTIN ([23], [24], [25]).

Figures 8 and 9 depict preliminary polarized and depolarized correlation functions of photons scattered from the seeded flame. The total CO flowrate was 0.50 lpm, with 25 mlpm diverted through a room temperature (297 K) bath of iron pentacarbonyl prior to burning. A 0.25 lpm oxygen flow was established around the seeded CO stream to facilitate rapid combustion and oxidation of the iron pentacarbonyl. No shroud was used because it caused instabilities in the flame. The stabilizer and measurement heights were 45 mm and 35 mm, respectively. The light scattering measurements were performed at a scattering angle of 5° with an incident laser power of approximately 1 W at a wavelength of 488 nm. The total duration time of the polarized (VV) correlation function shown in figure 8 was 5 minutes. The total duration time of the depolarized (VH) correlation function depicted in figure 9 was 2 hours. The polarized DLS measurement resulted in a reasonably noise-free correlation function that decays to its baseline at approximately $80 \mu\text{s}$. The noise present in this VV correlation function can be easily reduced by extending the duration time. The VH correlation function exhibits much more noise, even though the total duration time was 24 times longer than the duration time of the VV correlation function. Though the noise level is too great for a reliable distribution analysis using algorithms like CONTIN, definite trends do exist in the depolarized correlation function: it decays from an initial value of approximately 0.19 at $\tau = 0.025 \mu\text{s}$ to its baseline at approximately $\tau = 0.5 \mu\text{s}$. The significant temporal variations of the depolarized correlation function occur entirely within the range of delay

times that would have been significantly plagued by afterpulsing and deadtime had the single-detector autocorrelation scheme been used.

4. Summary and Conclusion

In order to extend currently existing techniques of measuring the morphological parameters of flame-generated agglomerates using non-intrusive light scattering techniques, an experiment has been developed to measure both the polarized and depolarized correlation functions of laser light scattered from straight chain agglomerates occurring within an iron-pentacarbonyl-seeded CO-O₂ flame. The objective is to obtain distribution functions of the Brownian translational and rotational diffusion coefficients from these correlation functions for comparison with flame temperature measurements and an independent *ex situ* determination of the distribution of the agglomerates' morphological parameters. With this information, experimental data relating the diffusion coefficients to the agglomerate morphological parameters within the non-continuum flame environment can be obtained. Accurate knowledge of this relationship could be used to determine agglomerate morphology distributions directly from dynamic light scattering and flame temperature measurements without the need for intrusive *ex situ* measurements. Preliminary testing of the apparatus indicates the possibility of obtaining both optical polarized and depolarized correlation functions from a flame if the output of two detectors viewing the same scattering volume are cross-correlated to eliminate unwanted detection system errors, such as afterpulsing and dead time. Under the conditions tested, the minimum sample time of the correlator used to process the data must be shorter than 100 ns in order to resolve the temporal variations of the rapidly-decaying depolarized correlation function. Furthermore, the reduction of noise is a major difficulty in measuring the depolarized correlation function and requires high laser power (several watts), long experimental duration times (several hours), and scattering particles exhibiting strong optical anisotropy (depolarization ratios greater than 10⁻³). Continuing work is underway to increase the signal-to-noise ratio of the measured depolarized correlation function and integrate the results with the flame temperature and *ex situ* morphology measurements.

5. References

- [1] Waguespack, G. PhD studies (in progress). ME Department, Louisiana State University.
- [2] Berne, B. J., and Pecora, R., *Dynamic Light Scattering with Applications to Chemistry, Biology, and Physics*. Wiley, New York, 1976.
- [3] Kerker, M., *The Scattering of Light and Other Electromagnetic Radiation*. Academic Press, New York, 1969.
- [4] Perrin, P. F., *J. Phys. Rad.* 5: 497 - 511 (1934).
- [5] Dahneke, B. E., *J. Aerosol Sci.* 4: 139 - 145 (1973).
- [6] Penner, S. S., Bernard, J. M., and Jerskey, T., *Acta Astron.* 3: 69 - 91 (1976).
- [7] Charalampopoulos, T. T., *Prog. Energy Combust. Sci.* 18: 13 - 45 (1992).
- [8] Penner, S. S., Bernard, J. M., and Jerskey, T., *Acta Astron.* 3: 93 - 105 (1976).
- [9] Penner, S. S., and Chang, P. H. P., in *Combustion in Reactive Systems* (J. R. Bowen, A. K. Openheim, and R. I. Soloukhin, eds.), *Progress in Astronautics and Aeronautics* 76 AIAA, New York, 1981, pp. 1 - 30.
- [10] King, G. B., Sorensen, C. M., Lester, T. W., and Merklin, J. F., *AIAA/ASME 3rd Joint Thermophysics, Fluids, Plasma, and Heat Transfer Conference*. (1982).
- [11] King, G. B., Sorensen, C. M., Lester, T. W., and Merklin, J. F., *Phys. Rev. Lett.* 50: 1125 - 1128 (1983).
- [12] Charalampopoulos, T. T., and Chang, H., *Combust. Sci. and Tech.* 59: 401 - 421 (1988).
- [13] Zhang, Z., *Controlled Combustion Synthesis of Iron Oxide Nanoparticles*. Masters Thesis, Louisiana State University, 1995.
- [14] Dobbins, R. A., and Megaridis, C. M., *Langmuir*. 3: 254 - 259 (1987).
- [15] Waldmann, L., *Z. Naturforsch.* 14a: 589 (1959).
- [16] Brock, J. R., *J. Colloid Sci.* 17: 768 - 780 (1962).
- [17] Rosner, D. E., Mackowski, D. W., and Garcia-Ybarra, P., *Combust. Sci. and Tech.* 80: 87 - 101 (1991).
- [18] Ford, N. C., in *Dynamic Light Scattering - Applications of Photon Correlation Spectroscopy*. (R. Pecora, ed.), Plenum Press, New York, 1985.
- [19] Brookhaven Instruments Corporation, *Instruction Manual for dModel BI-9000AT Digital Correlator*. 1993.
- [20] Phillips, G. D. J., in *Measurement of Suspended Particles by Quasi-Elastic Light Scattering*. (B. E. Dahneke, Ed.), Wiley, New York, 1985, pp. 291 - 326.
- [21] Jakeman, E., Pike, E. R., and Swain, S., *J. Phys. A: Gen. Phys.* 517 - 534 (1971).
- [22] THORN EMI Electron Tubes Ltd., *Photomultipliers*. 1986.
- [23] Russo, P. S., personal communications, Summer, 1996.
- [24] Provencher, S. W., *Comput. Phys. Commun.* 27: 213 - 227 (1982).
- [25] Provencher, S. W., *Comput. Phys. Commun.* 27: 229 - 242 (1982).

Material: 316 Stainless Steel

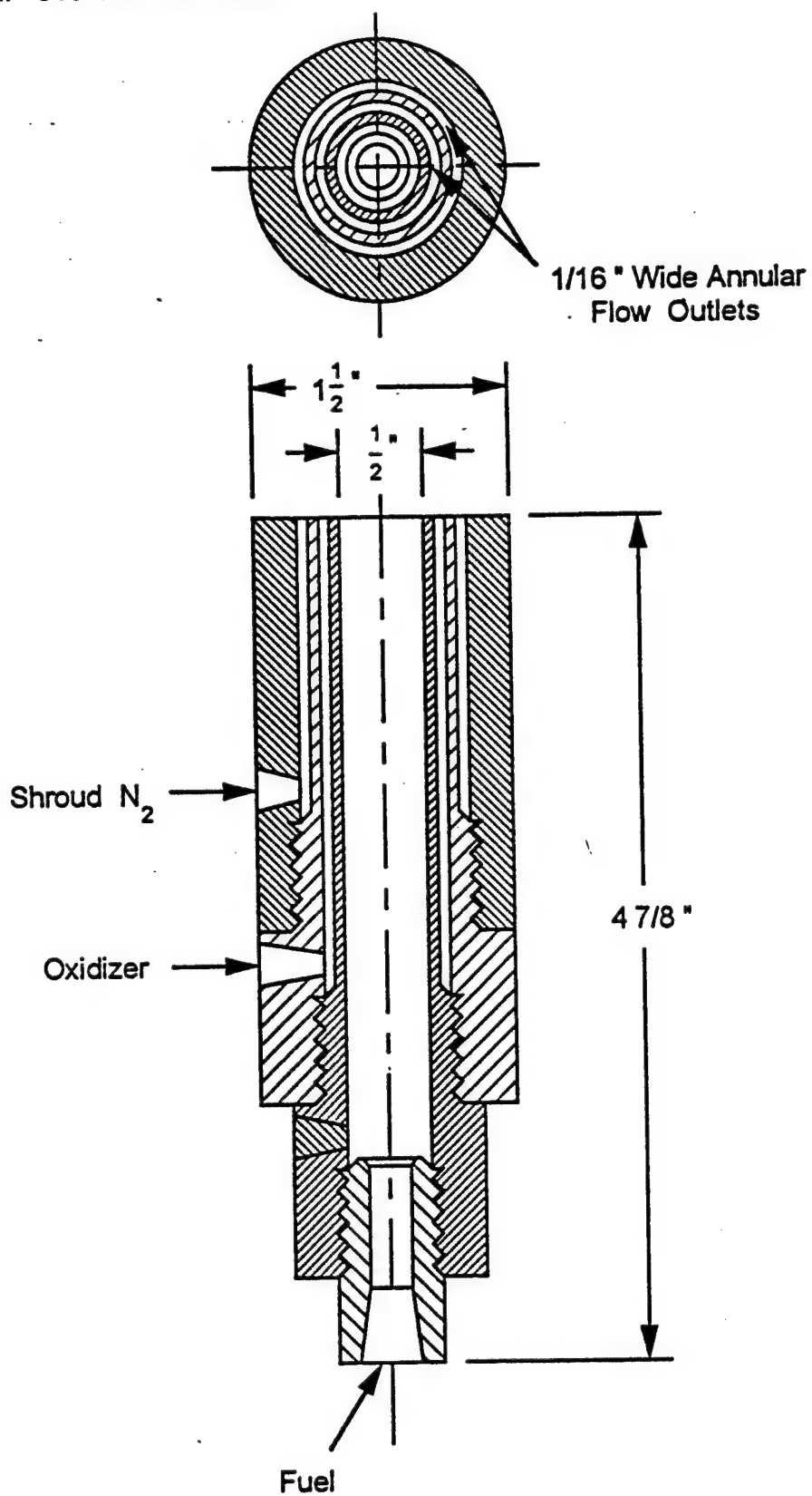


Figure 1: Concentric-tube diffusion burner.

TO OTHER
EXPERIMENTS

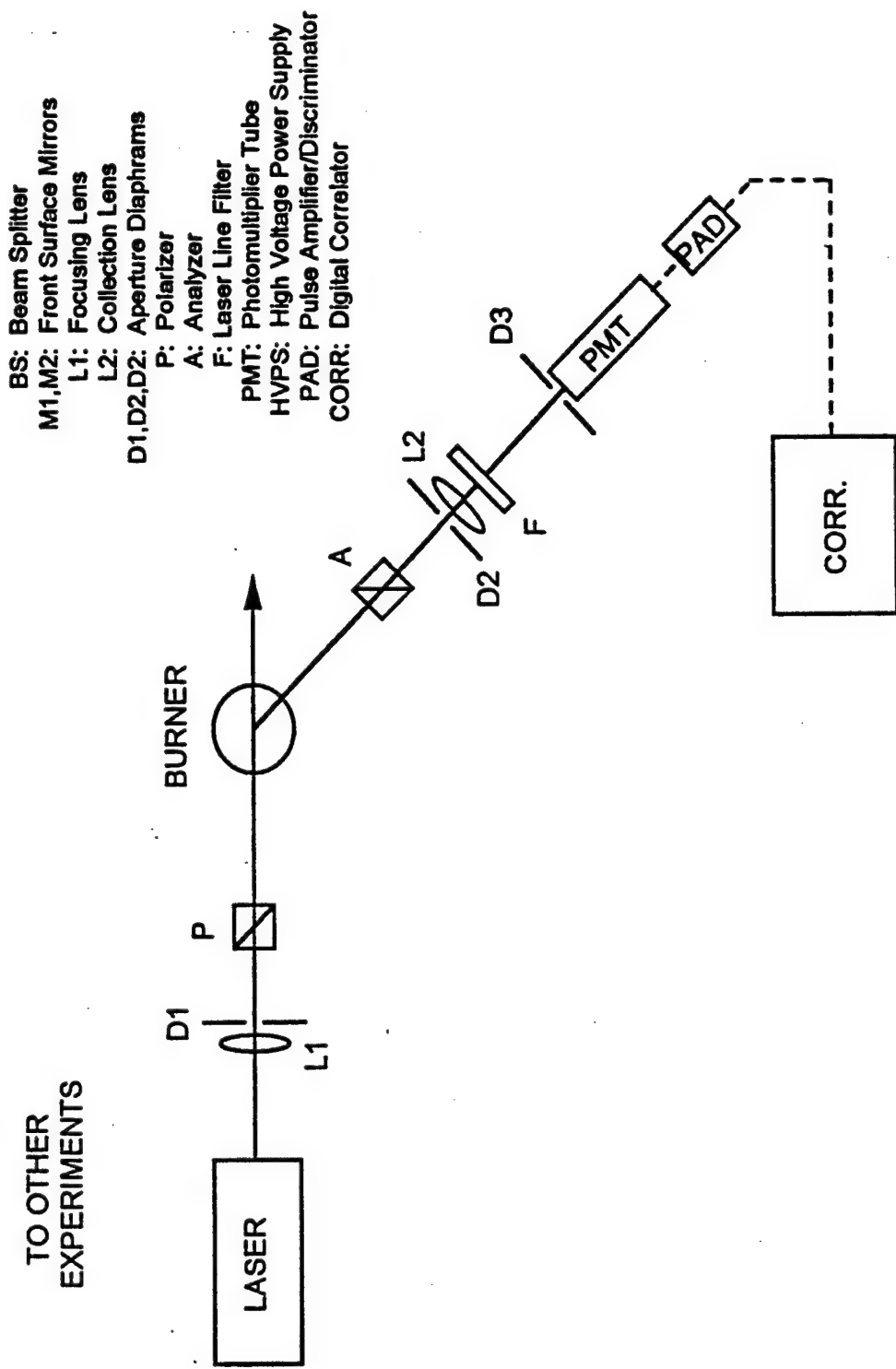


Figure 2: Schematic diagram of the optical measurement system.

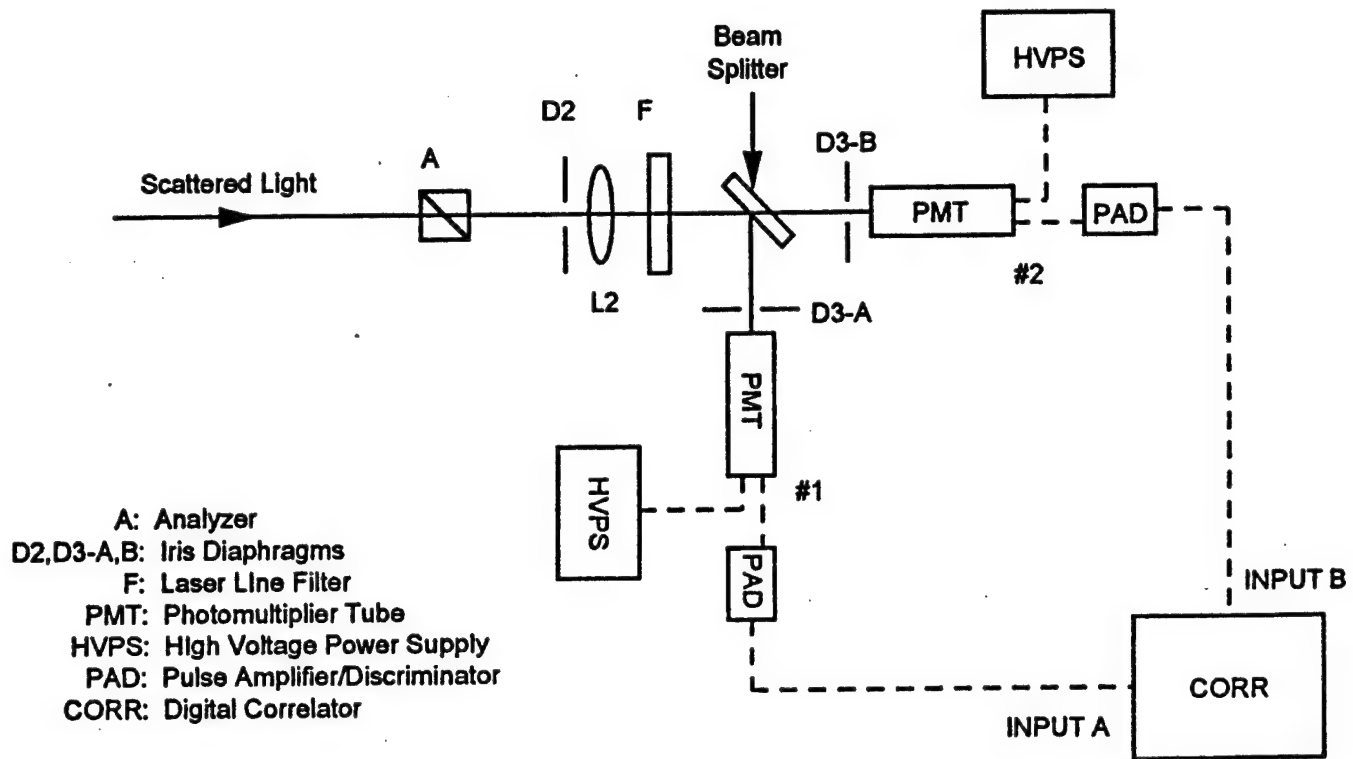


Figure 3: Schematic diagram of two-detector cross-correlation detection system.

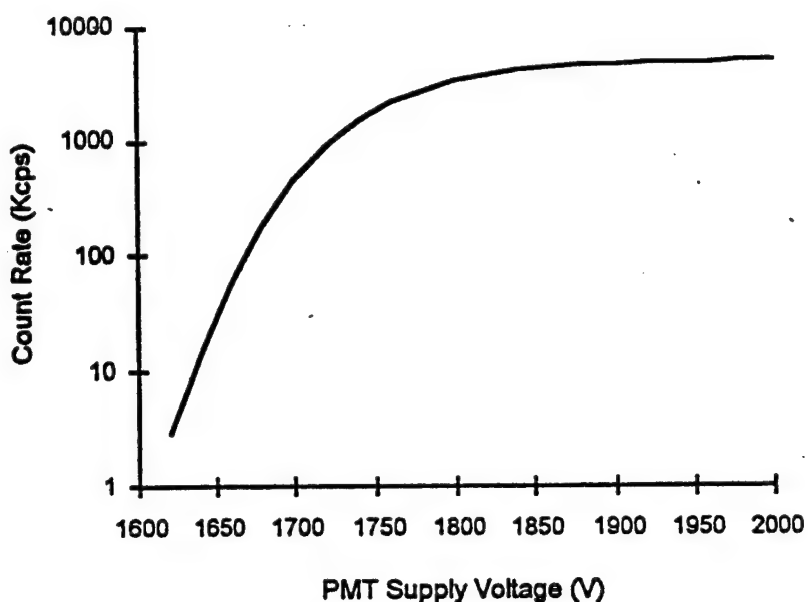


Figure 4: Experimental variation of measured count rate with PMT supply voltage for detection of a constant intensity light source.

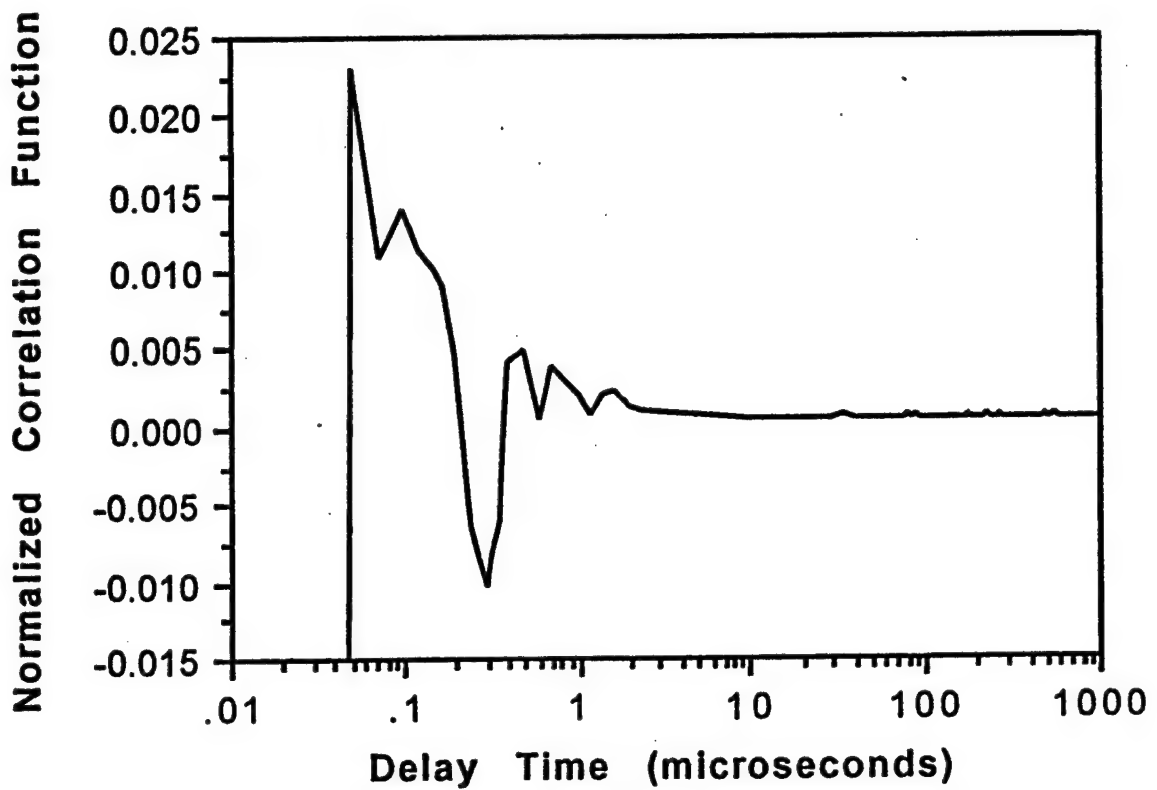


Figure 5: Normalized single-detector autocorrelation function of photons from a constant-intensity light source.

**Normalized
Correlation
Function**

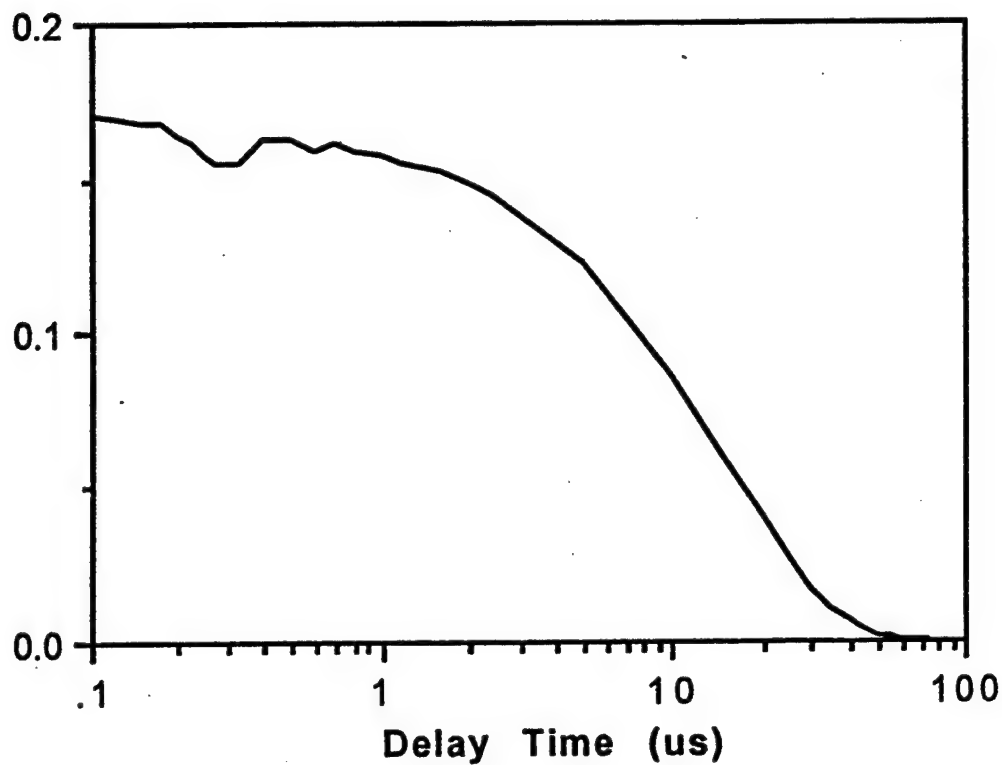


Figure 6: Normalized single-detector autocorrelation function of polarized (VV) light scattered from an iron-pentacarbonyl-seeded CO/room-air diffusion flame. (CO flow rate = 0.50 lpm; carrier CO flow rate = 20 mlpm; measurement height = 30 mm above burner surface; stabilizer position = 42 mm above burner surface)

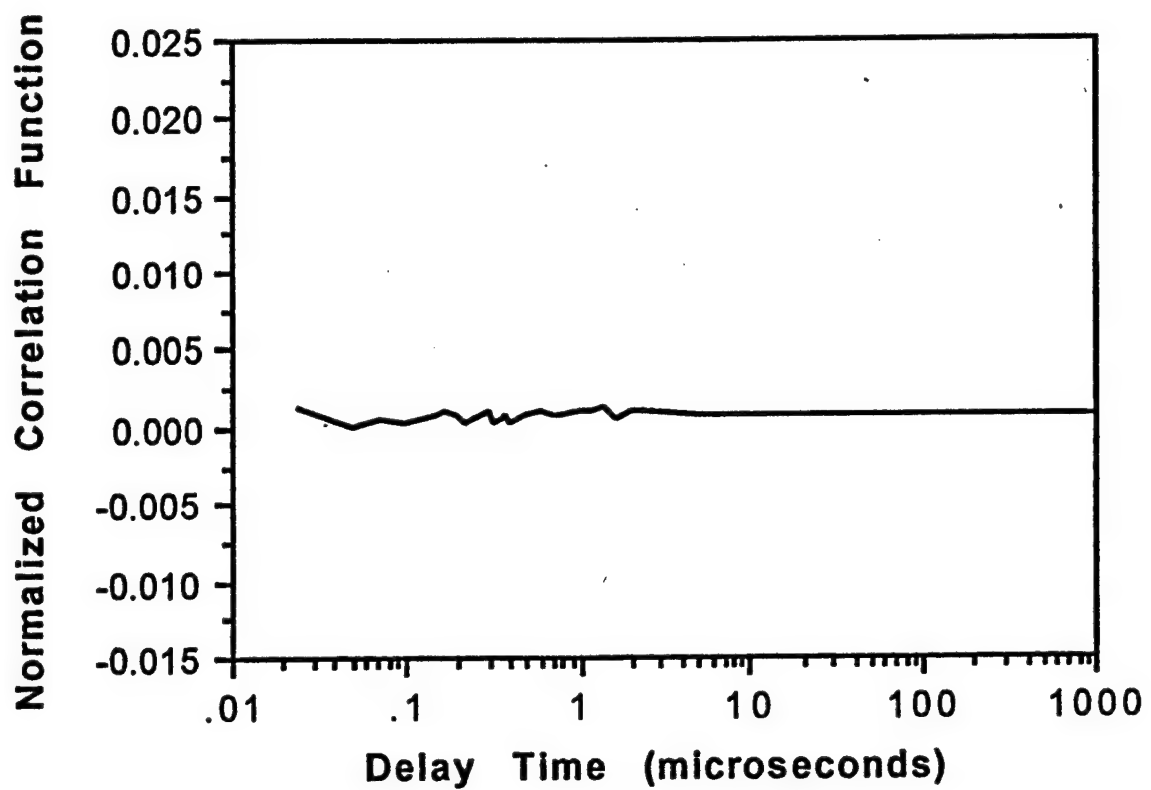


Figure 7: Normalized two-detector cross-correlation function of photons from a constant-intensity light source.

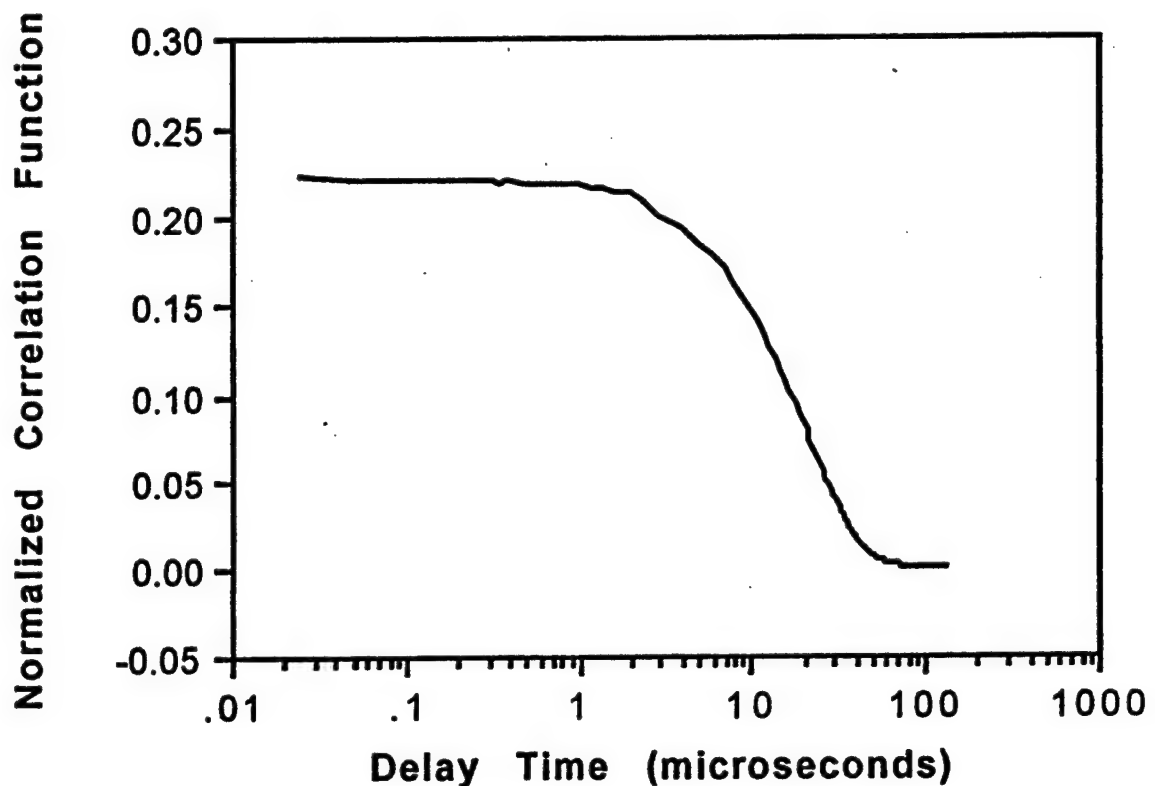


Figure 8: Normalized two-detector cross-correlation function of polarized (VV) light scattered from an iron-pentacarbonyl-seeded CO-O₂ diffusion flame. (CO flow rate = 0.50 lpm; carrier CO flow rate = 20 mlpm; O₂ flow rate = 0.25 lpm; measurement height = 35 mm above burner surface; stabilizer position = 45 mm above burner surface; duration time = 5 minutes)

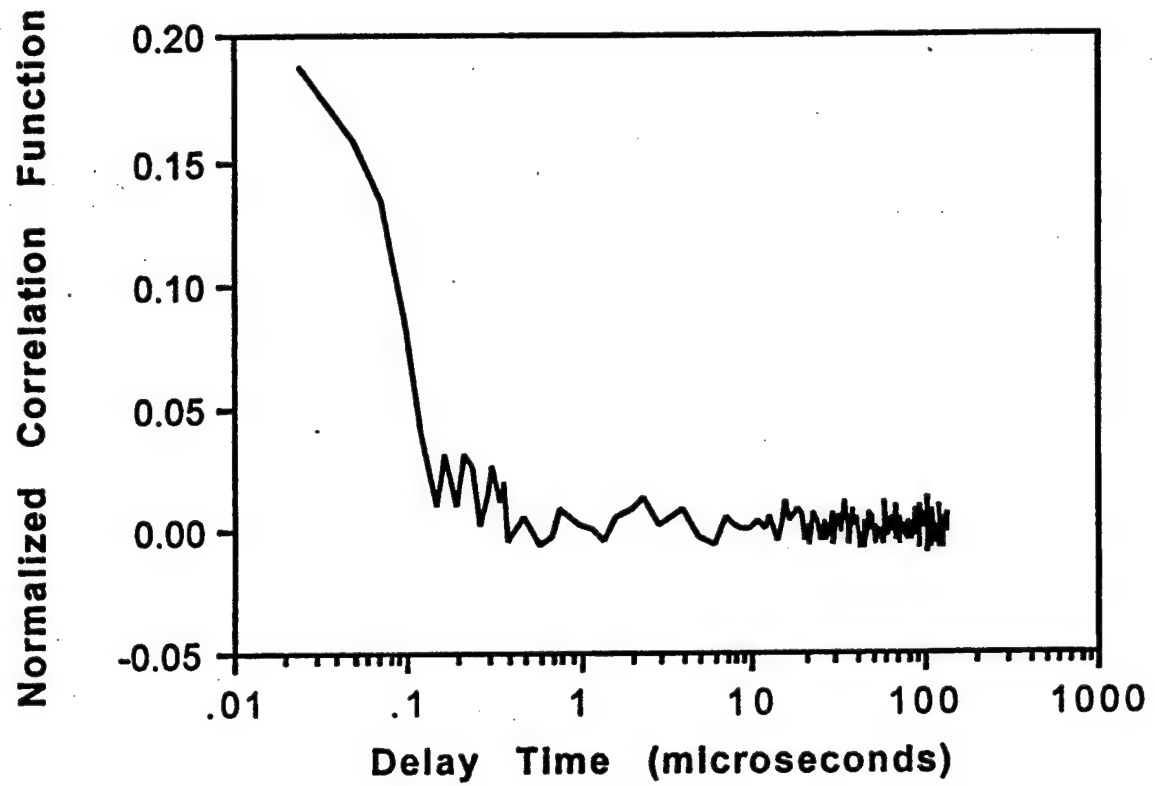


Figure 9: Normalized two-detector cross-correlation function of depolarized (VH) light scattered from an iron-pentacarbonyl-seeded CO-O₂ diffusion flame. (CO flow rate = 0.50 lpm; carrier CO flow rate = 20 mlpm; O₂ flow rate = 0.25 lpm; measurement height = 35 mm above burner surface; stabilizer position = 45 mm above burner surface; duration time = 2 hours)

VI. Sensitivity Considerations for the Use of Heterodyne Dynamic Light Scattering to Infer Velocities and Brownian Diffusion Coefficients of Agglomerates in a High Temperature Environment

1. Introduction and Motivation

Experimental determination of the morphology of flame-generated particulates within a flame environment is useful for soot-formation studies, radiative heat transfer computations from flames, and product monitoring in particulate synthesis applications [1]. Currently the available *in situ* methods for particulate morphology characterization, such as the fractal analysis technique [1], are limited because the data inversion requires knowledge of the particle refractive index, which in most cases is unknown. Thus, the objective of the ongoing research is to adapt the technique of depolarized dynamic light scattering (DDLS), which currently has widespread use in the characterization of macromolecules in solutions [2, 3, 4] and is independent of the particle refractive index for particles that are small in comparison to the incident laser wavelength, to the measurement of the dynamics of chain-like agglomerates within a reacting flame environment. Independent extractive sampling and subsequent transmission electron microscope (TEM) analysis of the flame-generated particulates would then provide valuable data on the relationship between the structure and non-continuum rotational dynamics of cylindrical particulates. Such information could be used to confirm any proposed theoretical models and to infer particulate structure information from experimentally determined rotational dynamics data.

In the case of zero-angle DDLS measurements, the incident laser beam is sent through the flame, which is located between crossed polarizers, and straight into the detector. Ideally, the only light actually reaching the detector would be the depolarized portion of the scattered light caused by the effective optical anisotropy resulting from the shape of the particulates. The autocorrelation function of the resulting detected intensity fluctuations would then contain rotational diffusion information, with no dependence on either the translational diffusion coefficient or the interparticle form factor [1, 2, 4]. Because the scattering volume for the zero-angle measurement intersects the entire width of the flame, the effects of velocity and temperature gradients within the diffusion flame should be considered. If these gradients significantly affect the measured correlation function, independent measurements of radial bulk particle velocity, as well as temperature, may become necessary for accurate data inversion. Since bulk particle velocity can theoretically be inferred from the results of a heterodyne DLS experiment, in which the scattered light is mixed with an unscattered beam (the local oscillator) prior to detection to establish a mutual beating signal [2, 3, 5, 6], the remainder of this section addresses this subject.

2. Experimental Considerations

Particles that are suspended within a fluid (solvent) medium typically undergo a variety of motions, both translational and rotational, that generally affect the temporal variation of light scattered from the particle. The particle motion is often governed by both deterministic and random forces. Deterministic particle translation, which is here characterized by a bulk or average velocity \mathbf{V} , is frequently the result of a variety of phoretic forces, such as thermophoresis, photophoresis, diffusiophoresis, or electrophoresis, in which a constant net force is applied to the particle and causes it to drift in the force's direction. Deterministic translation also results from Stoke's drag induced on the particle by a nonzero solvent velocity. Additionally, however, the dynamics of microscopic particles are often significantly affected by Brownian motion, which is caused by the random thermal variations of the momentum imparted to the particle by the solvent molecules. In its simplest form, Brownian translation is described by the following diffusion equation [2]:

$$\frac{\partial}{\partial t} G_S(\mathbf{R}, t) = D \nabla^2 G_S(\mathbf{R}, t), \quad (1)$$

where $G_S(\mathbf{R}, t)d^3R$ is the probability of finding the particle within the neighborhood d^3R of position \mathbf{R} at time t . The proportionality constant D is called the Brownian translational diffusion coefficient. Rotational Brownian motion is characterized by a similar probabilistic diffusion equation containing a Brownian rotational diffusion coefficient D_R [2]. Autocorrelating the intensity fluctuations of light scattered from these particles at different times permits the experimental determination of the magnitudes of these diffusion coefficients, which can then be theoretically related to the particles' size and aspect ratio. Additionally, if the scattered light is mixed with an unscattered reference beam, a beat signal is established between the two beams that provides information about the bulk particle velocity. These measurements are performed using the technique of dynamic light scattering (DLS). In a typical dynamic light scattering (DLS) experiment, polarized laser light is projected through a suspension of particulates. The resulting scattered light then passes through another polarizer (the analyzer) and is focused onto a photomultiplier tube (PMT). The PMT output is then processed and correlated by a preamplifier/discriminator and a digital autocorrelator to provide information about the temporal fluctuations of the scattered light, from which the particle dynamics can be inferred. Figure 1 depicts the scattering geometry used. The scattering plane is the plane defined by the directions of the incident and detected scattered beams, whose wave vectors are \mathbf{k}_i and \mathbf{k}_f , respectively. The angle between \mathbf{k}_i and \mathbf{k}_f is the scattering angle θ . The scattering vector $\mathbf{q} \equiv \mathbf{k}_i - \mathbf{k}_f$ thus has the magnitude

$$q = \frac{4\pi n}{\lambda} \sin\left(\frac{\theta}{2}\right), \quad (2)$$

where λ is the wavelength of the incident light and n is the refractive index of the surrounding medium. The basis vectors characterizing the polarization of the incident and scattered fields are defined to be parallel (horizontal) and perpendicular (vertical) to the scattering plane. Typically, the incident laser light is vertically polarized while the detected light is either vertically (for VV detection) or horizontally (for VH detection) polarized. The experimental apparatus is discussed in further detail by Ford [7].

The photomultiplier tube detects the individual photons of the scattered light, which are then discriminated from background noise using a preamplifier/discriminator. These photon pulses are then counted and processed by a digital autocorrelator, which evaluates the following correlation function [8]:

$$\langle n(0)n(\tau_j) \rangle = \lim_{N \rightarrow \infty} \frac{1}{N} \sum_{i=1}^N n_i n_{i-j}, \quad (j = 1, 2, \dots, M) \quad (3)$$

where n_i is the number of photons detected during sample time Δt centered at time t_i , n_j is the number of photons detected during Δt centered at time $t_i - \tau_j$, where τ_j is the j th delay time, and M is the number of correlator channels. Neglecting detection system effects such as afterpulsing, dead time, and dark current, the digital autocorrelation function is related to the normalized second order electric field autocorrelation function (for sample times much less than the correlation function's characteristic decay time [9]) by the following equation [3, 9, 10]:

$$\langle n(0)n(\tau) \rangle = \langle n(0) \rangle^2 \left\{ 1 + \frac{1}{N_c} [g^{(2)}(\tau) - 1] \right\} + \langle n(0) \rangle u(\tau), \quad (4)$$

where $\langle n(0) \rangle$ is the average number of photons counted during sample time Δt , N_c is the number of detected coherence areas [3, 6], $u(\tau)$ is a function whose value is unity for $\tau = 0$ and zero otherwise, $g^{(2)}(\tau)$ is the normalized second order electric field autocorrelation function with the definition

$$g^{(2)}(\tau) \equiv \frac{\langle |E(0)|^2 |E(\tau)|^2 \rangle}{\langle |E(0)|^2 \rangle^2}, \quad (5)$$

and $E(t)$ is the electric field at a point on the detector at time t . Equation (4) is obtained under the assumption that the first-order temporal correlation function of the energy flux within each coherence area is equal for all coherence areas. Additionally, use of the definition of $g^{(2)}(\tau)$ in equation (4) also relies on the validity of the assumption that the electric field is uniform within each coherence area. The first term on the right side of equation (4) contains the usable signal from which the dynamics of the scatterers can be extracted. The second term is a shot noise term

resulting from the Poisson nature of the photodetection process. When the correlation function is defined in terms of the detected photocurrent, the shot noise term is proportional to the dirac delta function $\delta(\tau)$ [11]. However, since the correlation function used in photon counting applications is formulated in terms of the number of photons counted during a finite sample time Δt , the shot noise term in this case is proportional to the finite step function $u(\tau)$ [9, 10].

For a heterodyne experiment where the intensity of the local oscillator I_{LO} is much larger than the average intensity i_s of the scattered field, $g^{(2)}(\tau)$ becomes [3, 7]:

$$g^{(2)}(\tau) = 1 + 2 \frac{\epsilon^2}{I_{LO}} \operatorname{Re}[I_1(\tau) \exp(i\omega_{LO}\tau)], \quad (6)$$

where $I_1(\tau) \equiv \langle E_s^*(0)E_s(\tau) \rangle$ is the first-order scattered electric field autocorrelation function, ω_{LO} is the angular frequency of the local oscillator, and ϵ^2 is the heterodyne mixing efficiency [3]. For a monodisperse suspension of spherical, optically isotropic particles, Penner, *et al.* [12] has evaluated $I_1(\tau)$, under the assumptions of particle independence and a spherically symmetric Gaussian incident intensity distribution, to be

$$I_1(\tau) = i_s \exp(i\mathbf{q} \cdot \mathbf{V}\tau) \exp(-q^2 D\tau) \exp\left(-\frac{V^2 \tau^2}{2\omega^2}\right) \exp(-i\omega_L \tau), \quad (7)$$

where \mathbf{V} is the bulk velocity of the particles, D is the particles' Brownian translational diffusion coefficient, ω is the radius of the scattering volume, and ω_L is the angular frequency of the scattered (and incident) light.

Substitution of equation (7) into equations (4) and (6) gives (for $\omega_{LO} = \omega_L$):

$$\langle n(0)n(\tau) \rangle = \langle n(0) \rangle^2 \left[1 + 2 \frac{\epsilon^2}{N_c} \frac{i_s}{I_{LO}} \cos(\mathbf{q} \cdot \mathbf{V}\tau) \exp(-q^2 D\tau) \exp\left(-\frac{V^2 \tau^2}{2\omega^2}\right) \right] + \langle n(0) \rangle u(\tau). \quad (8)$$

When $\omega/V \gg 1/q^2 D$, the last exponential factor is negligible because its decay is much slower than the decay of the other terms in equation (8). Assuming that both the baseline $\langle n(0) \rangle^2$ and the constant in front of the cosine factor are experimentally known and that the Gaussian term decays much slower than the other terms, the heterodyne correlation function can be normalized into the form:

$$g(\tau) = \cos(A\tau) \exp(-\Gamma\tau), \quad (\text{for } \tau > 0) \quad (9)$$

where $A \equiv q \cdot V$ and $\Gamma \equiv q^2 D$.

3. Conditions for Particle Velocity and Size Inference from the Heterodyne Correlation Function

An analysis of the variance of the constants A and Γ inferred from normalized correlation function data $g_m(\tau_i)$, which is obtained at M discrete delay times τ_i ($i = 1, 2, \dots, M$), provides the basis of a criterion that can be used to select a range of scattering angles that permits the inference of A and Γ with a percent uncertainty equal to or less than the uncertainty of the normalized raw data $g_m(\tau_i)$. The data inversion is assumed to take the form of a least squares analysis: finding the parameters A and Γ that minimize the function $\epsilon^2 \equiv \sum [g_m(\tau_i) - g(\tau_i)]^2$. The following theoretical analysis utilizes a small perturbation approximation to determine the effects of the statistical uncertainty of the measured correlation function $g_m(\tau)$ on the statistical uncertainty of the least squares estimations of the parameters A and Γ .

To facilitate this analysis, $g_m(\tau_j)$ is decomposed as follows:

$$g_m(\tau_j) = g(\tau_j) + \sigma(\tau_j), \quad (10)$$

where $g(\tau_j)$ is the value of the theoretical normalized correlation function at delay time τ_j and $\sigma(\tau_j)$ is the deviation of the correlation function's measured value from its theoretical value at τ_j . This decomposition assigns all of the statistical uncertainties associated with the measurement to the random function $\sigma(\tau_j)$. The theoretical correlation function $g(\tau_j)$ is therefore a deterministic function.

Utilization of a least squares analysis to determine the unknown parameters A and Γ from a set of raw data involves determining the values of A and Γ that minimize the function

$$\epsilon^2 \equiv \sum_{j=1}^M [g_m(\tau_j) - g(\tau_j)]^2 = \sum_{j=1}^M [g_m(\tau_j) - \cos(A\tau_j) \exp(-\Gamma\tau_j)]^2, \quad (11)$$

where M is the number of correlator channels. In this case the values of A and Γ that correspond to the minimum of ϵ^2 are found by solving the equations formed by setting the partial derivatives of ϵ^2 with respect to A and Γ equal to zero:

$$\sum_{j=1}^M [g_m(\tau_j) - \cos(A\tau_j)\exp(-\Gamma\tau_j)] \tau_j \sin(A\tau_j) \exp(-\Gamma\tau_j) = 0 \quad (12a)$$

and

$$\sum_{j=1}^M [g_m(\tau_j) - \cos(A\tau_j)\exp(-\Gamma\tau_j)] \tau_j \cos(A\tau_j) \exp(-\Gamma\tau_j) = 0 \quad (12b)$$

For the case where $g_m(\tau_j)$ follows the form of the theoretical curve exactly ($g_m(\tau_j) = \cos(A_0\tau_j) \exp(-\Gamma_0\tau_j)$, $j = 1, 2, \dots, M$) the computed least squares parameters take the values $A = A_0$ and $\Gamma = \Gamma_0$. When $g_m(\tau_j)$ deviates from the theoretical curve by the random quantity $\sigma(\tau_j)$ (ie. $g_m(\tau_j) = \cos(A_0\tau_j) \exp(-\Gamma_0\tau_j) + \sigma(\tau_j)$, $j = 1, 2, \dots, M$) the computed least squares parameters differ from the values A_0 and Γ_0 by δA and $\delta \Gamma$. Thus, for this more general case $A = A_0 + \delta A$ and $\Gamma = \Gamma_0 + \delta \Gamma$. By substituting $g_m(\tau_j) = \cos(A_0\tau_j) \exp(-\Gamma_0\tau_j) + \sigma(\tau_j)$, $A = A_0 + \delta A$, and $\Gamma = \Gamma_0 + \delta \Gamma$ into equations (12) and assuming that the order of magnitudes $O[\sigma(\tau_j)] = O[\delta A] = O[\delta \Gamma] \ll 1$, equations (12) are approximated by their first order terms in $\sigma(\tau_j)$, δA , and $\delta \Gamma$:

$$\sum_{j=1}^M \{ \sigma(\tau_j) + \tau_j [\delta \Gamma \cos(A_0\tau_j) + \delta A \sin(A_0\tau_j)] \} \exp(-\Gamma_0\tau_j) \tau_j \cos(A_0\tau_j) \exp(-\Gamma_0\tau_j) = 0 \quad (13a)$$

and

$$\sum_{j=1}^M \{ \sigma(\tau_j) + \tau_j [\delta \Gamma \cos(A_0\tau_j) + \delta A \sin(A_0\tau_j)] \} \exp(-\Gamma_0\tau_j) \tau_j \sin(A_0\tau_j) \exp(-\Gamma_0\tau_j) = 0. \quad (13b)$$

The coefficients of the perturbation parameters δA and $\delta \Gamma$ in the above equations are linear combinations of the sums

$$\sum_{j=1}^M \tau_j^2 \cos(2A_0\tau_j) \exp(-2\Gamma_0\tau_j), \quad \sum_{j=1}^M \tau_j^2 \sin(2A_0\tau_j) \exp(-2\Gamma_0\tau_j), \quad \text{and} \quad \sum_{j=1}^M \tau_j^2 \exp(-2\Gamma_0\tau_j).$$

The first two of these sums are the real and imaginary parts of

$$\xi = \sum_{j=1}^M \tau_j^2 \exp[-2(\Gamma_0 - iA_0)\tau_j], \quad (14)$$

while the last sum is

$$\sum_{j=1}^M \tau_j^2 \exp(-2\Gamma_0\tau_j) = \xi_0 = \lim_{A_0 \rightarrow 0} \xi. \quad (15)$$

Solving equations (13) for δA and $\delta \Gamma$ and expressing the results in terms of ξ and ξ_0 gives the following relationships:

$$\delta A = 2 \frac{[\xi_0 + \operatorname{Re}(\xi)] \sum_{j=1}^M \tau_j \sigma(\tau_j) \sin(A_0 \tau_j) \exp(-\Gamma_0 \tau_j) - \operatorname{Im}(\xi) \sum_{k=1}^M \tau_k \sigma(\tau_k) \cos(A_0 \tau_k) \exp(-\Gamma_0 \tau_k)}{|\xi|^2 - \xi_0^2}$$

and (16a,b)

$$\delta \Gamma = 2 \frac{[\xi_0 - \operatorname{Re}(\xi)] \sum_{j=1}^M \tau_j \sigma(\tau_j) \cos(A_0 \tau_j) \exp(-\Gamma_0 \tau_j) - \operatorname{Im}(\xi) \sum_{k=1}^M \tau_k \sigma(\tau_k) \sin(A_0 \tau_k) \exp(-\Gamma_0 \tau_k)}{|\xi|^2 - \xi_0^2}.$$

By computing the statistical averages of the squares of equations (16), first-order perturbation approximations of the variances of the least-squares-inferred quantities A and Γ are obtained. Squaring the expressions for δA and $\delta \Gamma$ produces terms involving products of the form $\sigma(\tau_j)\sigma(\tau_k)$; therefore, evaluation of the variances of A and Γ requires knowledge of the covariance matrix $\operatorname{Cov}[\sigma(\tau_j), \sigma(\tau_k)] = \langle \sigma(\tau_j)\sigma(\tau_k) \rangle$. If the mean value of the measured correlation function $g_m(\tau_j)$ is equal to $g(\tau_j)$ [$= \cos(A_0 \tau_j) \exp(-\Gamma_0 \tau_j)$] for all delay times τ_j , then $\operatorname{Cov}[\sigma(\tau_j), \sigma(\tau_k)] = \operatorname{Cov}[g_m(\tau_j), g_m(\tau_k)]$.

If the covariance matrix is approximated as $\langle \sigma(\tau_j)\sigma(\tau_k) \rangle = \operatorname{Cov}[g_m(\tau_j), g_m(\tau_k)] = \sigma^2 \delta_{jk}$, where σ^2 is the variance of the normalized experimental data, which is assumed to be independent of the delay time τ_j , then the variances computed using the expressions for δA and $\delta \Gamma$ given by equations (16) are

$$\text{Var}(A) \equiv \langle (\delta A)^2 \rangle = 2 \sigma^2 \frac{\xi_0 + \text{Re}(\xi)}{|\xi|^2 - \xi_0^2} \quad (17a)$$

and

$$\text{Var}(\Gamma) \equiv \langle (\delta \Gamma)^2 \rangle = 2 \sigma^2 \frac{\xi_0 - \text{Re}(\xi)}{|\xi|^2 - \xi_0^2} \quad (17b)$$

Nondimensionalization of these variances produces the following expressions:

$$\frac{\text{Var}(A)}{\sigma^2 A^2} = \frac{1}{2\pi^2 \chi^2} \frac{\gamma_0 + \text{Re}(\gamma)}{\gamma_0^2 - |\gamma|^2} \quad \text{and} \quad \frac{\text{Var}(\Gamma)}{\sigma^2 \Gamma^2} = \frac{2}{(\gamma_0)^2} \frac{\gamma_0 - \text{Re}(\gamma)}{\gamma_0^2 - |\gamma|^2} \quad (18a,b)$$

where

$$\gamma = \frac{\xi}{(\Delta t)^2} = \sum_{j=1}^M T_j^2 \exp[-2\chi(r - i2\pi)T_j] \quad (19a)$$

and

$$\gamma_0 \equiv \frac{\xi_0}{(\Delta t)^2} = \sum_{j=1}^M T_j^2 \exp[-2\chi r T_j] \quad (19b)$$

In equations (18) and (19) the dimensionless parameters r , χ , and T_j are defined as

$$r \equiv \frac{\text{period}}{\text{decay time}} = \frac{2\pi\Gamma_0}{A_0} \quad , \quad \chi \equiv \frac{\text{sample time}}{\text{period}} = \frac{A_0 \Delta t}{2\pi} \quad , \quad \text{and} \quad T_j \equiv \frac{\text{delay time}}{\text{sample time}} = \frac{\tau_j}{\Delta t} \quad .$$

If the correlation function is obtained using a linear correlator, in which the delay time is an integral multiple of the sample time, ie. $\tau_j = j\Delta t$ (or $T_j = j$), then equations (19) reduce to

$$\gamma = \sum_{j=1}^M j^2 s^j \quad \text{and} \quad \gamma_0 = \sum_{j=1}^M j^2 s_0^j, \quad (20a,b)$$

where

$$s \equiv \exp[-2\chi(r - i2\pi)] \quad \text{and} \quad s_0 \equiv \exp(-2\chi r).$$

The series expressed in equations (20) are simply the second derivatives of geometric series. Therefore, both series sum to the following closed-form expressions:

$$\gamma = s \frac{1 + s - (M + 1)^2 s^M + (2M^2 + 2M - 1) s^{M+1} - M^2 s^{M+2}}{(1 - s)^3} \quad (21a)$$

and

$$\gamma_0 = s_0 \frac{1 + s_0 - (M + 1)^2 s_0^M + (2M^2 + 2M - 1) s_0^{M+1} - M^2 s_0^{M+2}}{(1 - s_0)^3}, \quad (21b)$$

which reduce to the following as the number of correlator channels M approaches infinity:

$$\gamma = \frac{s(1 + s)}{(1 - s)^3} \quad \text{and} \quad \gamma = \frac{s_0(1 + s_0)}{(1 - s_0)^3}. \quad (22a,b)$$

The above expressions, which relate the variances of the least-squares-inferred parameters A and Γ to the variance of the measured normalized correlation function, are useful for determining the estimated statistical uncertainties of A and Γ . The dimensionless variance ratios on the left sides of equations (18) are the ratios of the squares of the inferred parameters' percent uncertainties to the square of the normalized experimental correlation function's percent uncertainty (as $\tau \rightarrow 0$). These variance ratios provide guidelines for the determination of appropriate experimental parameters to produce accurate results. All subsequent results presented in this paper are obtained using the expressions for γ and γ_0 given by equations (21) and (22), which are valid only when the correlation function's measured delay times are uniformly spaced. Extension of these results to multi-tau correlation, in which the measured delay times are exponentially spaced, can be accomplished by evaluating the sums in equations (19) with appropriately spaced T_j values.

For present purposes, a maximum "acceptable" limit of uncertainty is defined to be the same percent uncertainty as the uncertainty of the initial normalized data. This limit is set in order to insure that random errors in the raw data do not produce excessive errors in the inferred results. Thus, setting the normalized variance ratios expressed above equal to unity defines the boundaries of the acceptable region of operation for the measurement system. These boundaries are shown for various numbers of correlator channels M in figures 2 and 3. All points in the plane below the curves represent acceptable operating conditions according to the stated criterion. These results are quite general for the discrete sampling of any signal with the form of equation (9). Comparison of figures 2 and 3 reveals that the curves derived from $\text{Var}(A)/(\sigma A)^2$ provide a more stringent criterion than those derived from $\text{Var}(\Gamma)/(\sigma \Gamma)^2$ over the region of interest. The more stringent criterion should be used for the determination of any recommended operating condition.

An additional constraint can be imposed upon the variance criteria by noting that accurate results are best obtained when the maximum delay time is approximately four times the exponential decay time of the correlation function [13]. For the heterodyne case, this condition reduces to $M\Gamma\Delta t = 4$ (or $M\Gamma\chi = 4$). The application of this constraint permits the determination of a single curve bounding the region where both variance ratios are less than or equal to unity. This curve, which is presented in figure 4, presents the value of r , which is denoted as $r_{\max}(M)$, that yields $\text{Var}(A)/(\sigma A)^2$ equal to unity for each value of M . For any specified number of correlator channels, any value of r less than or equal to $r_{\max}(M)$ conforms to the above-mentioned variance criteria.

The curve in figure 4 does not extend to values of M less than 52 because when M is less than 52 no value of r exists that makes both variance ratios less than or equal to unity. Thus, when the $M\Gamma\Delta t = 4$ constraint is applied the sensitivity criterion proposed in this study cannot be satisfied when less than 52 linear correlator channels are used. By relaxing the acceptance criterion a smaller number of correlator channels can be accommodated. For example, if the maximum acceptable value of the two variance ratios is increased to 2 the minimum number of linear correlator channels reduces to $M = 26$. For consistency, the maximum acceptable variance ratios are nevertheless set equal to unity throughout this paper.

For applying these results to the specific problem of determining acceptable experimental parameters for a heterodyne DLS experiment, the scattering angle corresponding to $r = r_{\max}(M)$,

$$\theta_{\max} = 2 \sin^{-1} \left(\frac{\lambda V r_{\max}(M)}{8\pi^2 n D} \right), \quad (23)$$

which occurs when $\text{Var}(A)/(\sigma A)^2 = 1$, is plotted for monodisperse, spherical, optically isotropic particles ranging in size from 30 to 90 nm and undergoing a bulk velocity from 0.1 to 3.5 cm/s at a temperature of 775 K in figure 5 and 1300 K in figure 6. This angle θ_{\max} sets an upper limit for suitable scattering angles. Equation (23) incorporates the $M\Gamma\Delta t = 4$ constraint mentioned earlier. The relevant flame parameters and primary particle sizes

used to determine the particles' diffusion properties and the graph's axis limits were taken from the experimental results of Zhang [15]. The bulk velocity range (0.1 to 3.5 cm/s) was chosen to be on the order of thermophoretic velocities calculated for the largest measured temperature gradient (≈ 228 K/mm) of a 6.35 mm diameter CO/air laminar diffusion flame at a height of 35 mm above the burner surface. Similarly, the range of particle diameters (30 to 90 nm) was chosen to encompass the size range of primary particles observed in transmission electron micrographs of iron oxide particles that were thermophoretically sampled from this flame when seeded with $\text{Fe}(\text{CO})_5$ vapor. The translational diffusion coefficient used to evaluate the information in figures 5 and 6 was evaluated from the slip-corrected Stokes-Einstein relation [1, 2]:

$$D = \frac{kT}{6\pi\mu a} C_s \quad (24)$$

where k is Boltzmann's constant, μ is the viscosity of the solvent, a is the particle diameter, and

$$C_s = 1 + \frac{\lambda}{a} \left[1.234 + 0.414 \exp\left(-0.876 \frac{a}{\lambda}\right) \right] \quad (25)$$

is the Cunningham correction factor, which corrects the original Stokes-Einstein equation for non-continuum effects when the gas mean free path λ is not negligibly small in comparison to the particle diameter a [14]. These equations indicate that the slip-corrected translational diffusion coefficient increases with increasing temperature. This causes θ_{\max} to decrease with increasing temperature. This decrease in θ_{\max} with increasing temperature is observable in comparing figures 5 and 6.

These θ_{\max} results are qualitatively consistent with resolution considerations for the heterodyne power spectrum presented by Ware and Flygare [5], who define a frequency-based resolution as the ratio of the velocity-induced Doppler frequency shift of the scattered light to the diffusion-governed half width of the scattered light spectrum:

$$R \equiv \frac{\Delta \omega_{\text{shift}}}{\Delta \omega_{1/2 \text{ width}}} \quad (26)$$

For the Lorentzian scattered light frequency spectrum from monodisperse spherical particles [5]

$$R = \frac{qV}{q^2 D} \quad (27)$$

Since this resolution must be larger than unity in order to be able to accurately infer the velocity and diffusion coefficient from the frequency spectrum, the resolution-based maximum scattering angle has the following form:

$$\theta_{\max} = 2 \sin^{-1} \left(\frac{\lambda V q}{4\pi^2 n D} \right), \quad (28)$$

which is very similar to the previously derived expression for θ_{\max} given by equation (23).

4. Application to Nonspherical Particles

The analysis presented in this paper considers the feasibility of inferring the bulk translational velocities of monodisperse spherical particles from heterodyne DLS data. Since the agglomerated particulates in flame systems are often nonspherical, some considerations of the effects of nonsphericity and anisotropy to the uncertainties of the inferred bulk velocities and Brownian diffusion coefficients are presented.

The effects of optical anisotropy (and/or nonsphericity) on $I_1(t)$ can be approximated using an anisotropic dipole model, in which, for a cylindrically symmetric scatterer, the scatterer's polarizability contains two independent components, α_{par} and α_{per} , which are respectively parallel and perpendicular to the axis of symmetry. The first order autocorrelation function $I_1(t)$ has been evaluated for such scatterers by Berne and Pecora [2] under the assumptions that a) the incident electric field intensity is uniform throughout the scattering volume, b) the position and motion of each scatterer is statistically independent of the position and motion of the other scatterers, c) the translational motion of each scatterer is statistically independent of its rotational motion and vice versa, d) all scatterers within the scattering volume have identical optical and dynamic properties, e) statistical fluctuations of the number of scatterers in the scattering volume are negligible, and f) the length of each scatterer is much smaller than the wavelength of the incident light and thus validates the use of the dipole model instead of a general multipole expansion. The resulting expressions for $I_1(t)$ for VV and VH detection are [2]:

$$I_{\text{VV}}^{(1)} = \left\langle N_p \right\rangle \left[|\alpha|^2 + \frac{4}{45} \beta^2 \exp(-6D_R \tau) \right] \exp(-q^2 D \tau) \exp(iq \cdot V \tau) \exp(-i\omega_L \tau) \quad (29)$$

and

$$I_{\text{VH}}^{(1)} = \frac{1}{15} \left\langle N_p \right\rangle |\beta|^2 \exp[-(q^2 D + 6D_R) \tau] \exp(iq \cdot V \tau) \exp(-i\omega_L \tau) \quad (30)$$

where $\left\langle N_p \right\rangle$ is the average number of scatterers in the scattering volume, $\alpha \equiv (\alpha_{\text{par}} + 2\alpha_{\text{per}})/3$ is the isotropic part of the polarizability tensor, $\beta \equiv \alpha_{\text{par}} - \alpha_{\text{per}}$ is the optical anisotropy of the scatterers, and D_R is the scatterers' Brownian rotational diffusion coefficient. The $\exp(iq \cdot V \tau)$ term has been added to the original equations given by Berne and Pecora to account for the effects of bulk flow. Likewise, the incident light angular frequency term $\exp(-i\omega_L \tau)$, which was neglected by Berne and Pecora, is also included here for compatibility with the other equations.

Substitution of equations (29) and (30) into equations (4) and (6) yields (for $\omega_{\text{LO}} = \omega_L$)

$$\langle\langle n(0)n(\tau) \rangle\rangle_{VV,het} = \langle n(0) \rangle^2 \left\{ 1 + \frac{2\epsilon^2 \langle N_p \rangle}{N_c I_{LO}} \left[|\alpha|^2 + \frac{4}{45} |\beta|^2 \exp(-6D_R\tau) \right] \right\} \cos(qV\tau) \exp(-q^2 D\tau) + \langle n(0) \rangle u(\tau) \quad (31)$$

and

$$\langle\langle n(0)n(\tau) \rangle\rangle_{VH,het} = \langle n(0) \rangle^2 \left[1 + \frac{2\epsilon^2 \langle N_p \rangle |\beta|^2}{15N_c I_{LO}} \right] \cos(qV\tau) \exp[-(q^2 D + 6D_R)\tau] + \langle n(0) \rangle u(\tau). \quad (32)$$

Since the VV correlation function for cylindrically symmetric particles contains two exponentials, the variance results of equations (18) are not directly applicable to this case. Equation (31) demonstrates that assuming a single-exponential form for the VV correlation function from cylindrically-symmetric, nonspherical particles introduces a systematic error in the data interpretation. The percent deviation of the true normalized VV correlation function, as determined through normalization of equation (31), from the spherical-particle (single-exponential) normalized correlation function, as given by equation (9), is thus

$$\% \text{ Error} = \frac{F}{1 + F} \times 100\%, \quad (33)$$

where

$$F = \frac{4}{45} \left| \frac{\beta}{\alpha} \right|^2 \exp(-6D_R\tau) = \frac{4}{45} \left| \frac{\beta}{\alpha} \right|^2 \exp \left[-24 \frac{D_R}{q^2 D} \left(\frac{\tau}{T} \right) \right]$$

and T ($\equiv M\Delta t = 4/(q^2 D)$) is the correlation function's maximum measured delay time. This formula indicates that the approximation of the normalized VV heterodyne correlation function as a single exponential function is valid when $(4|\beta|^2)/(45|\alpha|^2)$ is much less than unity and/or $(24D_R)/(q^2 D)$ is much greater than unity. Typical values of $(4|\beta|^2)/(45|\alpha|^2)$ for prolate ellipsoidal particles of refractive index $m = 1.64 - 0.3i$, which corresponds to Fe_2O_3 at room temperature [16], are plotted in figure 7 for aspect ratios ranging from 2 to 20. These curves were computed using the electrostatics approximations for the polarizability components of prolate ellipsoids, as presented by van de Hulst [17]. In this case, the maximum value of $(4|\beta|^2)/(45|\alpha|^2)$, which is obtained as the aspect ratio approaches

infinity, is 0.048. This limits the maximum deviation between the single and double exponential forms of the normalized VV correlation function to 4.6% for particles of refractive index $m = 1.64 - 0.3i$ at wavelength $\lambda = 488$ nm. Under the conditions in which the approximation of the VV heterodyne correlation function as a single-exponential function is deemed acceptably accurate, the variance analysis presented for spherical particles applies to cylindrically symmetric particles without modification.

Alternatively, the VH heterodyne correlation function is a single exponential function that has the same general form as the VV heterodyne correlation function for spherical particles, with the difference being the constant factors and the exponential decay rate. The same general analysis for θ_{\max} that was performed for the spherical particles thus applies for this case, provided that Γ is replaced with $(q^2D + 6DR)$. Therefore, when the constraint $M\Gamma\Delta t = 4$ is used, the range of scattering angles that facilitate the inference of A and Γ ($\equiv q^2D + 6DR$) with variance ratios less than or equal to unity is found from the expression:

$$r = \frac{2\pi\Gamma}{A} = \frac{2\pi(q^2D + 6DR)}{q \cdot V} \leq r_{\max}(M). \quad (34)$$

The introduction of the θ -independent quantity $6DR$ in the numerator of equation (34) causes this criterion to be quadratic in q . As a result, accuracy is not necessarily improved by running the experiment at arbitrarily low scattering angles. When $[V_{q\max}(M)]^2/(96\pi DD_R) > 1$, where V_q is the component of V in the direction of q , two scattering angles

$$\theta_{\min} = 2 \sin^{-1} \left\{ \frac{\lambda}{16\pi^2 n} \frac{V_{q\max}(M) - [(V_{q\max}(M))^2 - 96\pi^2 DD_R]^{1/2}}{D} \right\} \quad (35)$$

and

$$\theta_{\max} = 2 \sin^{-1} \left\{ \frac{\lambda}{16\pi^2 n} \frac{V_{q\max}(M) + [(V_{q\max}(M))^2 - 96\pi^2 DD_R]^{1/2}}{D} \right\} \quad (36)$$

bound the range of scattering angles for which equation (34) is satisfied. When $[V_{q\max}(M)]^2/(96\pi DD_R) = 1$ equation (34) is only satisfied at the scattering angle

$$\theta = 2 \sin^{-1} \left[\frac{\lambda}{16\pi^2 n} \frac{V_{q\max}(M)}{D} \right]. \quad (37)$$

When $[V_{Q\max}(M)]^2/(96\pi D D_R) < 1$ no solution exists for equation (34) and the variance ratio criterion cannot be satisfied. The boundaries of the range of acceptable scattering angles are depicted for straight chain agglomerates suspended in a gaseous medium at a temperature of 775 K in figure 8 and at a temperature of 1300 K in figure 9. The translational and rotational diffusion coefficients used to calculate the scattering angle ranges depicted in figures 8 and 9 were determined through the use of Perrin's equations for prolate ellipsoidal particles of semiaxes $a > b = c$ [4, 18, 19]:

$$D = \frac{kT}{6\pi\mu R_{eq}} \rho^{2/3} G(\rho) \quad (38)$$

and

$$D_R = \frac{3kT}{16\pi\mu R_{eq}^3} \frac{\rho^2[(2 - \rho^2)G(\rho) - 1]}{1 - \rho^4}, \quad (39)$$

where

$$\rho \equiv \frac{b}{a},$$

$$G(\rho) \equiv \frac{1}{\sqrt{1 - \rho^2}} \ln \left[\frac{1 + \sqrt{1 - \rho^2}}{\rho} \right],$$

and R_{eq} is the particle's volume-equivalent sphere radius. The above expression for D_R is valid for tumbling about the ellipsoidal particle's short axis b . Assuming that the particle's material composition is optically isotropic, spinning about the long axis a does not affect the scattered light correlation function. To account for non-continuum and slip-flow effects, the expression for D is multiplied by the Cunningham correction factor of equation (25) (replacing a with R_{eq}). In the absence of an adequate non-continuum correction factor for the rotational diffusion coefficient D_R , non-continuum slip flow is assumed to affect the rotational diffusion coefficient D_R in a manner similar to its effect on the translational diffusion coefficient D . Therefore, as in reference [1], Perrin's equation for the rotational diffusion coefficient D_R is corrected for non-continuum and slip flow effects using the same Cunningham correction factor C_s used to correct the translational diffusion coefficient D .

Like the translational diffusion coefficient D for spherical particles, both the translational and rotational diffusion coefficients increase with increasing temperature. As a result, the range of scattering angles conforming to the variance criteria decreases with increasing temperature. This effect is observable in comparing figure 9 to figure 8, where, for example, increasing the temperature from 775 K to 1300 K decreases the range of acceptable scattering angles by 36% for chainlike agglomerates of aspect ratio 8 undergoing a bulk velocity of 83 cm/s.

As a result of the sensitivity considerations of this section, VV heterodyne detection appears to be better suited than VH detection for measuring the bulk velocities of cylindrical agglomerates under the high temperature conditions considered here when the bulk velocities are less than approximately 30 cm/s. For VV detection of spherical and/or cylindrical particles, the variance ratios of equations (18) can theoretically be reduced to less than unity at any bulk velocity by reducing the scattering angle θ of the detector optics. The variance ratios from the VH heterodyne correlation function, however, does not exhibit this behavior because of the presence of the θ -independent rotational diffusion term in equation (29). For VH heterodyne experiments the variance ratios are both less than unity only within the limited range of conditions defined by equation (31). This fact makes the application of VV detection to velocity measurements more generally applicable than VH detection.

5. Discussion

The expressions developed relating the variances of the parameters A and Γ of a heterodyne correlation function to the variance of the normalized raw data is applicable to any discretely sampled exponentially decaying cosine function, provided that the decaying amplitude conforms to a single exponential function. The strict validity of these variance equations relies on the assumption that the deviations of the experimental data from the theoretical form of $g(\tau)$ occur only as uncorrelated random errors. Thus, systematic errors are not considered in this analysis. In applying these results to the interpretation of heterodyne photon correlation data from monodisperse spherical particles, restriction of the variance ratios of equations (18) to unity or less insures that the percent uncertainties of the inferred frequency A ($\equiv q \cdot V$) and decay Γ ($\equiv q^2 D$) terms are no greater than the percent uncertainty (extrapolated to $\tau = 0$) of the normalized raw data. This analysis demonstrates that for accurate data inversion the ratio r of the correlation function's period to its decay time should be less than a constant whose magnitude is typically on the order of magnitude of 10. At larger values of this ratio the correlation function decays to its baseline value before it can complete enough of an oscillation to contain enough information for accurate frequency inference.

These variance results can be used to estimate the uncertainties of V_q and D through the relationships (see [20]):

$$\text{Var}(V_q) \equiv \left(\frac{\partial V_q}{\partial A} \right)^2 \text{Var}(A) + \left(\frac{\partial V_q}{\partial q} \right)^2 \text{Var}(q) = \frac{\text{Var}(A)}{q^2} + \left(\frac{A}{q^2} \right)^2 \text{Var}(q) \quad (40)$$

and

$$\text{Var}(D) \equiv \left(\frac{\partial D}{\partial \Gamma} \right)^2 \text{Var}(\Gamma) + \left(\frac{\partial D}{\partial q} \right)^2 \text{Var}(q) = \frac{\text{Var}(\Gamma)}{q^4} + \left(\frac{2\Gamma}{q^3} \right)^2 \text{Var}(q). \quad (41)$$

The statistical uncertainties of V_q and D are, by definition, the square roots of their variances. The variances of A and Γ required for evaluating equations (40) and (41) are readily obtained from equations (18). The variance of q , which increases with decreasing scattering angle, is determined by both the angular resolution of the goniometer used to set the scattering angle and the size of the scattering volume [7].

As previously discussed, the variance expressions presented in this paper can also be applied to cylindrically symmetric particles. Since, unlike the VH heterodyne correlation function, the VV correlation function from monodisperse cylindrical particles contains a multi-exponential decay factor, equations (18) are not strictly applicable since the approximation of the correlation function as a single-exponential function introduces a systematic error in the data analysis. The correlation function does, however, often follow the single-exponential form very closely

under the conditions presented in the previous section. One possible extension of the present analysis would be to determine how this systematic error affects the variance estimates of the inferred parameters.

The functional form of the correlation function also deviates from the single-exponential form of equation (9) when the scattering particles are polydisperse, thus exhibiting variations in the particle dimensions and/or optical properties. Like the case of VV heterodyne detection from monodisperse, nonspherical scatterers, this deviation produces a systematic error in the data analysis if a single-exponential decay is assumed. The theoretical correlation function of light scattered from a suspension of polydisperse scatterers is generally expressed as a weighted integral of the monodisperse correlation function over the entire range of particle dimensions and/or optical properties. In order to properly evaluate the effects of polydispersity on the statistical uncertainty of the inferred results, an inversion scheme that accounts for this polydispersity must first be developed for the heterodyne case. Then, a variance analysis could be performed using the same general methodology as the analysis presented in this paper.

One further limitation of this analysis is the assumption that the pre-exponential factor of equation (8), (31), or (32) is known prior to the inversion of the raw data so that the data can be properly normalized. This factor can be determined by extrapolating the correlation function to its zero-delay-time value. If the current formulation is used to estimate the variances of A and Γ from the variances of the correlation function data, the variance of the normalized correlation function must first be adjusted to account for the uncertainty of this pre-exponential factor. An alternative technique would be to treat the pre-exponential factor as a third unknown parameter in the least-squares data inversion scheme and extending the current variance analysis using a derivation similar to the one presented in this paper.

6. Summary of Results

The results of the present study may be summarized as follows:

- a) As the particle size and bulk velocity increases, the maximum acceptable scattering angle for accurate determination of the bulk velocity and Brownian diffusion coefficient increases. This occurs because increasing the size or bulk velocity increases the decay time of the correlation function with respect to its period, thus permitting more measurable oscillations of the cosine factor before the correlation function completely decays to its baseline value.
- b) On the basis of the variance analysis for monodisperse spherical particles, the inference of $A (\equiv qV)$ and $\Gamma (\equiv q^2D)$ with a percent uncertainty less than or equal to the initial percent uncertainty of the normalized correlation function data may be performed for the CO/air diffusion flame under consideration when the average particle velocity is greater than approximately 1 cm/s and the diameter of the particles is larger than approximately 40 nm. The translational diffusion coefficient D and the q -component of the average velocity V_q may then be found through knowledge of q from equation (2).
- c) Under certain conditions, this analysis can be extended to non-spherical particles. For VV detection of monodisperse cylindrically symmetric particles, the heterodyne correlation function contains two distinct exponential terms, making the single-exponential-based variance analysis considered in this paper invalid. When the scattering particles' polarizability anisotropy is much smaller than the isotropic part of the polarizability tensor and/or the rotational relaxation time is much smaller than the translational relaxation time, the VV correlation function may be approximated as a single-exponential function. In this case, the variance analysis presented in this paper applies to non-spherical particles without modification. The variance analysis also applies to the single-exponential VH correlation function from cylindrically symmetric, anisotropic particles. In this case, however, the addition of a scattering-angle-independent rotational diffusion term to the exponential decay factor changes the qualitative characteristics of the range of scattering angles giving acceptable error propagation characteristics. For particles of aspect ratio less than approximately ten the magnitudes of the minimum measurable bulk velocities are considerably larger (by a factor of 10 to 100) than the velocities measurable using VV detection. As revealed in figure 8 the minimum measurable bulk velocity gradually decreases as the aspect ratio of the scatterers increases. This occurrence of a distinct minimum measurable bulk velocity severely limits the applicability of VH heterodyne detection to measuring bulk velocities.

7. References

1. Charalampopoulos, T. T. *Prog. Energy Combust. Sci.* 18: 13-45 (1992).
2. Berne, B. J., and Pecora, R. *Dynamic Light Scattering* Wiley, New York, 1976.
3. Benedek, G. B. in *Polarization, Matter, and Radiation*, Presses Universitaires de France, Paris, 1969, pp. 49 - 84.
4. Russo, P. S., Saunders, M. J., DeLong, L. M., Kuehl, S., Langley, K. H., and Detenbeck, R. W. *Analyt. Chim. Acta* 189: 69-87 (1986)
5. Ware, B. R. and Flygare, W. H. *Chem. Phys. Lett.* 12: 81-85 (1971)
6. Cummins, H. Z., and Swinney, H. L. *Progress in Optics* 8: 133-200 (1970)
7. Ford, N. C. Jr. in *Dynamic Light Scattering: Applications of Photon Correlation Spectroscopy* (R. Pecora, Ed.), Plenum Press, New York, 1985.
8. Brookhaven Instruments Corporation. *Instruction Manual for Model BI-9000-AT Digital Correlator* (1993)
9. Jakeman, E. *J. Phys. A: Gen. Phys.* 3: 201-215 (1970)
10. Waguespack, G. PhD studies (in progress). ME Department, Louisiana State University.
11. Mandel, L. *J. Opt. Soc. Am.* 56: 1200-1206 (1966)
12. Penner, S. S., Bernard, J. M., and Jerskey, T. *Acta Astronautica* 3: 69-91 (1976)
13. Jakeman, E., Pike, E. R., and Swain, S. *J. Phys. A: Gen. Phys.* 4: 517-534 (1971)
14. Dahneke, B. E. *Aerosol Science* 4: 163-170 (1973)
15. Zhang, Z. MS Thesis. ME Department, Louisiana State University, 1995.
16. Hahn, D. W., and Charalampopoulos, T. T. *Twenty Fourth Symp. (Intl.) on Combustion*. The Combustion Institute, Pittsburgh, 1992, pp. 1007 - 1014.
17. van de Hulst, H. C. *Light Scattering by Small Particles*. Dover Publications, Inc., New York, 1981.
18. Perrin, F. *J. Phys. Radium* 5: 497-511 (1934)
19. Cantor, C. R., and Schimmel, P. R. *Biophysical Chemistry*. W. H. Freeman, San Francisco, CA, 1980.
20. Beckwith, T. G., Buck, N. L., Marangoni, R. D. *Mechanical Measurements* (3rd edition) Addison-Wesley, Reading, MA, 1982.

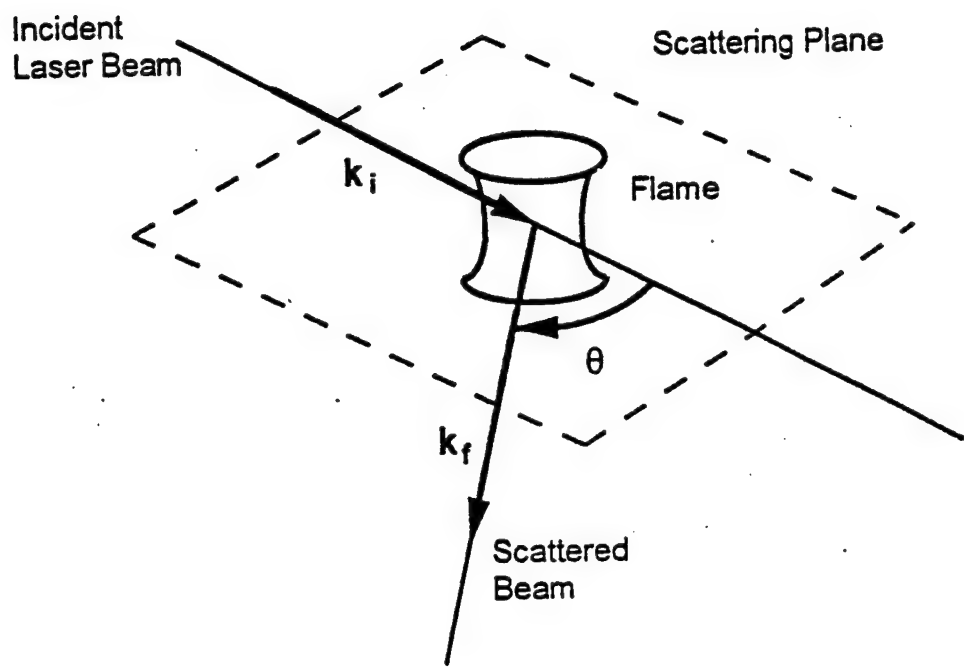


Figure 1: Scattering geometry for the dynamic light scattering (DLS) experiment.

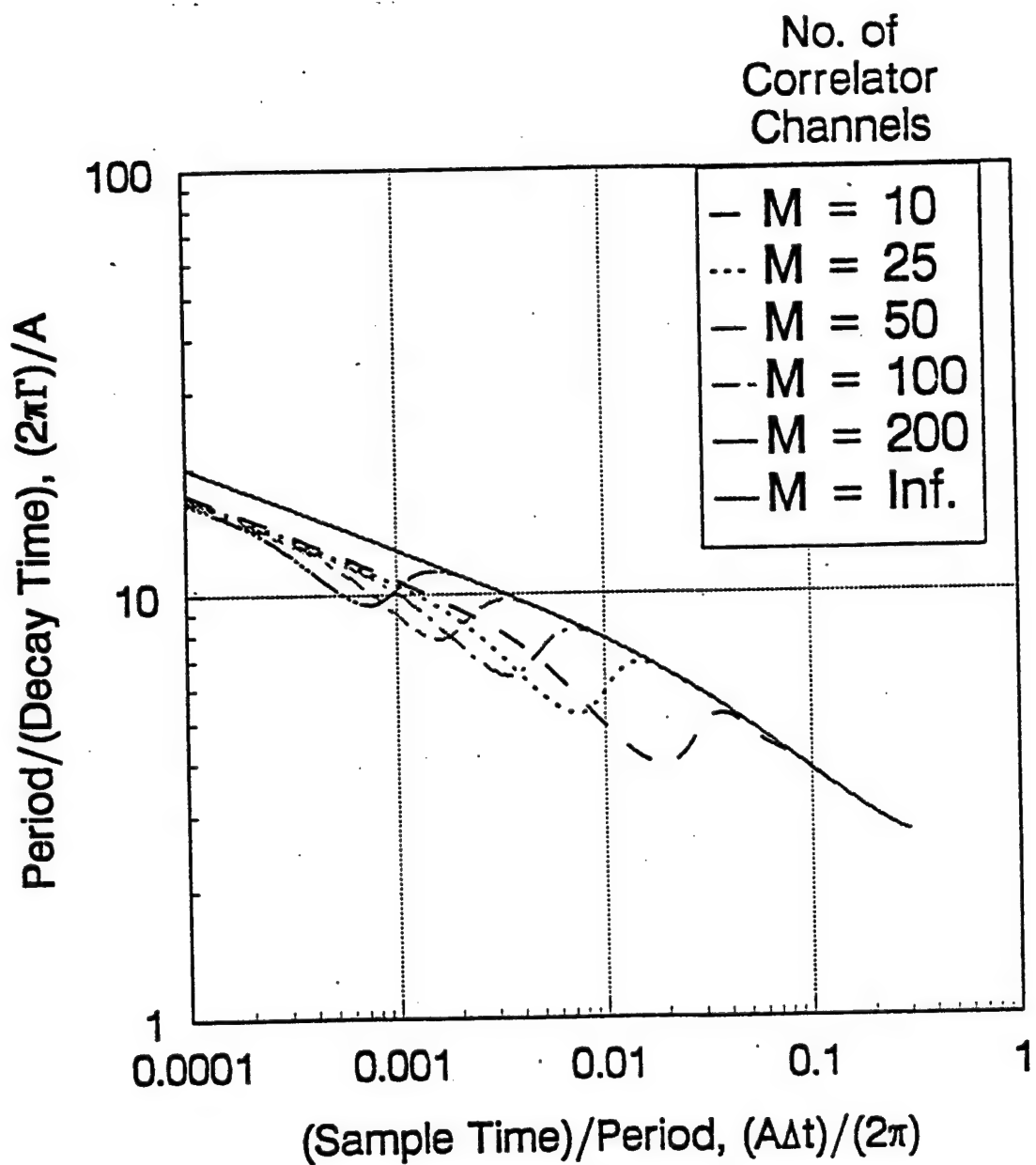


Figure 2: Boundaries of the acceptable operation region, corresponding to $\text{Var}(A)/(\sigma A)^2 = 1$, for the inference of A ($= q \cdot V$) from a single-exponential heterodyne DLS correlation function determined for M linear correlator channels. The system should operate below these curves.

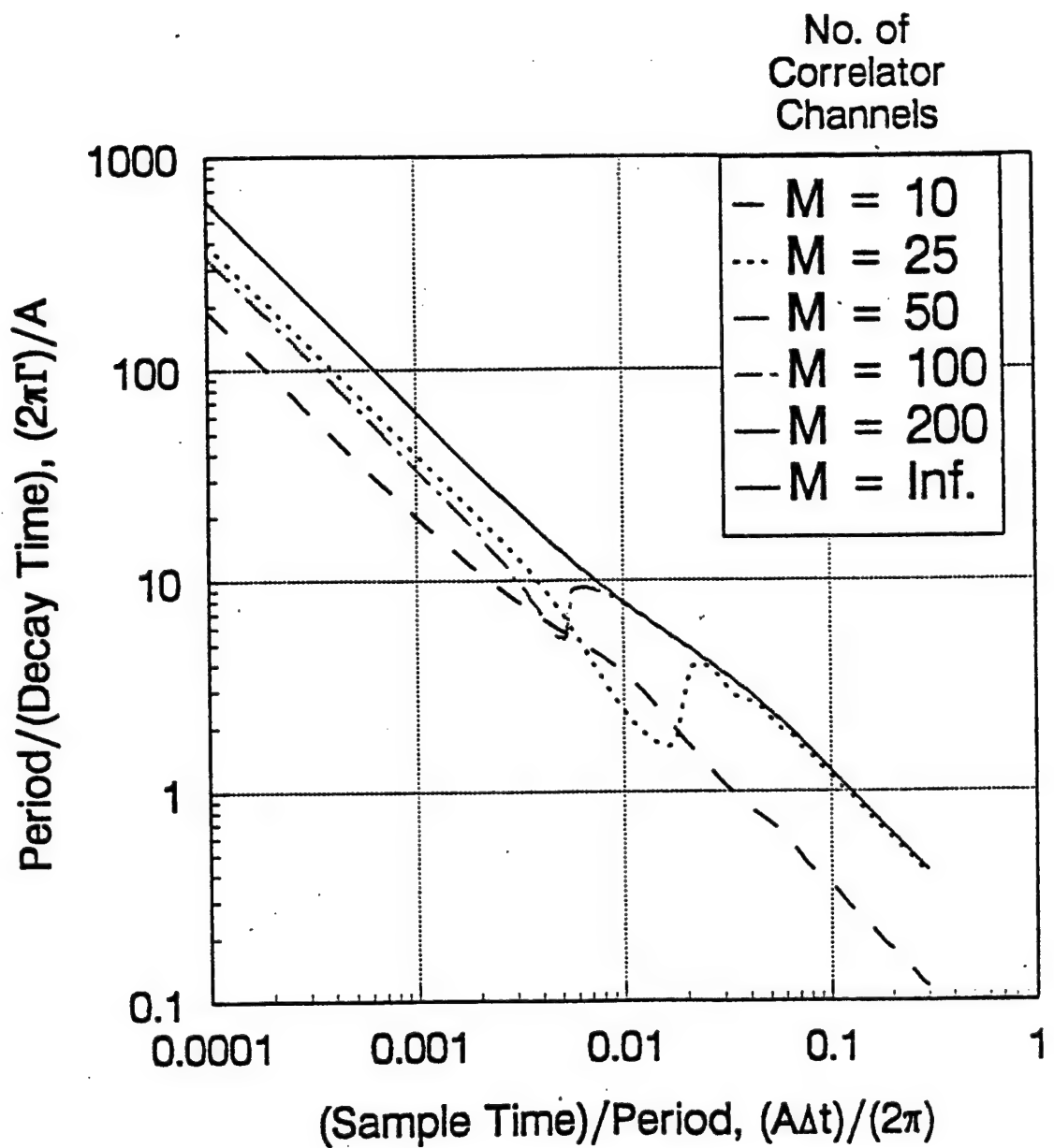


Figure 3: Boundaries of the acceptable operation region, corresponding to $\text{Var}(\Gamma)/(\sigma\Gamma)^2 = 1$, for the inference of Γ ($= q^2 D$) from a single-exponential heterodyne DLS correlation function determined for M linear correlator channels. The system should operate below these curves.

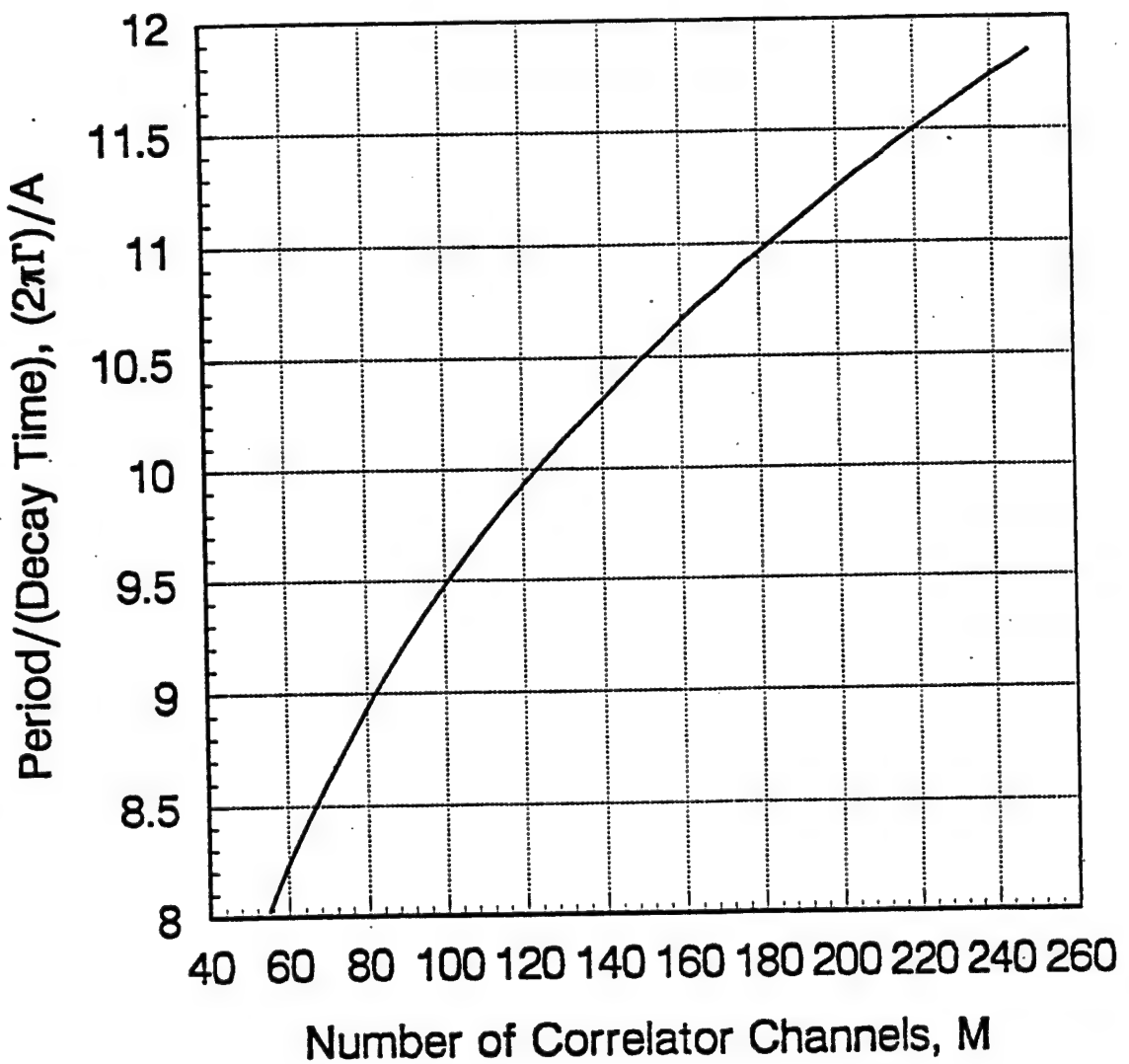


Figure 4: Maximum period/(decay time) ($r_{\max}(M)$) yielding $\text{Var}(A)/(\sigma A)^2 \leq 1$ and $\text{Var}(\Gamma)/(\sigma \Gamma)^2 \leq 1$, subject to the constraint that $M\Gamma\Delta t = 4$.

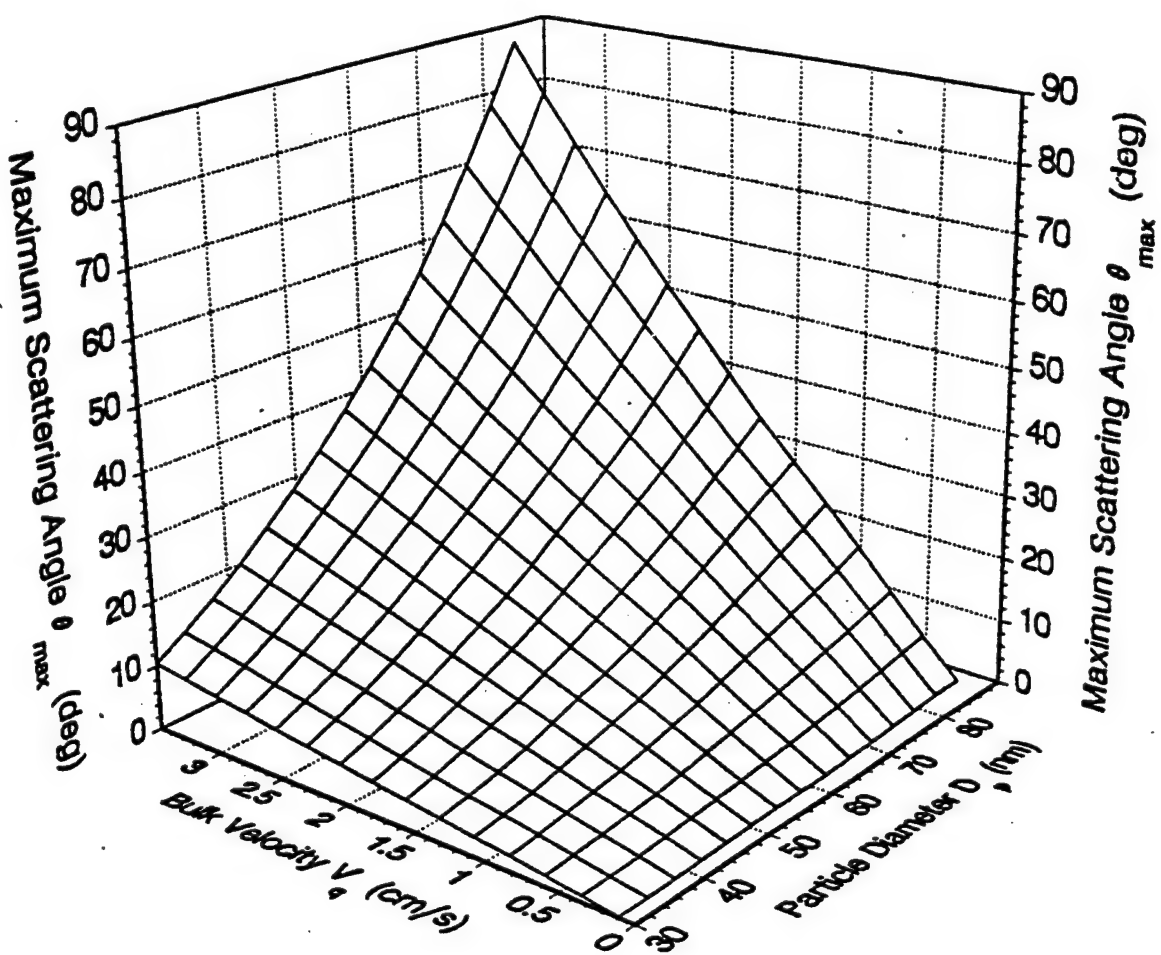


Figure 5: Maximum scattering angle for accurate inversion of A ($= q \cdot V$) and Γ ($= q^2 D$) from VV heterodyne correlation data. ($M = 200$, $\lambda = 488$ nm, Temperature = 775 K)

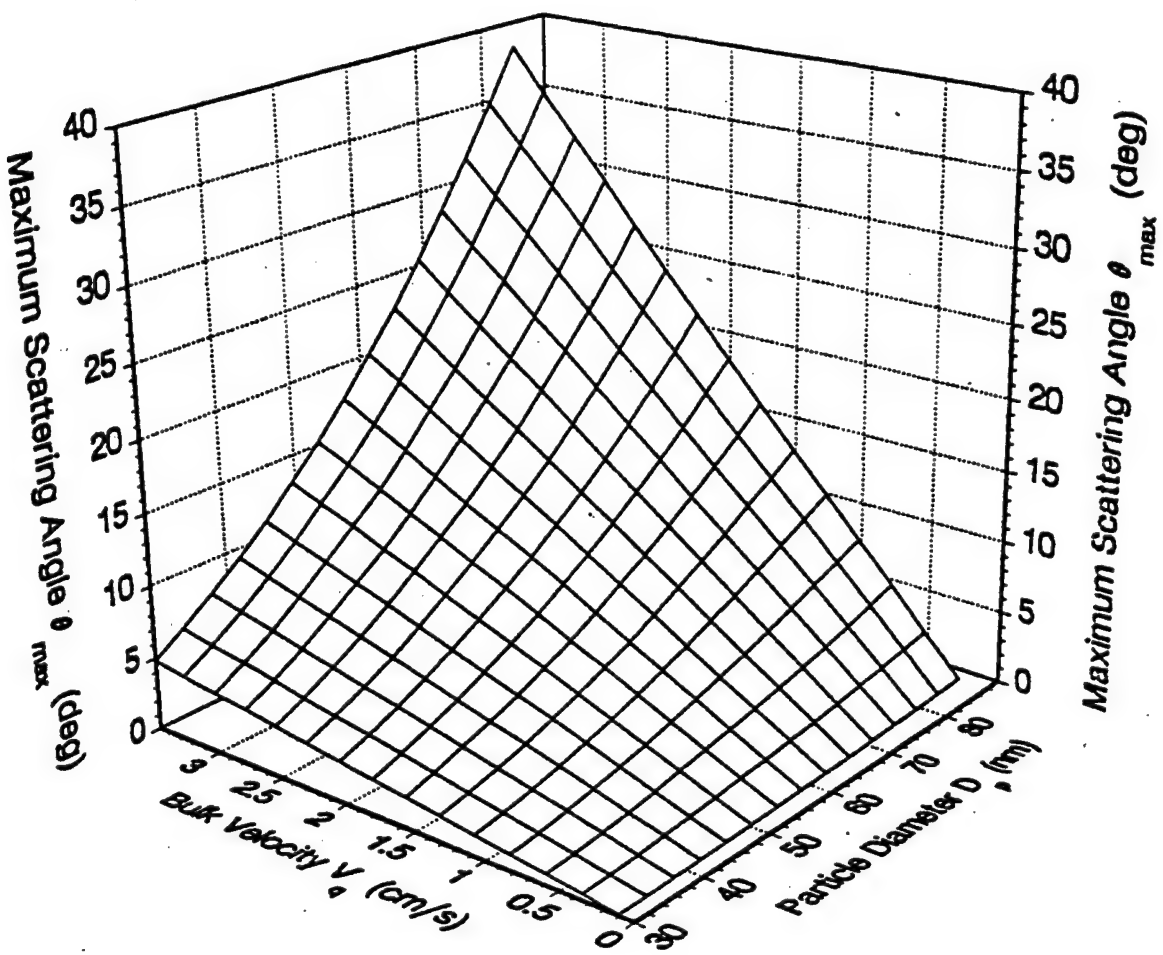


Figure 6: Maximum scattering angle for accurate inversion of A ($= q \cdot V$) and Γ ($= q^2 D$) from VV heterodyne correlation data. ($M = 200$, $\lambda = 488$ nm, Temperature = 1300 K)

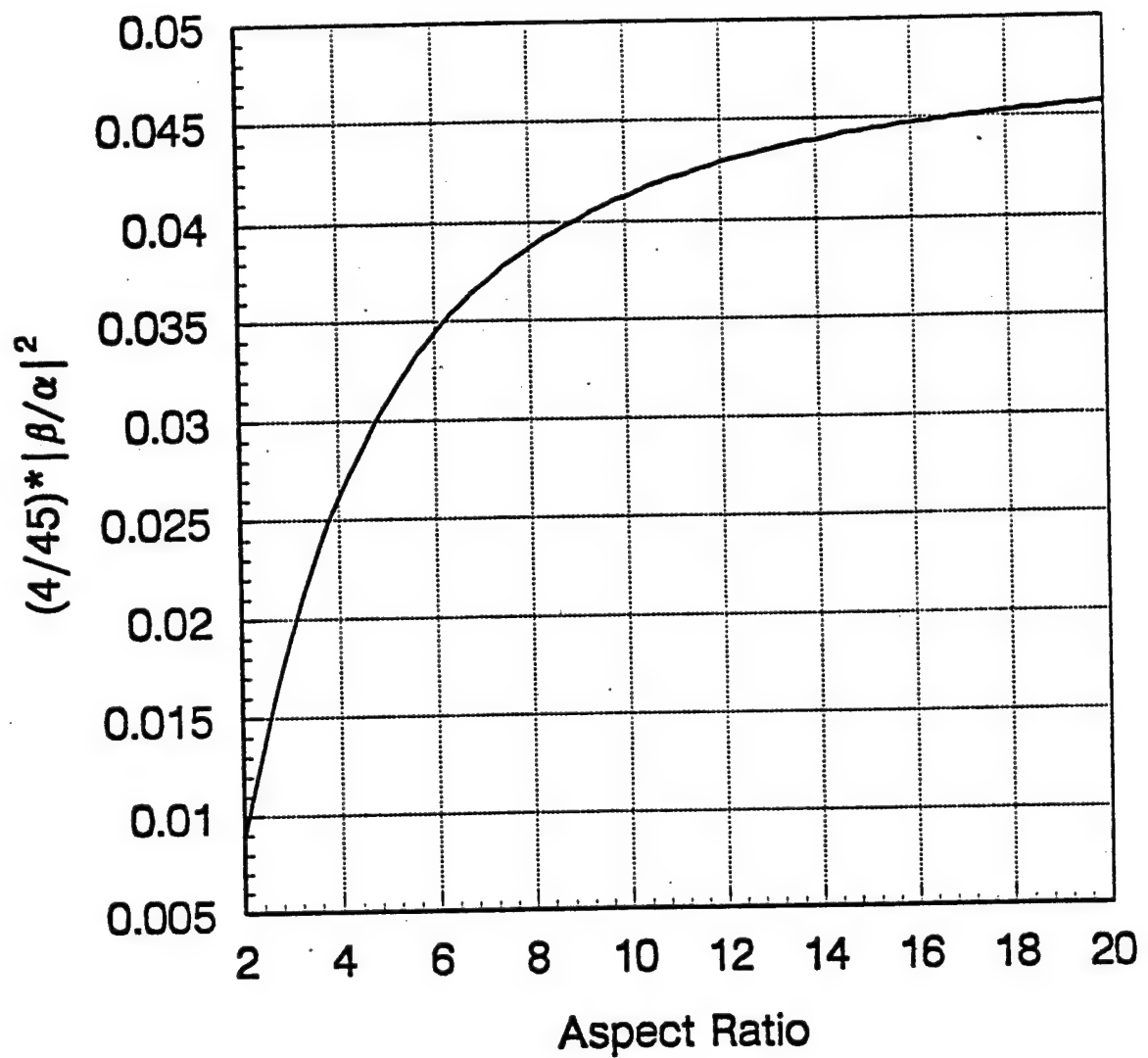


Figure 7: Relative optical anisotropy parameter $(4|\beta|^2)/(45|\alpha|^2)$ of prolate ellipsoidal particles of refractive index $m = 1.64 - 0.3i$ (corresponding to room temperature Fe_2O_3) as a function of aspect ratio.

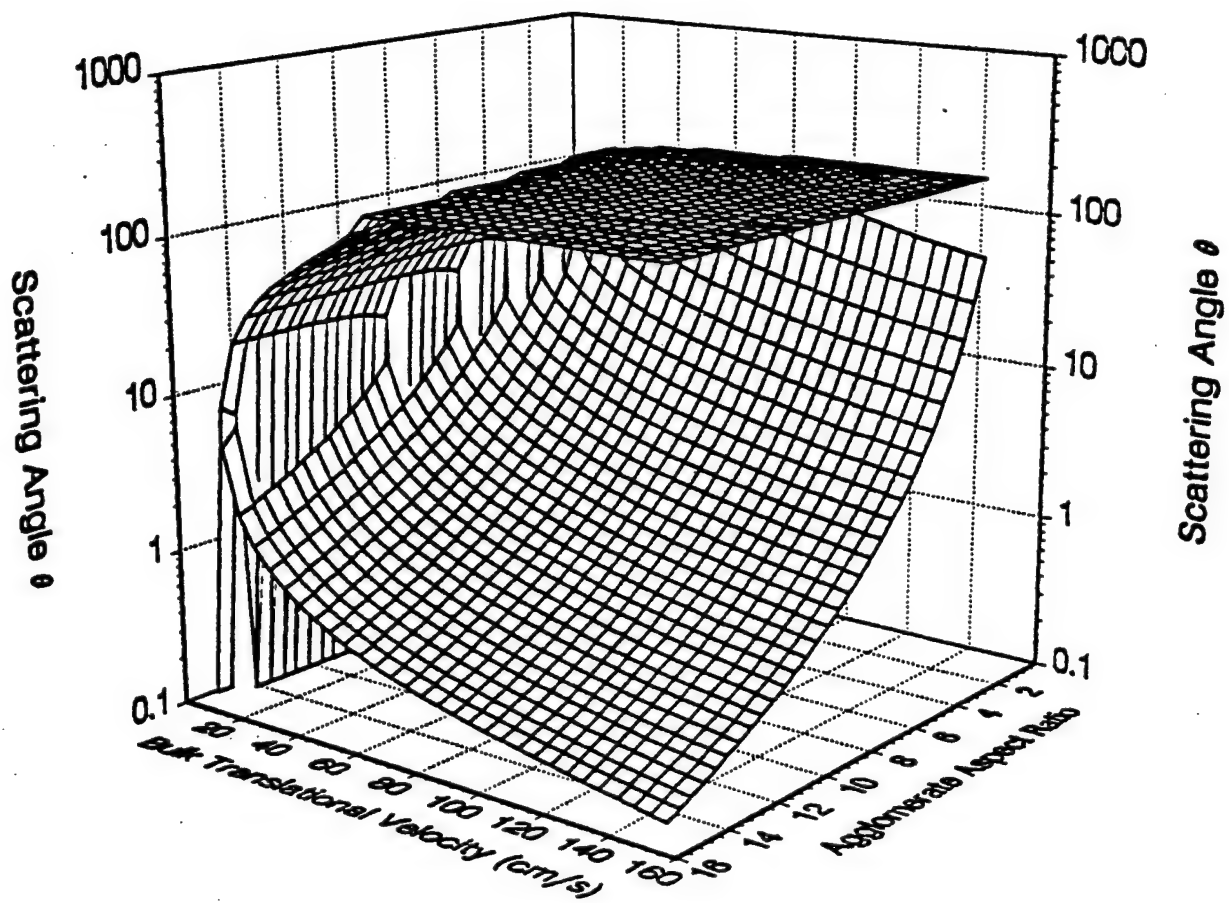


Figure 8: Upper and lower bounding surfaces of the scattering angle range for the accurate inference of A ($= q \cdot V$) and Γ ($= q^2 D + 6D_R$) from VH heterodyne correlation data. ($M = 60$, $\lambda = 488$ nm, Primary Particle Diameter = 56 nm, Temperature = 775 K)

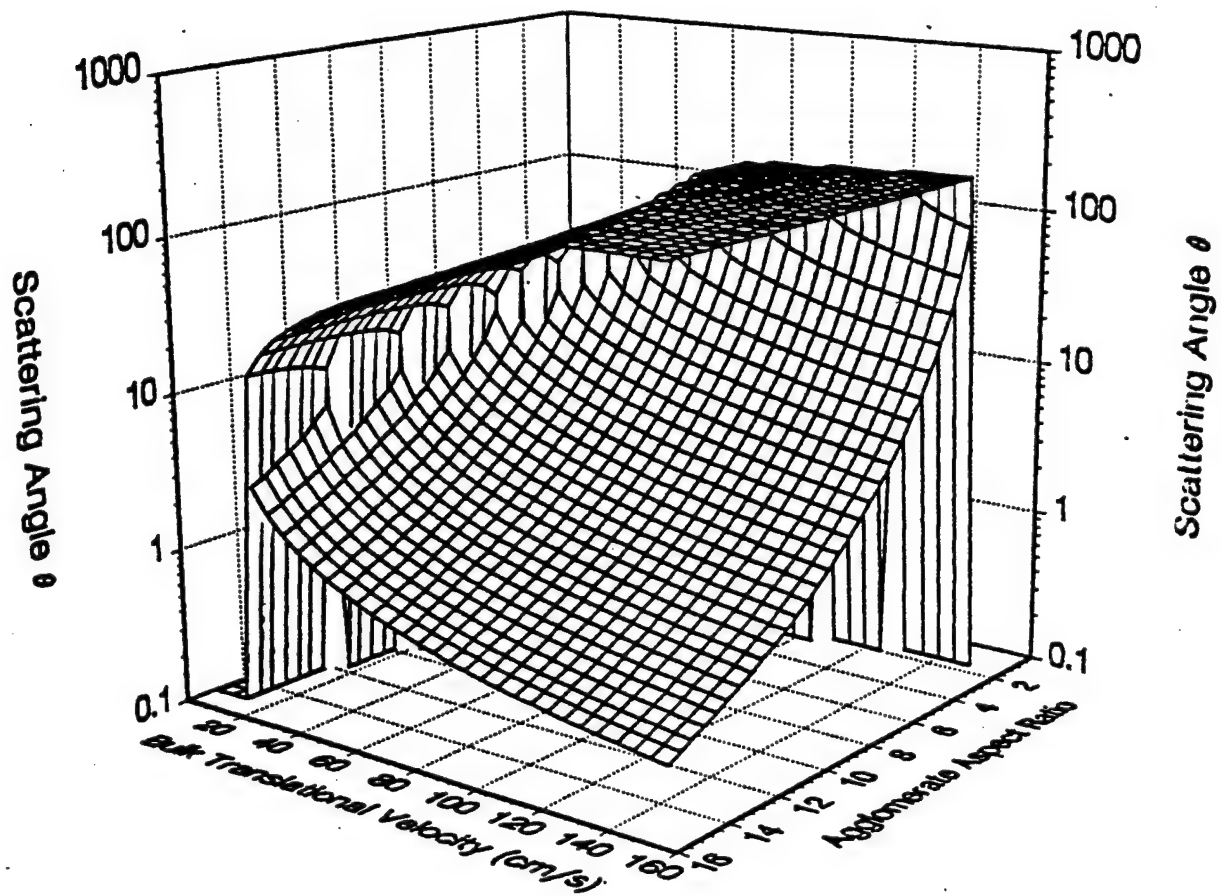


Figure 9: Upper and lower bounding surfaces of the scattering angle range for the accurate inference of A ($= q \cdot V$) and Γ ($= q^2 D + 6D_R$) from VH heterodyne correlation data. ($M = 60$, $\lambda = 488$ nm, Primary Particle Diameter = 56 nm, Temperature = 1300 K)

VII. Computer Source Code (AGGL) Developed for the Prediction of the Light Scattering Properties of Agglomerated Particulates Composed of Rayleigh Sized Primary Particles.

The FORTRAN codes included here evolved from the Exact Formulation for the light scattering properties of agglomerated particulates. The exact formulation as noted in section I of this Report has been published in the Journal of Physics D: Applied Physics Vol. 27, pp 2258 - 2270(1994). A Guide about the running of this code and an output example are provided in section VI of this Report. More information about this code may be found in the Masters Thesis of Wujiang Lou entitled "Theory and Application of Electromagnetic Wave Scattering and Absorption of Agglomerated Small Spherical Particles". This document is available in the Louisiana State University Library.

```
c*****
c.a. sub: a collection of all subroutines          'em
c.a.                                              'em
c***** prepared by w. lou, december 1994          *****
c— version: d— featuring derivatives of scattering quantities *****
c*****
c2345678901234567890123456789012345678901234567890123456789

c_____
c—sub: aggl_shell
c— a pilot program providing interface to master program
c_____lou,august 10,1994
subroutine aggl_shell(np,ns,nps,alpha,rfindx)
parameter ( mnp=100,nd=181)
complex rindx,epsilon
character eff*1,pol*1,chain*1
real kvve(nd), khhe(nd),kvhe(nd),khve(nd),
$ qetn,qetk,dkvvn(nd),dkvvk(nd),dkhvn(nd),dkhvk(nd),
$ qehtn,qehtk,dkhhn(nd),dkhhk(nd),dkvhvn(nd),dkvhk(nd),
$ qetx,qehtx,dkvvx(nd),dkhvnx(nd),dkvhx(nd),dkhhx(nd)
common/p2/pol,eff,chain
common/j2s/scahh(181),scavv(181), scahv(181), scavh(181),
$ cosang(181),sinang(181)
```

```

common/l1/xo(mnp),yo(mnp),zo(mnp)
common/lou/lu,lu1,lu2,lu3,lu4
common/lou1/cospsi(10),sinpsi(10),coschi(10),sinchi(10),w(10)
common/orient/dchi,dpsi
common/qqext/qext0,qabs0,qsca0,qexth0,qabsh0,qscah0
common/loa/qetn0,qetk0,dkvvn0(nd),dkvvk0(nd),dkhvn0(nd),
$ dk hvk0(nd),qehtn0,qehtk0,dkhhn0(nd),dkhhk0(nd),
$ dkvhn0(nd),dkvhk0(nd)
common/lox/qetx0,dkvvx0(nd),dkhv0(nd),
& qehtx0,dkhhx0(nd),dkvhx0(nd)

c---averaged derivatives for random structures/pass to master

common/qextm/qext,qabs,qsca,qexth,qabsh,qscah
common/j2sm/scahhk(181),scavvk(181), scahv(181), scavhk(181),
$ angk(181)
common/louv/rvv(nd),drvvn(nd),drvvk(nd),dkhven(nd),dkhvek(nd),
$ kvve,dkvven(nd),dkvvek(nd),rvv(nd),drvvn(nd),
$ drhv(181),khve,kvhe
common/louh/rhh(nd),drhhn(nd),drhhk(nd),dkvhen(nd),dkvhek(nd),
$ khhe,dkhhen(nd),dkhhek(nd),rvh(nd),drvhn(nd),drvhk(nd)
common/loux/qetx,drvvx(nd),drhv(181),drvhx(nd),drhhx(nd),
$ qehtx,dkvvex(nd),dkhvex(nd),dkvhex(nd),dkhhex(nd)

if(chain.eq.'r')then
else
  nps=1
end if
pi=3.1415926
epsilon=rindx*rindx

```

c---data initialization-----

```

call lou1
sumxl=0.0
qsca=0.0
qext=0.0
qabs=0.0

```

```
qscah=0.0
qexth=0.0
qabsh=0.0
do 96 i=1, ns
  scavvk(i)=0.0
  scahhk(i)=0.0
  scavhk(i)=0.0
  scahvk(i)=0.0
  angle=angk(i)*pi/180.0
  cosang(i)=cos(angle)
  sinang(i)=sin(angle)
```

96 continue

```
qetn=0.0
qetk=0.0
qehtn=0.0
qehtk=0.0
qetx=0.0
qehtx=0.0
```

do 97 i=1,ns

```
dkvvn(i)=0.0
dkvvk(i)=0.0
dkhvn(i)=0.0
dkhvk(i)=0.0
dkhhn(i)=0.0
dkhhk(i)=0.0
dkvhn(i)=0.0
dkvhk(i)=0.0
dkvvx(i)=0.0
dkhvrx(i)=0.0
dkvhx(i)=0.0
dkhhx(i)=0.0
```

97 continue

```
do 100 kk=1, nps
  if (chain .eq. 'r') then
    call random(np)
```

```

else if (chain .eq. 's') then
  call strait(np)
else if (chain .eq. 'c') then
  call clustr(np)
else
  print *, 'no such choice of chain'
  stop
endif

if(lu3.eq.0)then
  if(lu4.eq.0)then
    call agglou0(np,alpha,epsilon,ns)
  else
    call agglou0d(np,alpha,rindx,ns)
  end if
else
  chi=dchi*pi/180.0
  psi=dpsi*pi/180.0
  call agglou1(np,alpha,rindx,ns,chi,psi)
end if

qasca=qasca0/nps + qasca
qext=qext + qext0/nps
qabs=qabs + qabs0/nps
qscah=qscah0/nps + qscah
qexth=qexth + qexth0/nps
qabsh=qabsh + qabsh0/nps
sumxl = sumxl + agxl/nps
do 98 mm=1,ns
  scavvk(mm)=scavvk(mm)+scavv(mm)/nps
  scahhk(mm)=scahhk(mm)+scahh(mm)/nps
  scavhk(mm)=scavhk(mm)+scavh(mm)/nps
  scahvk(mm)=scahvk(mm)+scahv(mm)/nps
98  continue
qetn=qetn+qetn0/nps
qetk=qetk+qetk0/nps

```

```

qehtn=qehtn+qehtn0/nps
qehtk=qehtk+qehtk0/nps
qetx=qetx+qetx0/nps
qehtx=qehtx+qehtx0/nps
do 99 i=1,ns
    dkvvn(i)=dkvvn(i)+dkvvn0(i)/nps
    dkvvk(i)=dkvvk(i)+dkvvk0(i)/nps
    dkhvn(i)=dkhvn(i)+dkhvn0(i)/nps
    dkhvk(i)=dkhvk(i)+dkhvk0(i)/nps
    dkhhn(i)=dkhhn(i)+dkhhn0(i)/nps
    dkhhk(i)=dkhhk(i)+dkhhk0(i)/nps
    dkvhn(i)=dkvhn(i)+dkvhn0(i)/nps
    dkvhk(i)=dkvhk(i)+dkvhk0(i)/nps
    dkvvx(i)=dkvvx(i)+dkvvx0(i)/nps
    dkhvx(i)=dkhvxi(i)+dkhvxi0(i)/nps
    dkvhx(i)=dkvhx(i)+dkvhx0(i)/nps
    dkhhx(i)=dkhhx(i)+dkhhx0(i)/nps

```

99 continue

100 continue

c—derivatives —————

```

do 211 k=1,ns
    kvve(k)=scavvk(k)/qext
    khve(k)=scahvk(k)/qext
    dkvven(k)=(dkvvn(k)-kvve(k)*qetn)/qext
    dkvvek(k)=(dkvvk(k)-kvve(k)*qetk)/qext
    dkhven(k)=(dkhvn(k)-khve(k)*qetn)/qext
    dkhvek(k)=(dkhvk(k)-khve(k)*qetk)/qext
    dkvvex(k)=(dkvvx(k)-kvve(k)*qetx)/qext
    dkhvex(k)=(dkhvxi(k)-khve(k)*qetx)/qext
    rvv(k)=scavvk(k)/scavvk(ns-k+1)
    rhv(k)=scahvk(k)/scavvk(k)

```

211 continue

do 230 k=1,ns

drvvn(k)=(dkvvn(k)-rvv(k)*dkvvn(ns-k+1))/scavvk(ns-k+1)

```

drvvk(k)=(dkvvk(k)-rvv(k)*dkvvk(ns-k+1))/scavvk(ns-k+1)
drhvvn(k)=(dkhvn(k)-rvv(k)*dkvvn(k))/scavvk(k)
drhv(k)=(dkhvk(k)-rvv(k)*dkvvk(k))/scavvk(k)
drvvx(k)=(dkvvx(k)-rvv(k)*dkvvx(ns-k+1))/scavvk(ns-k+1)
drhv(x(k)=(dkhvx(k)-rvv(k)*dkvvx(k))/scavvk(k)

```

230 continue

```

do 311 k=1,ns
  khhe(k)=scahhk(k)/qexth
  kvhe(k)=scavhk(k)/qexth
  dkhhen(k)=(dkhhn(k)-khhe(k)*qehm)/qexth
  dkhhek(k)=(dkhhk(k)-khhe(k)*qehk)/qexth
  dkvhen(k)=(dkvhn(k)-kvhe(k)*qehm)/qexth
  dkvhk(k)=(dkvhk(k)-kvhe(k)*qehk)/qexth
  dkhhex(k)=(dkhhx(k)-khhe(k)*qehx)/qexth
  dkvhx(k)=(dkvhx(k)-kvhe(k)*qehx)/qexth
  rhh(k)=scahhk(k)/scahhk(ns-k+1)
  rvh(k)=scavhk(k)/scahhk(k)

```

311 continue

```

do 330 k=1,ns
  drhhn(k)=(dkhhn(k)-rhh(k)*dkhhn(ns-k+1))/scahhk(ns-k+1)
  drhhk(k)=(dkhhk(k)-rhh(k)*dkhhk(ns-k+1))/scahhk(ns-k+1)
  drvhn(k)=(dkvhn(k)-rvh(k)*dkhhn(k))/scahhk(k)
  drvhk(k)=(dkvhk(k)-rvh(k)*dkhhk(k))/scahhk(k)
  drhhx(k)=(dkhhx(k)-rhh(k)*dkhhx(ns-k+1))/scahhk(ns-k+1)
  drvhx(k)=(dkvhx(k)-rvh(k)*dkhhx(k))/scahhk(k)

```

330 continue

```

return
end

```

c_____

c—sub: agglou1 _____

c—for chains at a specific orientation _____

c—date of generation: july 15, 1994 — by wujiang lou _____

c—derivatives included in august 1994 - _____

c: qetn(k)(x): derivatives of qext wrt n,k, and xp respectively
 c: qehtn(k)(x): same as qetn(k)(x) but for vertical incidence
 c: dkabn(k)(x): derivatives of differential scattering efficiency
 c——— wrt n,k, and xp. a&b denote polarization(v or h)

```

subroutine agglo1(np,alpha,rindx,ns,chi,psi)
parameter (mnp=100,nd=181)
complex rindx,epsilon,e(3,mnp),esum,fsum,ep(6),theta,phi,
$ cm, eh(3,mnp), eph(6), csumh,fsumh,thetah,phih, ci,
$ e1(3,mnp),eh1(3,mnp),ex(3,mnp),ehx(3,mnp), ctem
character pol*1,chain*1,eff*1
common/p2/pol,eff,chain
common/lou/lu,lu1,lu2,lu3,lu4
common/jl/e, eh
common/jl2/e1, eh1
common/jl3/ex,ehx
common/l2/x(mnp),y(mnp),z(mnp)
common/l1/x0(mnp),y0(mnp),z0(mnp)
common/j2s/scahh(181), scavv(181), scahv(181), scavh(181),
$ cosang(181),sinang(181)
common/qqext/qext,qabs,qsca,qexth,qabsh,qscab
common/loa/qetn,qetk,dkvvn(nd),dkvvk(nd),dkhvn(nd),dkhvk(nd),
$ qehtn,qehtk,dkhhn(nd),dkhhk(nd),dkvhn(nd),dkvhk(nd)
common/lox/qetx,dkvvx(nd),dkhv(x(nd),qehtx,dkhhx(nd),dkvhx(nd)
data pi/3.1415926/

```

```

epsilon=rindx*rindx
alpha2=alpha*alpha
ci=cmplx(0.0,1.0)
if(lu.eq.2)then
  yj1=(sin(alpha)/alpha-cos(alpha))/alpha
else
  yj1=alpha/3.0
end if
call coord(np,alpha,1.,0.0,1.,0.0)

```

```

call zhou1(np,alpha,epsilon)

chicos=cos(chi)
chisin=sin(chi)
psicos=cos(psi)
psisin=sin(psi)
call coord(np,alpha,chicos,chisin,psicos,psisin)
if(eff.eq.'n'.or. eff.eq.'r')then
  call zhou0(np,alpha,epsilon)
else
  if(lu4.eq.0)then
    call zhou3(np,alpha,epsilon)
  else
    call zhou31(np,alpha,rfindx)
  end if
end if

c---extinction & absorption efficiency factors

asum=0.0
esum=(0.,0.)
asumh=0.0
esumh=(0.,0.)
do 40 j=1,np
  ctem=cmplx(cos(z(j)),-sin(z(j)))
  esum=esum+ e(1,j)*ctem
  asum=asum+e(1,j)*conjg(e(1,j))+e(2,j)*conjg(e(2,j))
$           +e(3,j)*conjg(e(3,j))
  esumh=esumh+eh(2,j)*ctem
  asumh=asumh+eh(1,j)*conjg(eh(1,j))+eh(2,j)*conjg(eh(2,j))
$           +eh(3,j)*conjg(eh(3,j))

40  continue
qext=aimag((epsilon-1.)*esum)
qabs=aimag(epsilon-1.0)*asum
qexth=aimag((epsilon-1.)*esumh)
qabsh=aimag(epsilon-1.0)*asumh
qext=4.*yj1/np*qext

```

```

qabs=4.*yj1/np*qabs
qexth=4.*yj1/np*qexth
qabsh=4.*yj1/np*qabsh

c---total scattering efficiency factor, set lu1=0 to skip
if(lu1.eq.0)then
  qscsa=qext-qabs
  qscsh=qexth-qabsh
else
  call lou0(np,alpha,epsilon,qscsa,qscsh)
end if

```

```

c---angular differential scattering efficiency
do 140 k=1,ns
  cangle=cosang(k)
  sangle=sinang(k)
  do 120 l=1,3
    ep(l)=cmplx(0.,0.)
120  eph(l)=cmplx(0.,0.)
    do 132 j=1,np
      rj=z(j)*cangle+y(j)*sangle
      ctem=cmplx(cos(rj),-sin(rj))
      do 130 l=1,3
        ep(l)=ep(l)+ctem*e(l,j)
130  eph(l)=eph(l)+ctem*eh(l,j)
132  continue
    theta=cangle*ep(2)-sangle*ep(3)
    phi=ep(1)
    scahv(k)=theta*conjg(theta)
    scavv(k)=phi*conjg(phi)
    thetah=cangle*eph(2)-sangle*eph(3)
    phih=eph(1)
    scahh(k)=thetah*conjg(thetah)
    scavh(k)=phih*conjg(phih)
140  continue

```

```

c=(cabs(epsilon-1.))**2*alpha**2*yj1*yj1/pi/np
do 170 k=1,ns
scahh(k)=c*scahh(k)
scavh(k)=c*scavh(k)
scahv(k)=c*scahv(k)
170 scavv(k)=c*scavv(k)

```

c—partial derivatives of extinction and differential scattering

```

if(lu4.eq.0)then
  return
end if
c——vertical incidence: qext,cvv and chv wrt (n,k,xp=alpha)
esum=(0.0,0.0)
fsum=(0.0,0.0)
do 250 j=1,np
  cm=cmplx(cos(z(j)),-sin(z(j)))
  esum=esum+ (e(1,j)*2.0*rfindx+(epsilon-1.0)*e1(1,j))*cm
  fsum=fsum+ (ex(1,j)-cmplx(0.0,z(j))*e(1,j)/alpha)*cm
250 continue
qetn=4.0/np*yj1*aimag(esum)
qetk=4.0/np*yj1*real(esum)
qext=(1.0-0.3*alpha2)/alpha/(1.0-0.1*alpha2)*qext
& + 4.*alpha/3.0/np*aimag((epsilon-1.0)*fsum)
temp0=(epsilon-1.0)*conjg((epsilon-1.0))
temp1=alpha2*yj1*yj1/pi/np
tempn=4.0*real(rfindx)*(rfindx*conjg(rfindx)-1.0)
tempk=4.0*aimag(rfindx)*(rfindx*conjg(rfindx)+1.0)
do 210 k=1,ns
cangle=cosang(k)
sangle=sinang(k)
esum=(0.0,0.0)
fsum=(0.0,0.0)
ep(1)=(0.0,0.0)
ep(2)=(0.0,0.0)
ep(5)=(0.0,0.0)

```

```

eph(5)=(0.0,0.0)
do 220 j=1,np
  rj=z(j)*cangle+y(j)*sangle
  cm=cmplx(cos(rj),-sin(rj))
  esum=esum+ e(1,j)*cm
  fsum=fsum+ e1(1,j)*cm
  ep(1)=ep(1)+(cangle*e(2,j)-sangle*e(3,j))*cm
  ep(2)=ep(2)+(cangle*e1(2,j)-sangle*e1(3,j))*cm
  ep(5)=ep(5)+(ex(1,j)-ci*rj/alpha*e(1,j))*cm
  eph(5)=eph(5)+(cangle*(ex(2,j)-e(2,j)*ci*rj/alpha)
  &           -sangle*(ex(3,j)-e(3,j)*ci*rj/alpha))*cm
220 continue
theta=esum*conjg(fsum)+conjg(esum)*fsum
ep(3)=ep(1)*conjg(ep(2))+conjg(ep(1))*ep(2)
phi=cmplx(0.0,1.0)*(conjg(esum)*fsum-esum*conjg(fsum))
ep(4)=cmplx(0.0,1.0)*(conjg(ep(1))*ep(2)-ep(1)*conjg(ep(2)))
dkvvn(k)=scavv(k)/temp0*tempn+temp0*temp1*theta
dkvvk(k)=scavv(k)/temp0*tempk+temp0*temp1*phi
dkhvn(k)=scahv(k)/temp0*tempn+temp0*temp1*ep(3)
dkhvk(k)=scahv(k)/temp0*tempk+temp0*temp1*ep(4)
dkvvx(k)=(4.0-1.2*alpha2)/alpha/(1-0.2*alpha2)*scavv(k)
&           +temp0*temp1*(ep(5)*conjg(esum)+conjg(ep(5))*esum)
dkhvrx(k)=(4.0-1.2*alpha2)/alpha/(1-0.2*alpha2)*scahv(k)
&           +temp0*temp1*(eph(5)*conjg(ep(1))+conjg(eph(5))*ep(1))

```

210 continue

c—derivatives of qexth, cvh, & chh: horizontal incidence.

```

esumh=(0.0,0.0)
fsumh=(0.0,0.0)
do 350 j=1,np
  cm=cmplx(cos(z(j)),-sin(z(j)))
  esumh=esumh+ (eh(2,j)*2.0*rfindx+(epsilon-1.0)*eh1(2,j))*cm
  fsumh=fsumh+ (ehx(1,j)-cmplx(0.0,z(j))*eh(1,j)/alpha)*cm

```

350 continue

```
qehtn=4.0/np*yj1*aimag(esumh)
```

```

qehtk=4.0/np*yj1*real(esumh)
qehtx=(1.0-0.3*alpha2)/alpha/(1.0-0.1*alpha2)*qexth
& + 4.*alpha/3.0/np*aimag((epsilon-1.0)*fsumh)

c-----angular derivatives-----
do 330 k=1,ns
  cangle=cosang(k)
  sangle=sinang(k)
  esumh=(0.0,0.0)
  fsumh=(0.0,0.0)
  eph(1)=0.0
  eph(2)=0.0
  ep(5)=(0.0,0.0)
  eph(5)=(0.0,0.0)
  do 320 j=1,np
    rj=z(j)*cangle+y(j)*sangle
    cm=cmplx(cos(rj),-sin(rj))
    esumh=esumh+ eh(1,j)*cm
    fsumh=fsumh+ eh1(1,j)*cm
    eph(1)=eph(1)+(cangle*eh(2,j)-sangle*eh(3,j))*cm
    eph(2)=eph(2)+(cangle*eh1(2,j)-sangle*eh1(3,j))*cm
    ep(5)=ep(5)+(ehx(1,j)-ci*rj/alpha*eh(1,j))*cm
    eph(5)=eph(5)+(cangle*(ehx(2,j)-eh(2,j)*ci*rj/alpha)
    & -sangle*(ehx(3,j)-eh(3,j)*ci*rj/alpha))*cm

320  continue
  thetah=esumh*conjg(fsumh)+conjg(esumh)*fsumh
  eph(3)=eph(1)*conjg(eph(2))+conjg(eph(1))*eph(2)
  phih=cmplx(0.0,1.0)*(conjg(esumh)*fsumh-esumh*conjg(fsumh))
  eph(4)=cmplx(0.0,1.0)
  $ *(conjg(eph(1))*eph(2)-eph(1)*conjg(eph(2)))
  dkvhk(k)=scavh(k)/temp0*tempn+temp0*temp1*thetah
  dkvhk(k)=scavh(k)/temp0*tempk+temp0*temp1*phih
  dkhhk(k)=scahh(k)/temp0*tempn+temp0*temp1*eph(3)
  dkhhk(k)=scahh(k)/temp0*tempk+temp0*temp1*eph(4)
  dkvhx(k)=(4.0-1.2*alpha2)/alpha/(1-0.2*alpha2)*scavh(k)
  & +temp0*temp1*(ep(5)*conjg(esumh)+conjg(ep(5))*esumh)

```

```
dkhhx(k)=(4.0-1.2*alpha2)/alpha/(1-0.2*alpha2)*scahh(k)
& +temp0*temp1*(eph(5)*conjg(eph(1))+conjg(eph(5))*eph(1))
330 continue
return
end
```

c-----

c--sub: agglou0d

c---- agglou0 with derivatives

c----date of generation: august 20, 1994

c-----

```

subroutine agglou0d(np,alpha,rfindx,ns)
parameter (mnp=100,nd=181)
complex rfindx,epsilon,e(3,mnp),esum,fsum,ep(6),theta,phi,
$ cm, eh(3,mnp), eph(6), esumh,fsumh,thetah,phih,ci,
$ e1(3,mnp),eh1(3,mnp),ex(3,mnp),ehx(3,mnp), ctem
character pol*1,chain*1,eff*1
real scahh(nd),scavv(nd),scahv(nd),scavh(nd),
$ qetn,qetk,dkvvn(nd),dkvvk(nd),dkhvn(nd),dkhvk(nd),
$ qehtn,qehtk,dkhhn(nd),dkhhk(nd),dkvhvn(nd),dkvhk(nd),
$ qetx,qehtx,dkvvx(nd),dkhvx(nd),dkvhx(nd),dkhhx(nd)
common/p2/pol,eff,chain
common/lou/lu,lu1,lu2,lu3,lu4
common/lou1/cospsi(20),sinpsi(20),coschi(20),sinchi(20),w(20),ng
common/jl/e, eh
common/jl2/e1, eh1
common/jl3/ex,ehx
common/l2/x(mnp),y(mnp),z(mnp)
common/l1/x0(mnp),y0(mnp),z0(mnp)

c---orientation averaged quantities
common/j2s/scahh0(181),scavv0(181),scahv0(181),scavh0(181),
$ cosang(181),sinang(181)
common/qqext/qext0,qabs0,qscat0,qexth0,qabsh0,qscat0
common/loa/qetn0,qetk0,dkvvn0(nd),dkvvk0(nd),dkhvn0(nd),
$ dkhvk0(nd),qehtn0,qehtk0,dkhhn0(nd),dkhhk0(nd),
$ dkvhvn0(nd),dkvhk0(nd)
common/lox/qetx0,dkvvx0(nd),dkhvx0(nd),
$ qehtx0,dkhhx0(nd),dkvhx0(nd)

```

pi = 3.1415926

pi2=pi*0.5

```

alpha2=alpha*alpha
epsilon=rfidx*rfidx
ci=cmplx(0.0,1.0)
if(lu.eq.2)then
  yj1=(sin(alpha)/alpha-cos(alpha))/alpha
else
  yj1=alpha/3.0
end if
call coord(np,alpha,1.,0.0,1.,0.0)
call zhou1(np,alpha,epsilon)
qext0=0.
qsca0=0.
qabs0=0.
qexth0=0.
qscah0=0.
qabsh0=0.
qetn0=0.0
qetk0=0.0
qehtn0=0.0
qehtk0=0.0

```

c—data initialization——

```

do 10 k=1,ns
  scahh0(k)=0.
  scahv0(k)=0.
  scavv0(k)=0.
  scavh0(k)=0.
  dkvvn0(k)=0.0
  dkvvk0(k)=0.0
  dkhvn0(k)=0.0
  dkhvk0(k)=0.0
  dkhhn0(k)=0.0
  dkhhk0(k)=0.0
  dkvhn0(k)=0.0
  dkvhk0(k)=0.0

```

10 continue

```

do 420 ip=1,ng
  psicos=cospsi(ip)
  psisin=sinpsi(ip)
do 410 ic=1,ng
  chisin=sinchi(ic)
  chicos=coschi(ic)
  call coord(np,alpha,chicos,chisin,psicos,psisin)

```

```

if(eff.eq.'n'.or. eff.eq.'r')then
  call zhou0(np,alpha,epsilon)
else
  call zhou31(np,alpha,rfindx)
end if

```

c—extinction & absorption efficiency factors

```

asum=0.0
esum=(0.,0.)
asumh=0.0
esumh=(0.,0.)
do 40 j=1,np
  ctem=cmplx(cos(z(j)),-sin(z(j)))
  esum=esum+ e(1,j)*ctem
  asum=asum+e(1,j)*conjg(e(1,j))+e(2,j)*conjg(e(2,j))
$           +e(3,j)*conjg(e(3,j))
  esumh=esumh+eh(2,j)*ctem
  asumh=asumh+eh(1,j)*conjg(eh(1,j))+eh(2,j)*conjg(eh(2,j))
$           +eh(3,j)*conjg(eh(3,j))

```

40 continue

```

qext=aimag((epsilon-1.)*esum)
qabs=aimag(epsilon-1.0)*asum
qexth=aimag((epsilon-1.)*esumh)
qabsh=aimag(epsilon-1.0)*asumh
qext=4.*yj1/np*qext
qabs=4.*yj1/np*qabs
qexth=4.*yj1/np*qexth

```

```

qabsh=4.*yj1/np*qabsh

c—total scattering efficiency factor, set lu1=0 to skip

if(lu1.eq.0)then
  qsca=qext-qabs
  qscah=qexth-qabsh
else
  call lou0(np,alpha,epsilon,qsca,qscah)
end if

c—angular differential scattering efficiency

100  continue
do 140 k=1,ns
  cangle = cosang(k)
  sangle = sinang(k)
  do 120 l=1,3
    ep(l)=cmplx(0.,0.)
120  eph(l)=cmplx(0.,0.)
  do 132 j=1,np
    rj=z(j)*cangle+y(j)*sangle
    ctem=cmplx(cos(rj),-sin(rj))
    do 130 l=1,3
      ep(l)=ep(l)+ctem*e(l,j)
130  eph(l)=eph(l)+ctem*eh(l,j)
  132  continue
  theta=cangle*ep(2)-sangle*ep(3)
  phi=ep(1)
  scahv(k)=theta*conjg(theta)
  scavv(k)=phi*conjg(phi)
  thetah=cangle*eph(2)-sangle*eph(3)
  phih=eph(1)
  scahh(k)=thetah*conjg(thetah)
  scavh(k)=phih*conjg(phih)
140  continue
c=(cabs(epsilon-1.))**2*alpha**2*yj1*yj1/pi/np

```

```

do 170 k=1,ns
  scahh(k)=c*scahh(k)
  scavh(k)=c*scavh(k)
  scahv(k)=c*scahv(k)
170  scavv(k)=c*scavv(k)

c---derivatives of qext, cvv and chv/vertical incidence/
  esum=(0.0,0.0)
  fsum=(0.0,0.0)
  do 250 j=1,np
    cm=cmplx(cos(z(j)),-sin(z(j)))
    esum=esum+ (e(1,j)*2.0*rfindx+(epsilon-1.0)*e1(1,j))*cm
    fsum=fsum+ (ex(1,j)-cmplx(0.0,z(j))*e(1,j)/alpha)*cm
250  continue
  qetn=4.0/np*yj1*aimag(esum)
  qetk=4.0/np*yj1*real(esum)
  qext=(1.0-0.3*alpha2)/alpha/(1.0-0.1*alpha2)*qext
  & + 4.*alpha/3.0/np*aimag((epsilon-1.0)*fsum)
  temp0=(epsilon-1.0)*conjg((epsilon-1.0))
  temp1=alpha2*yj1*yj1/pi/np
  tempn=4.0*real(rfindx)*(rfindx*conjg(rfindx)-1.0)
  tempk=4.0*imag(rfindx)*(rfindx*conjg(rfindx)+1.0)
  do 230 k=1,ns
    cangle=cosang(k)
    sangle=sinang(k)
    esum=(0.0,0.0)
    fsum=(0.0,0.0)
    ep(1)=0.0
    ep(2)=0.0
    ep(5)=(0.0,0.0)
    eph(5)=(0.0,0.0)
    do 220 j=1,np
      rj=z(j)*cangle+y(j)*sangle
      cm=cmplx(cos(rj),-sin(rj))
      esum=esum+ e(1,j)*cm
220  continue
230  continue

```

```

fsum=fsum+ e1(1,j)*cm
ep(1)=ep(1)+(cangle*e(2,j)-sangle*e(3,j))*cm
ep(2)=ep(2)+(cangle*e1(2,j)-sangle*e1(3,j))*cm
ep(5)=ep(5)+(ex(1,j)-ci*rj/alpha*e(1,j))*cm
eph(5)=eph(5)+(cangle*(ex(2,j)-e(2,j)*ci*rj/alpha)
& -sangle*(ex(3,j)-e(3,j)*ci*rj/alpha))*cm

```

220 continue

```

theta=esum*conjg(fsum)+conjg(esum)*fsum
ep(3)=ep(1)*conjg(ep(2))+conjg(ep(1))*ep(2)
phi=cmplx(0.0,1.0)*(conjg(esum)*fsum-esum*conjg(fsum))
ep(4)=cmplx(0.0,1.0)*(conjg(ep(1))*ep(2)-ep(1)*conjg(ep(2)))
dkvvn(k)=scavv(k)/temp0*tempn+temp0*temp1*theta
dkvvk(k)=scavv(k)/temp0*tempk+temp0*temp1*phi
dkhvn(k)=scahv(k)/temp0*tempn+temp0*temp1*ep(3)
dkhvk(k)=scahv(k)/temp0*tempk+temp0*temp1*ep(4)
dkvvx(k)=(4.0-1.2*alpha2)/alpha/(1-0.2*alpha2)*scavv(k)
& +temp0*temp1*(ep(5)*conjg(esum)+conjg(ep(5))*esum)
dkhv(x(k)=(4.0-1.2*alpha2)/alpha/(1-0.2*alpha2)*scahv(k)
& +temp0*temp1*(eph(5)*conjg(ep(1))+conjg(eph(5))*ep(1))

```

230 continue

c—derivatives of qexth, cvh, & chh

```

esumh=(0.0,0.0)
fsumh=(0.0,0.0)
do 350 j=1,np
  cm=cmplx(cos(z(j)),-sin(z(j)))
  esumh=esumh+ (eh(2,j)*2.0*rfindx+(epsilon-1.0)*ch1(2,j))*cm
  fsumh=fsumh+ (ehx(1,j)-cmplx(0.0,z(j))*eh(1,j)/alpha)*cm

```

350 continue

```

qehtn=4.0/np*yj1*aimag(esumh)
qehtk=4.0/np*yj1*real(esumh)
qehtx=(1.0-0.3*alpha2)/alpha/(1.0-0.1*alpha2)*qexth
& + 4.*alpha/3.0/np*aimag((epsilon-1.0)*fsumh)
temp0=(epsilon-1.0)*conjg((epsilon-1.0))
temp1=alpha**2*yj1*yj1/pi/np

```

```

tempn=4.0*real(rfindx)*(rfindx*conjg(rfindx)-1.0)
tempk=4.0*aimag(rfindx)*(rfindx*conjg(rfindx)+1.0)
do 310 k=1,ns
cangle=cosang(k)
sangle=sinang(k)
esumh=(0.0,0.0)
fsumh=(0.0,0.0)
eph(1)=0.0
eph(2)=0.0
ep(5)=(0.0,0.0)
eph(5)=(0.0,0.0)
do 320 j=1,np
rj=z(j)*cangle+y(j)*sangle
cm=cmplx(cos(rj),-sin(rj))
esumh=esumh+ eh(1,j)*cm
fsumh=fsumh+ eh1(1,j)*cm
eph(1)=eph(1)+(cangle*eh(2,j)-sangle*eh(3,j))*cm
eph(2)=eph(2)+(cangle*eh1(2,j)-sangle*eh1(3,j))*cm
ep(5)=ep(5)+(ehx(1,j)-ci*rj/alpha*eh(1,j))*cm
eph(5)=eph(5)+(cangle*(ehx(2,j)-eh(2,j)*ci*rj/alpha)
& -sangle*(ehx(3,j)-eh(3,j)*ci*rj/alpha))*cm
320 continue
thetah=esumh*conjg(fsumh)+conjg(esumh)*fsumh
eph(3)=eph(1)*conjg(eph(2))+conjg(eph(1))*eph(2)
phih=cmplx(0.0,1.0)*(conjg(esumh)*fsumh-esumh*conjg(fsumh))
eph(4)=cmplx(0.0,1.0)
$ *(conjg(eph(1))*eph(2)-eph(1)*conjg(eph(2)))
dkvhn(k)=scavh(k)/temp0*tempn+temp0*temp1*thetah
dkvhk(k)=scavh(k)/temp0*tempk+temp0*temp1*phih
dkhhn(k)=scahh(k)/temp0*tempn+temp0*temp1*eph(3)
dkhhk(k)=scahh(k)/temp0*tempk+temp0*temp1*eph(4)
dkvhx(k)=(4.0-1.2*alpha2)/alpha/(1-0.2*alpha2)*scavh(k)
& +temp0*temp1*(ep(5)*conjg(esumh)+conjg(ep(5))*esumh)
dkhhx(k)=(4.0-1.2*alpha2)/alpha/(1-0.2*alpha2)*scahh(k)
& +temp0*temp1*(eph(5)*conjg(eph(1))+conjg(eph(5))*eph(1))

```

310 continue

c—orientation averages

```
temp=w(ic)*w(ip)*chisin*pi/8.0
qext0=qext0+qext*temp
qabs0=qabs0+qabs*temp
qsca0=qsca0+qsca*temp
qexth0=qexth0+qexth*temp
qabsh0=qabsh0+qabsh*temp
qscah0=qscah0+qscah*temp
qetn0=qetn0+qetn*temp
qetk0=qetk0+qetk*temp
qehtn0=qehtn0+qehtn*temp
qehtk0=qehtk0+qehtk*temp
qetx0=qetx0+qetx*temp
qehtx0=qehtx0+qehtx*temp
do 360 k=1,ns
  scavv0(k)=scavv0(k)+scavv(k)*temp
  scahv0(k)=scahv0(k)+scahv(k)*temp
  scahh0(k)=scahh0(k)+scahh(k)*temp
  scavh0(k)=scavh0(k)+scavh(k)*temp
  dkvvn0(k)=dkvvn0(k)+dkvvn(k)*temp
  dkvvk0(k)=dkvvk0(k)+dkvvk(k)*temp
  dkhvn0(k)=dkhvn0(k)+dkhvn(k)*temp
  dkhvk0(k)=dkhvk0(k)+dkhvk(k)*temp
  dkhhn0(k)=dkhhn0(k)+dkhhn(k)*temp
  dkhhk0(k)=dkhhk0(k)+dkhhk(k)*temp
  dkvhn0(k)=dkvhn0(k)+dkvhn(k)*temp
  dkvhk0(k)=dkvhk0(k)+dkvhk(k)*temp
  dkvvx0(k)=dkvvx0(k)+dkvvx(k)*temp
  dkhvx0(k)=dkhvx0(k)+dkhvx(k)*temp
  dkvhx0(k)=dkvhx0(k)+dkvhx(k)*temp
  dkhhx0(k)=dkhhx0(k)+dkhhx(k)*temp
```

360 continue

410 continue

420 continue

return

end

c-----
c---agglou0: orientation averaged version of agglou1
c----- gaussian integration (ng points, ng <=20)/3-12-95-----
c-----wlou-----

```
subroutine agglou0(np,alpha,epsilon,ns)
parameter (mnp=100)
complex epsilon,e(3,mnp),esum,fsum,ep(6),theta,phi,
$ cm, eh(3,mnp), cph(6), esumh,fsumh,thetah,phih,ci,
$ e1(3,mnp),eh1(3,mnp),ex(3,mnp),ehx(3,mnp), ctem
character pol*1,chain*1,eff*1
real scahh(181),scavv(181),scahv(181),scavh(181)
common/p2/pol,eff,chain
common/lou/lu,lu1,lu2,lu3,lu4
common/lou1/cospsi(20),sinpsi(20),coschi(20),sinchi(20),w(20),ng
common/jl/e, eh
common/jl2/e1, eh1
common/jl3/ex,ehx
common/l2/x(mnp),y(mnp),z(mnp)
common/l1/x0(mnp),y0(mnp),z0(mnp)
```

c---orientation averaged quantities
common/j2s/scahh0(181),scavv0(181),scahv0(181),scavh0(181),
\$ cosang(181),sinang(181)
common/qqext/qext0,qabs0,qsca0,qexth0,qabsh0,qscah0

```
pi = 3.1415926
pi2=pi*0.5
alpha2=alpha*alpha
ci=cmplx(0.0,1.0)
if(lu.eq.2)then
  yj1=(sin(alpha)/alpha-cos(alpha))/alpha
else
  yj1=alpha/3.0
end if
gang=4.*yj1/np
c=(epsilon-1.)*conjg(epsilon-1.0)*alpha2*yj1*yj1/pi/np
```

```

call coord(np,alpha,1.,0.0,1.,0.0)
call zhou1(np,alpha,epsilon)

c---data initialization---
qext0=0.
qsca0=0.
qabs0=0.
qexth0=0.
qscah0=0.
qabsh0=0.
do 10 k=1,ns
  scahh0(k)=0.
  scahv0(k)=0.
  scavv0(k)=0.
  scavh0(k)=0.

10  continue
do 420 ip=1,ng
  psicos=cospsi(ip)
  psisin=sinpsi(ip)
  do 410 ic=1,ng
    chisin=sinchi(ic)
    chicos=coschi(ic)
    call coord(np,alpha,chicos,chisin,psicos,psisin)

    if(eff.eq.'n'.or. eff.eq.'r')then
      call zhou0(np,alpha,epsilon)
    else
      call zhou3(np,alpha,epsilon)
    end if

c---extinction & absorption effiency factors
asum=0.0
esum=(0.,0.)
asumh=0.0
esumh=(0.,0.)
do 40 j=1,np

```

```

ctem=cmplx(cos(z(j)),-sin(z(j)))
esum=esum+ e(1,j)*ctem
asum=asum+e(1,j)*conjg(e(1,j))+e(2,j)*conjg(e(2,j))
$           +e(3,j)*conjg(e(3,j))
esumh=esumh+eh(2,j)*ctem
asumh=asumh+eh(1,j)*conjg(eh(1,j))+eh(2,j)*conjg(eh(2,j))
$           +eh(3,j)*conjg(eh(3,j))

```

40 continue

```

qext=aimag((epsilon-1.)*esum)
qabs=aimag(epsilon-1.0)*asum
qexth=aimag((epsilon-1.)*esumh)
qabsh=aimag(epsilon-1.0)*asumh
qext= gang*qext
qabs= gang*qabs
qexth= gang*qexth
qabsh= gang*qabsh

```

c---total scattering efficiency factor, set lu1=0 to skip

```

if(lu1.eq.0)then
  qsc= qext-qabs
  qsc= qexth-qabsh
else
  call lou0(np,alpha,epsilon,qsc,qsc)
end if
do 140 k=1,ns
  cangle = cosang(k)
  sangle = sinang(k)
  do 120 l=1,3
    ep(l)=cmplx(0.,0.)
120  eph(l)=cmplx(0.,0.)
  do 132 j=1,np
    rj=z(j)*cangle+y(j)*sangle
    ctem=cmplx(cos(rj),-sin(rj))
    do 130 l=1,3
      ep(l)=ep(l)+ctem*e(l,j)

```

```

130      eph(l)=eph(l)+ctem*eh(l,j)
132  continue
      theta=cangle*ep(2)-sangle*ep(3)
      phi=ep(1)
      scahv(k)=theta*conjg(theta)
      scavv(k)=phi*conjg(phi)
      thetah=cangle*eph(2)-sangle*eph(3)
      phih=eph(1)
      scahh(k)=thetah*conjg(thetah)
      scavh(k)=phih*conjg(phih)
140  continue
      do 170 k=1,ns
      scahh(k)=c*scahh(k)
      scavh(k)=c*scavh(k)
      scahv(k)=c*scahv(k)
170      scavv(k)=c*scavv(k)

```

c—orientation averages

```

temp=w(ic)*w(ip)*chisin*pi/8.0
qext0=qext0+qext*temp
qabs0=qabs0+qabs*temp
qsca0=qsca0+qsca*temp
qexth0=qexth0+qexth*temp
qabsh0=qabsh0+qabsh*temp
qscah0=qscah0+qscah*temp
      do 360 k=1,ns
      scavv0(k)=scavv0(k)+scavv(k)*temp
      scahv0(k)=scahv0(k)+scahv(k)*temp
      scahh0(k)=scahh0(k)+scahh(k)*temp
      scavh0(k)=scavh0(k)+scavh(k)*temp
360  continue
410  continue
420  continue

```

return

end

c
c--sub: zhou0 solves the internal field under non-coupling option
c-- (eff='n') in the measuring coordinate system (x,y,z)
c-- it also gives the internal field of the rayleigh-gans theory
c-- (eff='r') addedon friday, 10-14-94 by w. lou

c
subroutine zhou0(np,alpha,epsilon)
parameter (mnp=100, mn3=mnp*3)
complex epsilon,b(mn3),bh(mn3),c,d,c1
character pol*1, eff*1, chain*1
common/p2/pol,eff,chain
common/lou/lu,lu1,lu2,lu3,lu4
common/jl/b,bh
common/l2/x(mnp),y(mnp),z(mnp)
if(eff .eq. 'r')then
do 60 i=1,np
c=cmplx(cos(z(i)),sin(z(i)))
nrow0=3*(i-1)
bh(nrow0+1)=(0.0,0.0)
bh(nrow0+2)=c
bh(nrow0+3)=(0.0,0.0)
b(nrow0+1)=c
b(nrow0+2)=(0.0,0.0)
b(nrow0+3)=(0.0,0.0)
60 continue
else
c1=3./(epsilon+2.)
if(lu.eq.1)then
d1=2.0*alpha/3.0
d=(1.0,0.)-alpha*alpha*(epsilon-1.)/(epsilon+2.)*cmplx(1.0,d1)
else if(lu.eq.0)then
d=(1.0,0.0)
else if(lu.eq.2)then
yj1=(sin(alpha)/alpha-cos(alpha))/alpha
yy1=-(cos(alpha)/alpha+sin(alpha))/alpha

```

yih1=cmplx(-yy1,yj1)
d=(3.0*epsilon-(epsilon-1.)*2.*alpha**2*yih1)/(epsilon+2.)
else
end if
do 64 i=1,np
  c=cmplx(cos(z(i)),sin(z(i)))
  nrow0=3*(i-1)
  bh(nrow0+1)=(0.0,0.0)
  bh(nrow0+2)=c*c1/d
  bh(nrow0+3)=(0.0,0.0)
  b(nrow0+1)=c*c1/d
  b(nrow0+2)=(0.0,0.0)
  b(nrow0+3)=(0.0,0.0)
64  continue
end if
return
end

```

c

c—sub: zhoul establishes the matrix a for the internal field

c— in the structural coordinate system (x',y',z')

subroutine zhoul(np,alpha,epsilon)

```
parameter (mnp=100, mn3=mnp*3)
complex epsilon,a(mn3,mn3), a1(mn3,mn3), t(3,3),c,d,ctem
character eff*1,pol*1,chain*1
common/lou/lu,lu1,lu2,lu3,lu4
common/jla/a,al
common/l1/x0(mnp),y0(mnp),z0(mnp)
common/p2/pol,eff,chain
pi=3.1415926
nrank=3*np
if (eff.eq.'n')then
  return
else if (eff.eq.'f') then
  ctem=cmplx(0.,-1.)
else if (eff.eq.'w') then
  ctem=cmplx(0.,1.)
endif
c=alpha**3*(epsilon-1.)/(3.*epsilon+2.)*ctem
if(lu.eq.1)then
  d1=2.0*alpha/3.0
  d=(1.0,0.0)-alpha*alpha*(epsilon-1.)/(epsilon+2.)*cmplx(1.0,d1)
else if(lu.eq.0)then
  d=(1.0,0.0)
else if(lu.eq.2)then
  yj1=(sin(alpha)/alpha-cos(alpha))/alpha
  c=alpha**2*(epsilon-1.)/(epsilon+2.)*ctem*yj1
  yy1=-(cos(alpha)/alpha+sin(alpha))/alpha
  yih1=cmplx(-yy1,yj1)
  d=(3.0*epsilon-(epsilon-1.)*2.*alpha**2*yih1)/(epsilon+2.)
else
end if
do 10 i=1,np
```

```

nrow0=1+3*(i-1)
nrowe=3*i
do 20 nrow=nrow0,nrowe
do 20 ncol=nrow,nrowe
a(nrow,ncol)=(0.0,0.0)
if (ncol.eq.nrow)then
  a(nrow,ncol)=d
endif
20 continue
if(i .eq. np) goto 10
ir=i+1
do 30 j=ir,np
  dx=x0(j)-x0(i)
  dy=y0(j)-y0(i)
  dz=z0(j)-z0(i)
  dj=sqrt(dx*dx+dy*dy+dz*dz)
  dj2=sqrt(dx*dx+dy*dy)
  chicos=dz/dj
  chisin=dj2/dj
  if(dj2.le.0.1e-30)then
    psicos=1.0
    psisin=0.0
  else
    psicos=dx/dj2
    psisin=dy/dj2
  end if
  djk=dj*2.0*alpha
  call tmatrix(djk,chicos,chisin,psicos,psisin,t)
  ncol0=3*(j-1)
  do 40 nc=1,3
    do 40 nrow=nrow0,nrowe
40  a(nrow,ncol0+nc)=c*t(nrow-nrow0+1,nc)
30 continue
10 continue
do 50 nrow=2,nrank

```

```
ncoldg=nrow-1
do 50 ncol=1,ncoldg
50  a(nrow,ncol)=a(ncol,nrow)
    if(eff.eq.'f')then
        do 56 i=1,nrank
        do 56 j=1,nrank
56      a1(i,j)=a(i,j)
        call cbdecp(a,nrank)
    else
        do 60 i=1,nrank
60      a(i,i)=(1.0,0.0)
    endif
    return
end
```

```

c_____
c--sub: zhou3 solves the internal field in the (x',y',z') system
c_____
c-- then transforms it into the measuring coordinate

subroutine zhou3(np,alpha,epsilon)
parameter (mnp=100, mn3=mnp*3)
complex epsilon,a(mn3,mn3),b(mn3),bh(mn3),c,d ,b1(mn3),
$ ex, ey, ez, exh, eyh, ezh, a1(mn3,mn3),
$ bs(mn3), bhs(mn3)
real t(3,3)
character eff*1,pol*1,chain*1
common/jl/b,bh
common/jle/bs,bhs
common/jla/a,a1
common/l2/x(mnp),y(mnp),z(mnp)
common/p2/pol,eff,chain
common/lou/lu,lu1,lu2,lu3,lu4
common/trans1/t
nrank=3*np
do 64 i=1,np
  c=cmplx(cos(z(i)),sin(z(i)))
  nrow0=3*(i-1)
  bh(nrow0+1)=c*t(2,1)
  bh(nrow0+2)=c*t(2,2)
  bh(nrow0+3)=c*t(2,3)
  b(nrow0+1)=c*t(1,1)
  b(nrow0+2)=c*t(1,2)
  b(nrow0+3)=c*t(1,3)
64 continue
d=3./epsilon+2.)
if (eff.eq.'f') then
  do 70 i=1,nrank
    b(i)=b(i)*d
70  bh(i)=bh(i)*d
    call cbsolx(a,b,nrank)
    call cbsolx(a,bh,nrank)

```

```

else if(eff.eq.'w')then
do 80 i=1,nrank .
b1(i)=cmplx(0.,0.)
do 80 j=1,nrank
80    b1(i)=b1(i)+a(j,i)*b(j)
do 85 i=1,nrank
b(i)=cmplx(0.,0.)
do 85 j=1,nrank
85    b(i)=b(i)+a(j,i)*bh(j)
if(lu.eq.1)then
d1=2.0*alpha/3.0
c=(1.0,0.)-alpha*alpha*(epsilon-1.)/(epsilon+2.)*cmplx(1.0,d1)
else if(lu.eq.0)then
c=(1.0,0.0)
else if(lu.eq.2)then
yj1=(sin(alpha)/alpha-cos(alpha))/alpha
yy1=-(cos(alpha)/alpha+sin(alpha))/alpha
yih1=cmplx(-yy1,yj1)
c=(3.0*epsilon-(epsilon-1.)*2.*alpha**2*yih1)/(epsilon+2.)
else
end if
do 90 i=1,nrank
bh(i)=b(i)*d/c
90    b(i)=b1(i)*d/c
else
stop
end if
do 100 i=1,np
i1 = 3*(i-1)+1
i2 = i1 + 1
i3 = i1 + 2
bs(i1)= b(i1)
bs(i2)= b(i2)
bs(i3)= b(i3)
bhs(i1)= bh(i1)

```

```
bhs(i2)= bh(i2)
bhs(i3)= bh(i3)
ex=b(i1)*t(1,1)+b(i2)*t(1,2)+b(i3)*t(1,3)
ey=b(i1)*t(2,1)+b(i2)*t(2,2)+b(i3)*t(2,3)
ez=b(i1)*t(3,1)+b(i2)*t(3,2)+b(i3)*t(3,3)
exh=bh(i1)*t(1,1)+bh(i2)*t(1,2)+bh(i3)*t(1,3)
eyh=bh(i1)*t(2,1)+bh(i2)*t(2,2)+bh(i3)*t(2,3)
ezh=bh(i1)*t(3,1)+bh(i2)*t(3,2)+bh(i3)*t(3,3)
b(i1)=ex
b(i2)=ey
b(i3)=ez
bh(i1)=exh
bh(i2)=eyh
bh(i3)=ezh
100 continue
return
end
```

c---sub: lou0 computes total scattering efficiency factor

c--- in the structural coordinate system

subroutine lou0(np,alpha,epsilon,qsca,qscah)

parameter (mnp=100, mn3=mnp*3)

complex epsilon,a(mn3,mn3),c,d ,a1(mn3,mn3),

\$ bs(mn3), bhs(mn3),bjl0,bjh0,ctem

character eff*1,pol*1,chain*1

common/p2/pol,eff,chain

common/jle/ba,bhs

common/jla/a,a1

common/lou/lu,lu1,lu2,lu3,lu4

if (eff.eq.'n')then

 return

else if (eff.eq.'f') then

 ctem=cmplx(0.,-1.)

else if (eff.eq.'w') then

 ctem=cmplx(0.,1.)

endif

c=alpha**3*(epsilon-1.)/(3.*(epsilon+2.))*ctem

bjl = alpha/3.0

if(lu.eq.1)then

 d1=2.0*alpha/3.0

 d=(1.0,0.0)-alpha*alpha*(epsilon-1.)/(epsilon+2.)*cmplx(1.0,d1)

else if(lu.eq.0)then

 d=(1.0,0.0)

else if(lu.eq.2)then

 yj1=(sin(alpha)/alpha-cos(alpha))/alpha

 c=alpha**2*(epsilon-1.)/(epsilon+2.)*ctem*yj1

else

end if

bjl = 0.0

bjh = 0.0

do 64 j=1,np

```

do 64 l=1,np
  if(j .eq. l)then
    do 50 j2 =1, 3
      j1 =(j-1)*3+j2
      bj1 =bj1 + 2.0* bs(j1)*conjg(bs(j1))
      bj1h =bj1h + 2.0* bhs(j1)*conjg(bhs(j1))
  50  continue
  else
    do 54 j2 =1,3
      j1=(j-1)*3+j2
      bj10 =(0.0,0.0)
      bj1h0 =(0.0,0.0)
      do 52 l2 =1,3
        l1=(l-1)*3+l2
        z = real(a1(j1,l1)/c)
        bj10 = bj10 + z*conjg(bs(l1))
  52  bj1h0 = bj1h0 + z*conjg(bhs(l1))
        bj1 =bj1 +bj10*bs(j1)
  54  bj1h =bj1h +bj1h0*bhs(j1)
    end if
  64  continue
  qsca = bj1*4.0/3.0/np*alpha*alpha*yj1*yj1
  $  *(epsilon-1.0)*conjg(epsilon-1.0)
  qscah = bj1h/bj1*qsca
  return
end

```

```

c
c--sub: lou1
c-- generate cosine and sine of the gausian points(ng points
c--date of generation: december 21, 1994 lou-
c

subroutine lou10
parameter (ngs=10)
real zx(20),w(20),zx6(3),w6(3),zx8(4),w8(4),zx10(5),w10(5),
& zx12(6),w12(6),zx16(8),w16(8),zx20(10),w20(10)
common/lou1/cospsi(20),sinpsi(20),coschi(20),sinchi(20),w,ng
data pi/3.1415926/
data zx16/0.09501251,0.28160355,0.45801678,0.61787624,
& .75540441,.86563120,.94457502,.98940093/, w16/0.18945061,
& 0.18260342,0.16915652,0.14959599,0.12462897,0.09515851,
& 0.06225352,0.02715246/
data zx12/.12523341,.36783150,.58731795,.76990267,.90411726,
& .98156063/, w12/.24914705,.23349254,.20316743,.16007833,
& .10693933,.04717534/
data zx10/.14887434,.43339539,.67940957,.86506337,.97390653/,
$ w10/.29552422,.2692667,.2190864,.14945135,.06667134/
data zx8/.18343464,.52553241,.79666648,.96028986/,
& w8/.36268378,.31370665,.22238103,.10122854/
data zx6/.23861919,.66120939,.93246951/,
& w6/.46791393,0.36076157,0.17132449/
pi2=pi*0.5
ng = ngs
if(ngs .eq. 6)then
  do 12 i=1,ngs/2
    zx(i+ngs/2)=zx6(i)
    zx(i)=-zx6(ngs/2-i+1)
    w(i+ngs/2)=w6(i)
12      w(i)=w6(ngs/2-i+1)
else if(ngs .eq. 8)then
  do 13 i=1,ngs/2
    zx(i+ngs/2)=zx8(i)

```

```

zx(i)= -zx8(ngs/2-i+1)
w(i+ngs/2)=w8(i)

13      w(i)= w8(ngs/2-i+1)

else if(ngs .eq. 10)then
  do 14 i=1,ngs/2
    zx(i+ngs/2)=zx10(i)
    zx(i)= -zx10(ngs/2-i+1)
    w(i+ngs/2)=w10(i)

14      w(i)= w10(ngs/2-i+1)

else if(ngs .eq. 12)then
  do 15 i=1,ngs/2
    zx(i+ngs/2)=zx12(i)
    zx(i)= -zx12(ngs/2-i+1)
    w(i+ngs/2)=w12(i)

15      w(i)= w12(ngs/2-i+1)

else if(ngs .eq. 16)then
  do 16 i=1,ngs/2
    zx(i+ngs/2)=zx16(i)
    zx(i)= -zx16(ngs/2-i+1)
    w(i+ngs/2)=w16(i)

16      w(i)= w16(ngs/2-i+1)

else
  print *, 'no gaussian available-in sub lou1'
  stop
end if

do 20 i=1,ng
  psi=(zx(i)+1.)*pi
  cospsi(i)=cos(psi)
  sinpsi(i)=sin(psi)

20  continue

do 40 i=1,ng
  chi=(zx(i)+1.)*pi2
  sinchi(i)=sin(chi)
  coschi(i)=cos(chi)

40  continue

```

return

end

c
c--sub: zhou31
c—— zhou3 with derivatives of internal field wrt (n,k)& xp
c—— output in common/jl2/&/jl3/. full coupling only.
c——lou, august 20(n,k), and september 28, 1994 for xp's

```
subroutine zhou31(np,alpha,rfindx)
parameter (mnp=100, mn3=mnp*3)
complex rfindx,epsilon,a(mn3,mn3),b(mn3),bh(mn3),c,d,c1,c1x,
& ex, ey, ez, exh, eyh, ezh, b1(mn3),bh1(mn3),
& a1(mn3,mn3), bx(mn3),bhx(mn3),h0,h1,h2,bs(mn3),bhs(mn3)
real t(3,3)
character eff*1,chain*1,pol*1
common/jl/b,bh
common/jle/b$b,bs
common/jl2/b1,bh1
common/jl3/bx,bhx
common/jla/a,a1
common/l2/x(mnp),y(mnp),z(mnp)
common/p2/pol,eff,chain
common/lou/lu,lu1,lu2,lu3,lu4
common/trans1/t
```

```
nrank=3*np
epsilon=rfindx*rfindx
ez=(epsilon-1.0)/(epsilon+2.0)
d=3.0/(epsilon+2.0)
alpha2=alpha*alpha
s0=sin(alpha)
c0=cos(alpha)
z1=c0+alpha*s0
z2=s0-alpha*c0
c1=d+ez*(3.0-2.0*cmplx(z1,z2)).
c1x=-2.0*cmplx(c0,s0)*ez
```

c--incoming wave rotation

```
do 64 i=1,np
```

```

c=cmplx(cos(z(i)),sin(z(i)))
nrow0=3*(i-1)
bh(nrow0+1)=c*t(2,1)
bh(nrow0+2)=c*t(2,2)
bh(nrow0+3)=c*t(2,3)
b(nrow0+1)=c*t(1,1)
b(nrow0+2)=c*t(1,2)
b(nrow0+3)=c*t(1,3)

```

64 continue

c—internal field in the structural coordinate system, including
c——derivatives of the field. full coupling only.

```

if (eff.eq.'f') then
  do 70 i=1,nrank
    b(i)=b(i)*d
    bh(i)=bh(i)*d
    b1(i)=b(i)
70      bh1(i)=bh(i)
      call cbsolx(a,b,nrank)
      call cbsolx(a,bh,nrank)

```

c——derivatives w.r.t. size parameter alpha

```

c=cmplx(0.0,-1.0)*alpha2*alpha*ez/3.0
do 58 l=1,np
  do 56 m=1,3
    n1=3*(l-1)+m
    ex=(0.0,0.0)
    ey=(0.0,0.0)
    exh=(0.0,0.0)
    eyh=(0.0,0.0)
    do 54 j=1,np
      n2=3*(j-1)+m
      n3=3*(j-1)
      if(j.eq.l)go to 54
      rho=sqrt((x(l)-x(j))*(x(l)-x(j))+(y(l)-y(j))
      * (y(l)-y(j))+(z(l)-z(j))*(z(l)-z(j)))
      s0=sin(rho)

```

```

c0=cos(rho)
h0=cmplx(s0,-c0)/rho
z1=(3./rho/rho-1.)*s0-3.*c0/rho
z2=(1.-3./rho/rho)*c0-3.*s0/rho
h2=cmplx(z1,z2)/rho
h1=rho/3.0*(h0+h2)
ex=ex + 2.*c*b(n2)*(rho*h1 - 3.*h0 + rho*h1*h0/h2)
ey=ey + rho*h1/h2*(a1(n1,n3+1)*b(n3+1)
& + a1(n1,n3+2)*b(n3+2)+a1(n1,n3+3)*b(n3+3))
exh=exh + 2.*c*bh(n2)*(rho*h1 - 3.*h0 + rho*h1*h0/h2)
eyh=eyh + rho*h1/h2*(a1(n1,n3+1)*bh(n3+1)
& + a1(n1,n3+2)*bh(n3+2)+a1(n1,n3+3)*bh(n3+3))

54    continue
bx(n1)=b1(n1)*cmplx(-alpha/3.0,z(l)/alpha)
& + b(n1)*alpha*(c1/3.0-c1x) + (ex-ey)/alpha
56    bhx(n1)=bh1(n1)*cmplx(-alpha/3.0,z(l)/alpha)
& + bh(n1)*alpha*(c1/3.0-c1x) + (exh-eyh)/alpha
58    continue
call cbsolx(a,bx,nrank)
call cbsolx(a,bhx,nrank)
c----derivatives w.r.t. refractive index (n,k)
do 72 i=1,nrank
    bh1(i)=(d*bh(i)-bh1(i))/(epsilon-1.0)*2.*rfindx
    b1(i)=(d*b(i)-b1(i))/(epsilon-1.0)*2.0*rfindx
72    continue
call cbsolx(a,b1,nrank)
call cbsolx(a,bh1,nrank)
else if(eff.eq.'w')then
    do 80 i=1,nrank
        b1(i)=cmplx(0.,0.)
        do 80 j=1,nrank
            b1(i)=b1(i)+a(j,i)*b(j)
80    b1(i)=b1(i)+a(j,i)*b(j)
    do 85 i=1,nrank
        b(i)=cmplx(0.,0.)
        do 85 j=1,nrank

```

```

85    b(i)=b(i)+a(j,i)*bh(j)
      if(lu.eq.1)then
        d1=2.0*alpha/3.0
        c=(1.0,0.0)-alpha*alpha*(epsilon-1.)/(epsilon+2.)*cmplx(1.0,d1)
      else if(lu.eq.0)then
        c=(1.0,0.0)
      else if(lu.eq.2)then
        yj1=(sin(alpha)/alpha-cos(alpha))/alpha
        yy1=-(cos(alpha)/alpha+sin(alpha))/alpha
        yih1=cmplx(-yy1,yj1)
        c=(3.0*epsilon-(epsilon-1.)*2.*alpha**2*yih1)/(epsilon+2.)
      else
        end if
      do 90 i=1,nrank
        bh(i)=b(i)*d/c
90    b(i)=b1(i)*d/c
      else
        stop
      end if

```

c—field&derivative rotate back to the measuring coordinate system

```

      do 100 i=1,np
        i1 = 3*(i-1)+1
        i2 = i1 + 1
        i3 = i1 + 2
        bs(i1)= b(i1)
        bs(i2)= b(i2)
        bs(i3)= b(i3)
        bhs(i1)= bh(i1)
        bhs(i2)= bh(i2)
        bhs(i3)= bh(i3)
        ex=b(i1)*t(1,1)+b(i2)*t(1,2)+b(i3)*t(1,3)
        ey=b(i1)*t(2,1)+b(i2)*t(2,2)+b(i3)*t(2,3)
        ez=b(i1)*t(3,1)+b(i2)*t(3,2)+b(i3)*t(3,3)
        exh=bh(i1)*t(1,1)+bh(i2)*t(1,2)+bh(i3)*t(1,3)
        eyh=bh(i1)*t(2,1)+bh(i2)*t(2,2)+bh(i3)*t(2,3)

```

ezh=bh(i1)*t(3,1)+bh(i2)*t(3,2)+bh(i3)*t(3,3)

b(i1)=ex

b(i2)=ey

b(i3)=ez

bh(i1)=exh

bh(i2)=eyh

bh(i3)=ezh

100 continue

do 102 i=1,np

i1 = 3*(i-1)+1

i2 = i1 + 1

i3 = i1 + 2

ex=b1(i1)*t(1,1)+b1(i2)*t(1,2)+b1(i3)*t(1,3)

ey=b1(i1)*t(2,1)+b1(i2)*t(2,2)+b1(i3)*t(2,3)

ez=b1(i1)*t(3,1)+b1(i2)*t(3,2)+b1(i3)*t(3,3)

exh=bh1(i1)*t(1,1)+bh1(i2)*t(1,2)+bh1(i3)*t(1,3)

eyh=bh1(i1)*t(2,1)+bh1(i2)*t(2,2)+bh1(i3)*t(2,3)

ezh=bh1(i1)*t(3,1)+bh1(i2)*t(3,2)+bh1(i3)*t(3,3)

b1(i1)=ex

b1(i2)=ey

b1(i3)=ez

bh1(i1)=exh

bh1(i2)=eyh

bh1(i3)=ezh

102 continue

do 104 i=1,np

i1 = 3*(i-1)+1

i2 = i1 + 1

i3 = i1 + 2

ex=bx(i1)*t(1,1)+bx(i2)*t(1,2)+bx(i3)*t(1,3)

ey=bx(i1)*t(2,1)+bx(i2)*t(2,2)+bx(i3)*t(2,3)

ez=bx(i1)*t(3,1)+bx(i2)*t(3,2)+bx(i3)*t(3,3)

exh=bhx(i1)*t(1,1)+bhx(i2)*t(1,2)+bhx(i3)*t(1,3)

eyh=bhx(i1)*t(2,1)+bhx(i2)*t(2,2)+bhx(i3)*t(2,3)

ezh=bhx(i1)*t(3,1)+bhx(i2)*t(3,2)+bhx(i3)*t(3,3)

```
bx(i1)=ex  
bx(i2)=ey  
bx(i3)=ez  
bhx(i1)=exh  
bhx(i2)=eyh  
bhx(i3)=ezh
```

104 continue

```
return  
end
```

```

c
c--sub: tmatrix
c---- calculates matrix t

c
subroutine tmatrix(z,cc,sc,cp,sp,t)
complex t(3,3),h10,h12
s=sin(z)
c=cos(z)
h10=cmplx(s,-c)/z
z1=(3./z/z-1.)*s-3.*c/z
z2=(1.-3./z/z)*c-3.*s/z
h12=cmplx(z1,z2)/z
t(1,1)=2.0*h10-h12*(1-3.0*sc*sc*cp*cp)
t(1,2)=h12*3.0*sc*sc*sp*cp
t(1,3)=h12*3.0*sc*cc*cp
t(2,1)=t(1,2)
t(2,2)=2.0*h10-h12*(1.0-3.0*sc*sc*sp*sp)
t(2,3)=h12*3.0*sc*cc*sp
t(3,1)=t(1,3)
t(3,2)=t(2,3)
t(3,3)=2.0*h10-h12*(1-3.0*cc*cc)
return
end

```

```

c
c---sub: strait
c---- generate straight chain geometry
subroutine strait(nt)

parameter (mnp=100)
common/l1/x(mnp),y(mnp),z(mnp)
common/ran/xl
nt2=nt/2
if(nt-2*nt2.eq.0)then
  do 140 i=1, nt2
    x(i)=0.0
    y(i)=0.0
    z(i)=-0.5+(i-nt2)*1.0
    x(i+nt2)=0.0
    y(i+nt2)=0.0
    z(i+nt2)=0.5+(i-1)*1.0
140      continue
else
  do 142 i=1, nt2
    x(i)=0.0
    y(i)=0.0
    z(i)=-1.0+(i-nt2)*1.0
    x(i+nt2+1)=0.0
    y(i+nt2+1)=0.0
    z(i+nt2+1)=1.0+(i-1)*1.0
142      continue
  x(nt2+1)=0.0
  y(nt2+1)=0.0
  z(nt2+1)=0.0
end if
xl=nt
return
end

```

```

c
c---s u b: cbdecp
c----- cholesky decomposition :a=(l)(d)(u)
parameter (mnp=100, mn3=mnp*3)
complex a(mn3,mn3), aij, ajj
do 40 j=1,n
    j1=j-1
    if (j1.lt.2) go to 25
    do 20 i=2,j1
        i1=i-1
        aij=cmplx(0.0,0.0)
        do 10 k=1,i1
            10    aij=aij+a(k,i)*a(k,j)*a(k,k)
            a(i,j)=(a(i,j)-aij)/a(i,i)
        20    a(j,i)=a(i,j)
        25    ajj= cmplx(0.0,0.0)
            if (j.eq.1) go to 35
            do 30 k1=1,j1
        30    ajj=aij+ a(k1,j)*a(k1,j)*a(k1,k1)
            a(j,j)=a(j,j)-aij
        35    if(a(j,j).eq.0.) go to 50
40 continue
    return
50 print 55
55 format(/ 'a(j,j) is zero program stop.')
    return
end

```

c

c---sub: coord transforms (x',y',z') into measuring coord.(x,y,z)

couples with size parameter alpha*2

subroutine coord(np,alpha,cchi,schi,cpsi,spsi)

parameter (mnp=100)

dimension c(3,3),p(3)

common/l1/xo(mnp),yo(mnp),zo(mnp)

common/l2/x(mnp),y(mnp),z(mnp)

common/trans1/c

c(1,1)=cpsi*cchi

c(1,2)=-spsi

c(1,3)=cpsi*schi

c(2,1)=spsi*cchi

c(2,2)=cpsi

c(2,3)=spsi*schi

c(3,1)=-schi

c(3,2)=0.

c(3,3)=cchi

do 10 i=1,np

p(1)=xo(i)

p(2)=yo(i)

p(3)=zo(i)

x(i)=0.

y(i)=0.

z(i)=0.

do 10 j=1,3

x(i)=x(i)+2.*alpha*c(1,j)*p(j)

y(i)=y(i)+2.*alpha*c(2,j)*p(j)

10 z(i)=z(i)+2.*alpha*c(3,j)*p(j)

return

end

c-

c---sub: cbsolx

c---- (l)(d)(u)(x)=(b) with (d) cannot be zero

c---- let (l)(z)=(b), and (d)(u)(x)=(z)

c---verified November 15, 1993---

subroutine cbsolx(a,b,n)

parameter (mnp=100, mn3=mnp*3)

complex a(mn3,mn3),b(n)

do 70 i=2,n

i1=i-1

do 60 k=1,i1

60 b(i)=b(i)-a(k,i)*b(k)

70 continue

c divided by diagonal

c (d)(y)=(z), where (y) to be found

do 72 i=1,n

72 b(i)=b(i)/a(i,i)

c backward substitution

c (u)(x), where (x) is final solution

do 80 i = n-1,1,-1

do 75 j=i+1,n

75 b(i)=b(i)-a(i,j)*b(j)

80 continue

return

end

VIII. USER'S GUIDE FOR AGGL WITH SOURCE CODE

1. User Interface: AGGL_SHELL

To use AGGL, simply call AGGL_SHELL from your main program in the following format:

CALL AGGL_SHELL(NP,NX,NPS,ALPHA,RFINDEX)

where

ALPHA: Primary particle size parameter
NP: Number of primary particles in the agglomerate
NX: Number of scattering angles
NPS: Number of structures used to mimic randomly branched chains
RFINDEX: Complex refractive index, the imaginary part must be positive

Other input/output data are transferred via COMMON blocks, see the following list,

<u>Block</u>	<u>Variables</u>	<u>Explanation</u>
<u>name</u>	<u>carrying</u>	
L1	X,Y,Z:	Coordinate components of the particle centers of the agglomerate
P2	CHAIN	Type of chains, 'R' for randomly branched chain, 'S' for straight 'C' for cluster, 'U' for user specified geometry
LOU	LU1	Switch for Q_{sca} computation, 0 for subtraction, 1 for direct computation
	LU3	Switch for orientation, 0 for random orientation 1 for a specific orientation
	LU4	Switch for derivative computation, 0 for no derivative computation, 1 to calculate derivatives
Qextm	QE,QA,QS	Extinction, absorption, and total scattering efficiency factors
Louv	RPP	Dissymmetry, depolarization ratios and extinction normalized differential scattering efficiencies under vertical incidence
Louh		Same as Louv but under horizontal incidence
J2sm	QPP	Differential scattering efficiencies under both vertical and horizontal incidences. P can be V or H standing for vertical or horizontal
	ANGK	Scattering angles where differential scattering is to be computed
LON	DPPN	Derivatives with respect to the real part of the refractive index
LOK	DPPK	Derivatives with respect to the imaginary part of the refractive index
Loux	DPPX	Derivatives with respect to the size parameter x

Orient Dchi,Dpsi Orientation of the agglomerate if not random

2. Output List

QEXT: Extinction efficiency factor for vertical incidence

QABS: Absorption efficiency factor for vertical incidence

QSCA: Total scattering efficiency factor for vertical incidence

QEXTH: Same as QEXT, but for horizontal incidence

QABSH: Same as QABS, but for horizontal incidence

QSCAH: Same as QSCA, but for horizontal incidence

CPP(): Differential scattering efficiencies. P can be either V or H

standing for vertical or horizontal polarization states. The first P
is related to the observation or measurement, and the second P the incidence light.

RPP(): Dissymmetry or depolarization ratios(optional)

KVV(): Extinction normalized differential scattering(optional)

DQEXTq: Derivative of QEXT with respect to q. Q

can be n(real part of the refractive index), k (imaginary part of the refractive index),
or x (size parameter)

DCPPq: Derivative of CPP with respect to q. (Optional)

3 Sample Master Program and Results

The following is a sample master program which makes use of AGGL to calculate the extinction, absorption, total scattering, and differential scattering efficiencies under both vertical incidence and horizontal incidence for a straight chain of 10 particles with a specific orientation ($\chi=45$ deg and $\psi=60$ deg). Other parameters are $x=0.2$ and $m=1.7+0.7i$. Computational results are given after the program.

Note the symbols "\$" and "&" are exclusively used to mark continuing lines. Other symbols used for the same purpose are "#" and "@".

C*****

C— THIS IS A SAMPLE USER' MASTER PROGRAM *****

C*****

C23456789012345678901234567890123456789012345678901234567890123456789

C PROGRAM MASTER.FOR

PARAMETER (NS=181, NC=1, MNP=100,NX=37)

C***THE FOLLOWING LINES CAN NOT BE CHANGED. FOLLOW STRICTLY!***

C*** WHILE WRITING YOUR OWN MASTER PROGRAM *****

COMPLEX RFINDX,EPSON

CHARACTER EFF*1,POL*1,CHAIN*1

COMMON/P2/POL,EFF,CHAIN

COMMON/LOU/LU,LU1,LU2,LU3,LU4

COMMON/J2SM/SCAHHK(181),SCAVVK(181), SCAHK(181), SCAVHK(181),

\$ ANG(181)

COMMON/QEXTM/QEXT,QABS,QSCA,QEXTH,QABSH,QSCAH

COMMON/ORIENT/DCHI,DPSI

REAL KVVE(NS),KHHE(NS),KHVE(NS),KVHE(NS)

COMMON/LOUV/RVV(NS),DRVVN(NS),DRVVK(NS),

\$ DKHVN(NS),DKHVEK(NS),

\$ KVVE,DKVVEN(NS),DKVVEK(NS),RHV(NS),DRHVN(NS),

\$ DRHVK(NS),KHVE,KVHE

COMMON/LOUH/RHH(NS),DRHHN(NS),DRHHK(NS),

\$ DKVHEN(NS),DKVHEK(NS),

\$ KHHE,DKHHEN(NS),DKHHEK(NS),RVH(NS),DRVHN(NS),DRVHK(NS)

COMMON/LOUX/QETX,DRVNX(NS),DRHGX(NS),DRVHX(NS), DRHHX(NS),

\$ QEHTX,DKVVE(X(NS),DKHVE(X(NS),DKVHE(X(NS),DKHHE(X(NS)

C***ALL OF THE NAMES APPEARED ABOVE ARE RESERVED. *****

C*** DO NOT ATTEMPT TO CHANGE OR RENAME *****

CHARACTER*40 NAMDAT,NAMOUT,NAMPLT

NAMOUT='[MELOU.MIE]CHAIS6.OUT'

NAMDAT='[MELOU.MIE]CHAIS6.DAT'

NAMPLT='[MELOU.MIE]CHAS.DAT'

OPEN(UNIT=12,FILE=NAMOUT ,STATUS='UNKNOWN')

```
OPEN(UNIT=13,FILE=NAMPLT,STATUS='UNKNOWN')
OPEN(UNIT=14,FILE=NAMDAT,STATUS='UNKNOWN')
```

C---OPTIONS

C--SELF-TERM OPTIONS: LU

C LU=0 FOR JONES;

C 1 FOR THIRD ORDER APPROXIMATION (GOEDECKE&O'BRIEN)

C 2 FOR EXACT SOLUTION

C----- 3 OTHERS

LU=1

C--TOTAL SCATTERING OPTIONS:

C LU1=0 FOR SUBTRACTION FROM EXTINCTION AND ABSORPTION

C----- 1 FOR DIRECT INTEGRATION

LU1=0

C--T MATRIX OPTIONS:

C LU2=0 FOR JONES (INCORRECT)/DISABLED

C----- 1 FOR CORRECTED TENSOR MATRIX

LU2=1

C--ORIENTATION OPTIONS:

C LU3=0 FOR RANDOM ORIENTATION;

C----- 1 FOR A SPECIFIC ORIENTATION

LU3=1

IF(LU3.EQ.1)THEN

 DCHI=45.0

 DPSI=60.0

END IF

C--SCATTERING DERIVATIVES OPTIONS:

C LU4=1 FOR DERIVATIVE CALCULATIONS
C----- 0 TO SKIP DERIVATIVES
LU4=0

C--OTHER OPTIONS/ POL OPTION DISABLED/
C--CHAIN: SELECT AMONG 'S', 'C', 'R', OR, 'U'
EFF='F'
POL='H'
CHAIN='S'

C--DATA SPECIFICATION:

```
IF(CHAIN.EQ.'R')THEN
  NPS=500
END IF
NP = 10
DO 100 K=1,NX
100 ANG(K)=(K-1)*180.0/(NX-1)
WL=.488
REF =1.7
RIM =.7
PI=3.1415926
REFMED=1.0
RFINDEX=CMPLX(REF, RIM)/REFMED
```

```
DO 303 IL=1, NC
ALPHA=0.2+0.05*(IL-1)
DIA=ALPHA*WL/PI
CALL AGGL_SHELL(NP,NX,NPS,ALPHA,RFINDEX)
```

C!!!—DATA OUTPUT BLOCK _____
C!!!—THIS BLOCK IS NOT CRUTIAL AND OMITTED HERE TO SAVE SPACE
C!!!_____

303 CONTINUE
STOP

END

C***This is the output of the sample master program. Make sure run the preceding sample C***program and obtain the same result before using AGGL_Shell for your applications

DATA FILES:

[MELOU.mie]CHAIs6.OUT

[MELOU.Mie]CHAIs6.DAT

PRIMARY PARTICLE DIAMETER = 0.03107 UM

REFRACTIVE INDEX: M = 1.700 -I 0.700

NUMBER OF PRIMARY PARTICLES = 10

PRIMARY PARTICLE SIZE PARAMETER = 0.200

AGGLOMERATE SIZE PARAMETER = 2.000

STRAIGHT CHAINS

FULLY COUPLED SOLUTION

NUMBER OF ITERATIONS 1

SPECIFIED ORIENTATION

CHI= 45.00000 DEGS AND PSI= 60.00000

SCATTERING COEFFICIENT(VERT.) QSCAT= 6.5750182E-03

EXTINCTION COEFFICIENT(VERT.) QEXT= 0.2265852

ABSORPTION COEFFICIENT(VERT.) QABS= 0.2200102

SCATTERING COEFFICIENT(Hort.) QSCATH= 8.2514584E-03

EXTINCTION COEFFICIENT(Hort.) QEXTh= 0.2679992

ABSORPTION COEFFICIENT(Hort.) QABSh= 0.2597477

Scattering		Differential Scattering Efficiencies		
Angle (deg)	Q _{VV}	Q _{hh}	Q _{hv}	Q _{vh}
0.0	0.1468E-02	0.1709E-02	0.1128E-04	0.1128E-04
5.0	0.1463E-02	0.1663E-02	0.9565E-05	0.1111E-04
10.0	0.1446E-02	0.1581E-02	0.7863E-05	0.1090E-04
15.0	0.1420E-02	0.1471E-02	0.6242E-05	0.1066E-04
20.0	0.1390E-02	0.1340E-02	0.4755E-05	0.1041E-04
25.0	0.1358E-02	0.1197E-02	0.3440E-05	0.1015E-04
30.0	0.1327E-02	0.1048E-02	0.2323E-05	0.9905E-05
35.0	0.1300E-02	0.8992E-03	0.1418E-05	0.9675E-05
40.0	0.1277E-02	0.7545E-03	0.7332E-06	0.9472E-05
45.0	0.1261E-02	0.6171E-03	0.2715E-06	0.9303E-05
50.0	0.1252E-02	0.4894E-03	0.3435E-07	0.9173E-05
55.0	0.1249E-02	0.3730E-03	0.2302E-07	0.9087E-05
60.0	0.1253E-02	0.2694E-03	0.2397E-06	0.9047E-05
65.0	0.1263E-02	0.1802E-03	0.6871E-06	0.9056E-05
70.0	0.1278E-02	0.1072E-03	0.1368E-05	0.9114E-05
75.0	0.1295E-02	0.5243E-04	0.2281E-05	0.9219E-05
80.0	0.1313E-02	0.1822E-04	0.3423E-05	0.9369E-05
85.0	0.1329E-02	0.6583E-05	0.4778E-05	0.9559E-05
90.0	0.1340E-02	0.1896E-04	0.6322E-05	0.9784E-05
95.0	0.1343E-02	0.5562E-04	0.8013E-05	0.1004E-04
100.0	0.1336E-02	0.1151E-03	0.9797E-05	0.1030E-04
105.0	0.1316E-02	0.1939E-03	0.1160E-04	0.1058E-04
110.0	0.1281E-02	0.2864E-03	0.1335E-04	0.1084E-04
115.0	0.1230E-02	0.3852E-03	0.1495E-04	0.1109E-04
120.0	0.1165E-02	0.4816E-03	0.1632E-04	0.1130E-04
125.0	0.1086E-02	0.5672E-03	0.1739E-04	0.1146E-04
130.0	0.9966E-03	0.6343E-03	0.1808E-04	0.1156E-04
135.0	0.8991E-03	0.6775E-03	0.1838E-04	0.1159E-04
140.0	0.7975E-03	0.6940E-03	0.1827E-04	0.1154E-04
145.0	0.6954E-03	0.6840E-03	0.1778E-04	0.1141E-04
150.0	0.5962E-03	0.6504E-03	0.1695E-04	0.1120E-04
155.0	0.5029E-03	0.5980E-03	0.1585E-04	0.1092E-04

160.0	0.4175E-03	0.5326E-03	0.1454E-04	0.1057E-04
165.0	0.3413E-03	0.4603E-03	0.1310E-04	0.1015E-04
170.0	0.2750E-03	0.3868E-03	0.1161E-04	0.9699E-05
175.0	0.2186E-03	0.3163E-03	0.1013E-04	0.9212E-05
180.0	0.1715E-03	0.2521E-03	0.8709E-05	0.8709E-05